

SOPAC



PACIFIC ISLANDS APPLIED GEOSCIENCE COMMISSION

THREE DIMENSIONAL WAVE-CURRENT HYDRODYNAMIC MODEL FOR THE MANAGEMENT OF SAIPAN LAGOON SAIPAN, COMMONWEALTH OF THE NORTHERN MARIANA ISLANDS

*SOPAC Technical Report 439
November 2010*

Herve Damlamian and Jens Krüger
Ocean & Islands Programme, SOPAC

Financial support for this report was provided by the Coastal Zone Management Act of 1972, as amended, administered by the Office of Ocean and Coastal Resource Management, National Oceanic and Atmospheric Administration. Support was also received from RBR, Canada, through the provision of tide and wave recorders.

PACIFIC ISLANDS APPLIED GEOSCIENCE COMMISSION

c/o SOPAC Secretariat

Private Mail Bag

GPO, Suva

FIJI ISLANDS

<http://www.sopac.org>

Phone: +679 338 1377

Fax: +679 337 0040

www.sopac.org

director@sopac.org

Cataloguing in Publication Data:

Damlamian, Herve

Three dimensional wave-current hydrodynamic model for the management of Saipan Lagoon, Saipan, Commonwealth of the Northern Mariana Islands/Herve Damlamian and Jens Krüger. – Suva: SOPAC, 2010.

73 p.: ill.; 30 cm

ISSN: 1605-4377

1. Hydrodynamic modelling – Commonwealth of the Northern Mariana Islands

2. Environmental management – Saipan Lagoon

I. Krüger, Jens

II. SOPAC Technical Report 439

III. Title

TABLE OF CONTENTS

List of Figures	3
ACKNOWLEDGEMENTS	6
1 INTRODUCTION.....	8
2 STUDY AREA	9
2.1 Location.....	9
2.2 Oceanography and Meteorology.....	10
2.3 Inter-annual variations	11
3 METHODS.....	12
3.1 Physical Oceanography	12
3.2 Three Dimensional Wave-Current Hydrodynamic Model	13
4 RESULTS	24
4.1 Water Circulation	24
4.2 Plume Dispersion.....	48
4.3 Component Plume Dispersion	54
4.4 Residual Current Patterns	69
5 REFERENCES.....	73

List of Figures

Figure 1. Quickbird satellite image of Saipan	9
Figure 2. Locality diagram of the northern Saipan lagoon.	10
Figure 3. Mean annual number of tropical storms and typhoons	10
Figure 4. Time series plot of normalised monthly averaged tide gauge observations	11
Figure 5. Equipment locations within Saipan Lagoon, April to June 2010.....	12
Figure 6. Composite bathymetry for Saipan Island	14
Figure 7. Detail of model grid.....	15
Figure 8. Example of a 3D mesh using sigma layers.....	15
Figure 9. Flow chart showing the model calibration process.....	16
Figure 10. Time series of wave calibration for the wave gauge on the northern reef slope	16
Figure 11. Time series of surface elevation calibration for the northern reef slope and flat	17
Figure 12. Time series of surface elevation observed at the tide gauge	17
Figure 13. Calibration results between the observed and those obtained from the model.....	18
Figure 14. Calibration results between the observed current speed and those modelled for the ADP location in the lagoon	19
Figure 15. Calibration results between the observed current speed and those modelled for the AWAC near the outfall.	20
Figure 16. Calibration results for the observed current directions and those obtained from the model for the ADP location in the channel.	21
Figure 17. Time series of pollutant discharge concentration near the outfall	22
Figure 18. Chart outlining the work flow and model runs of the seasonal approach.....	23
Figure 19. Bathymetry of Tanapag Lagoon.	24
Figure 20. Snapshot of wave model output showing southward component of wave-induced radiation stress for Scenario 1	25
Figure 21. Snapshot of the dominant near bed current pattern in Tanapag Lagoon for Scenario 1	25

Figure 22. Snapshot of the near bed current pattern at spring low tide in Tanapag Lagoon for Scenario 1	26
Figure 23. Snapshot of wave model output showing southward component of wave-induced radiation stress for Scenario 2	27
Figure 24. Snapshot of the dominant bed current pattern in Tanapag Lagoon for Scenario 2 showing lagoon-ward flow through the shipping channel.....	27
Figure 25. Snapshot of the near bed current pattern in Tanapag Lagoon at peak high tide for Scenario 2.....	28
Figure 26. Locality diagram showing positions of model extraction points used to highlight the differences between scenarios 1 and 2.....	28
Figure 27. Comparative time series of observed surface elevation at the tide gauge and current speeds extracted from the northern lagoon.....	29
Figure 28. Comparative time series of observed surface elevation at the tide gauge and current direction extracted from the model in the shipping channel	29
Figure 29. Time series comparing the surface and bottom layer current speed and direction for Scenario 2 in the shipping channel at location 1 in Figure 26.....	30
Figure 30. Time series comparing the surface and bottom layer current speed and direction for Scenario 2 near the outfall at location 2 in Figure 26.	31
Figure 31. Time series comparing the surface and bottom layer current speed and direction for Scenario 2 in the lagoon at location 3 in Figure 26.....	31
Figure 32. Bathymetry of Garapan Lagoon	32
Figure 33. Snapshot of wave model output showing eastward component of wave-induced radiation stress for Season 1	33
Figure 34. Snapshot of the dominant near bed current pattern in Garapan lagoon during Scenario 1 showing southward water flow	34
Figure 35. Snapshot of the near bed current pattern during low tide in Garapan lagoon during Scenario 1, showing outward flow through the Garapan and Sugar Dock channels	35
Figure 36. Comparative time series of observed surface elevation at the tide gauge and current speeds extracted from the Garapan and Sugar Dock channels	36
Figure 37. Close up of the Sugar Dock and channel, showing near bed lagoon-ward flow for Scenario 1.....	37
Figure 38. Snapshot of wave model output showing eastward component of wave-induced radiation stress for Season 2	38
Figure 39. Snapshot of the dominant near bed current pattern in Garapan lagoon during Scenario 2 showing a predominantly inward and southward water flow	39
Figure 40. Near bed current patterns during Season 2 showing the influence of the dominant discharge through the shipping channel during high tide on water circulation between Puntan Muchot and Garapan pier	40
Figure 41. Near bed current patterns at low tide for Scenario 2.....	41
Figure 42. Comparative time series of observed surface elevation for Scenario 2 at the tide gauge and current direction extracted from the model in the Garapan Dock channel for the surface and near bed layers.....	42
Figure 43. Comparative time series of observed surface elevation for Scenario 2 at the tide gauge and current direction extracted from the model in the Sugar Dock channel for the surface and near bed layers	43
Figure 44. Bathymetry of Chalan Kanoa Lagoon	44
Figure 45. Snapshot of wave model output showing eastward component of wave-induced radiation stress for Scenario 1	44
Figure 46. Snapshot of dominant near bed current pattern in Chalan Kanoa Lagoon for Scenario 1, showing dominant southward flow.....	45
Figure 47. Snapshot of near bed current pattern during low tide in Chalan Kanoa Lagoon for Scenario 1	46
Figure 48. Snapshot of dominant near bed current pattern in Chalan Kanoa Lagoon for Scenario 2.....	47
Figure 49. Snapshot of near bed current pattern at low tide in Chalan Kanoa Lagoon for Scenario 2.....	48
Figure 50. Snapshot of plume in Tanapag lagoon during Scenario 1.....	49
Figure 51. Snapshot of plume in the southern Saipan lagoon during Scenario 1	50
Figure 52. Snapshot of plume in Tanapag lagoon during Scenario 1.....	51
Figure 53. Snapshot of plume in the south of Saipan lagoon during Scenario 1	52

Figure 54. Snapshot of plume in Tanapag lagoon during Scenario 2.....	53
Figure 55. Snapshot of plume in the southern Saipan lagoon during Scenario 2.....	54
Figure 56. Snapshot of plume of Nitrate under Scenario 1.....	55
Figure 57. Snapshot of plume of Nitrate under Scenario 1.....	55
Figure 58. Snapshot of plume of Nitrate under Scenario 2.....	56
Figure 59. Snapshot of plume of Nitrate under Scenario 2.....	56
Figure 60. Snapshot of plume of Total Nitrogen under Scenario 1.....	57
Figure 61. Snapshot of plume of Total Nitrogen under Scenario 1.....	57
Figure 62. Snapshot of plume of Total Nitrogen under Scenario 2.....	58
Figure 63. Snapshot of plume of Total Nitrogen under Scenario 2.....	58
Figure 64. Snapshot of plume of Orthophosphate and Total Phosphorus under Scenario 1.....	59
Figure 65. Snapshot of plume of Orthophosphate and Total Phosphorus under Scenario 1.....	59
Figure 66. Snapshot of plume of Orthophosphate and Total Phosphorus under Scenario 2.....	60
Figure 67. Snapshot of plume of Orthophosphate and Total Phosphorus under Scenario 2.....	60
Figure 68. Snapshot of plume of unionised Ammonia under Scenario 1.....	61
Figure 69. Snapshot of plume of unionised Ammonia under Scenario 1.....	61
Figure 70. Snapshot of plume of unionised Ammonia under Scenario 2.....	62
Figure 71. Snapshot of plume of unionised Ammonia under Scenario 2.....	62
Figure 72. Snapshot of plume of Copper under Scenario 1.....	63
Figure 73. Snapshot of plume of Copper under Scenario 1.....	63
Figure 74. Snapshot of plume of Copper under Scenario 2.....	64
Figure 75. Snapshot of plume of Copper under Scenario 2.....	64
Figure 76. Snapshot of plume of Nickel under Scenario 1.....	65
Figure 77. Snapshot of plume of Nickel under Scenario 1.....	65
Figure 78. Snapshot of plume of Nickel under Scenario 2.....	66
Figure 79. Snapshot of plume of Nickel under Scenario 2.....	66
Figure 80. Snapshot of plume of Zink under Scenario 1.....	67
Figure 81. Snapshot of plume of Zink under Scenario 1.....	67
Figure 82. Snapshot of plume of Zink under Scenario 2.....	68
Figure 83. Snapshot of plume of Zink under Scenario 2.....	68
Figure 84. Residual current vectors for Scenario 1 at Managaha Island.....	69
Figure 85. Residual current vectors for Scenario 2 at Managaha Island.....	69
Figure 86. Residual current vectors for Scenario 1.....	70
Figure 87. Residual current vectors for Scenario 2 at Muchot Point.....	70
Figure 88. Residual current vectors for Scenario 1 at Sugar Dock.....	71
Figure 89. Residual current vectors for Scenario 2 at Sugar Dock.....	71
Figure 90. Residual current vectors for Scenario 1 at San Antonio.....	72
Figure 91. Residual current vectors for Scenario 2 at San Antonio.....	73

ACKNOWLEDGEMENTS

The successful conduct of this survey has been with the assistance of a number of individuals from CRMO and beyond. We would like to acknowledge the support of the following people: John John Sannicolas, Annie Agutto, Julie Duenas, Ben Cabrera, John Iguel, Rita Dela Cruz, Doris Chong, Rodney Camacho, John Starmer, Heidi Yelin, and Paul Camacho.

EXECUTIVE SUMMARY

Damlamian, H., Krüger, J., 2010. Three dimensional wave-current hydrodynamic model for the management of Saipan lagoon, Saipan, Commonwealth of the Northern Mariana Islands. *SOPAC Technical Report 439*, 73 pp.

The purpose of the project was to establish a numerical model describing the water flow in the lagoon and to undertake a coastal erosion assessment. The study is in support of an update of regulations for marine and coastal activities and the 1997 Saipan Lagoon Use Management Plan (SLUMP).

A field data collection campaign was carried out from April to June 2010. The field data was used to calibrate the coupled three dimensional wave-current hydrodynamic numerical model, which reproduces the observed coupling between offshore waves and lagoon currents. The model was subsequently run to reproduce two seasonal scenarios, being the relatively calm period from April to September and the more energetic months from October to March. These seasonal models runs were used to model the dispersion of pollutants discharging from the Sadog Tasi outfall. No data was available to calibrate the material transport model but the model was assumed to be representative of the actual dispersion at least in the near field, as the initial dilution rate at the outfall was in agreement with the theoretical value of 77:1.

For each of the two seasonal scenarios, the model was used to look in detail at two types of discharge material. Firstly, the effluent was considered to be an imaginary substance with a concentration of 100 g/m³. The model was then used to investigate the diffusion of this plume in space and the variation of its concentration over time. Secondly, the discharge consisted of the nine most common constituents (Nitrate, Total Nitrogen, Orthophosphate, Total Phosphorous, Unionized Ammonia, Copper, Nickel, Zinc, TRC). This was further analysed by varying the concentration and keeping it constant according to the specific maximum monthly averaged concentration as stipulated in the 2008 Sadog Tasi permit, and releasing the material with a daily constant concentration according to their specific maximum daily concentration allowed. Note that in this last case, a day of discharge is followed by one day of pollution free flow. Each scenario was run for 30 days and the resultant model was inspected with regards to the dominant current patterns, the dispersion of pollutants, and the residual velocity fields.

Since the circulation in Tanapag lagoon is mainly driven by offshore wave forces, overall current speed within the lagoon is much stronger from October to March compared to the months April to September. Water is predominantly pumped into the lagoon over the barrier reef by wave action and exits via the channel from October to March. The model shows the reverse for the period from April to September, when an east-directed inward flux of oceanic waters dominates, with outward flushing occurring for less than four hours a day during leading ebb periods. Wind stress also plays an important role in the water circulation, with a significant contribution on the surface layer.

The overall impact of the seasonality is that Saipan lagoon exhibits relatively good flushing (reduced lagoon water residence time) from October to March compared to the low energy period April to September. From October to March the plume discharged from Sadog Tasi does not significantly impact on the Managaha marine conservation area, but is partly driven south into Garapan lagoon with a concentration of less than 0.05% of the initial concentration. During the months April to September, the model shows the plume residing within the conservation area with levels of up to 0.35% of the initial concentration of pollutants set at 100%.

The model outputs suggest that the instantaneous concentration of pollutants in the plume discharged from Sadog Tasi outfall is well below the limits stipulated by CNMIWQS. However, the model only investigated the advection and dispersion of the pollutants, treating them as inert neutrally buoyant particles. No settling velocity other bio-chemical reactions were attributed. The potential for metal to be fixed by sediment is high in Saipan Lagoon (Denton *et al.* 2006). Accumulation of metals in the sediment could be a threat to human health in Saipan. A sediment sample collection survey should be undertaken to further analyse and determine the rate of accumulation of harmful pollutants. The plume pathways presented in this report can act as a guide to concentrate sampling regimes within the common plume pathways such as east and south of Managaha Island as well as near Muchot point. Furthermore, it is recommended to map a plume of Rhodamine with a GPS-integrated fluorometer or similar technique, in order to confirm plume dilution and dispersion.

1 INTRODUCTION

Hydrodynamic numerical modelling of Saipan Lagoon (Figure 1) was undertaken by the Pacific Islands Applied Geoscience Commission (SOPAC) based on field calibration data collected from April to June 2010. This work was initiated by the Coastal Resources Management Office (CRMO) of the Commonwealth of the Northern Mariana Islands (CNMI). The purpose of the project was to establish a numerical model describing the water flow in the lagoon and to undertake a coastal erosion assessment. The study is in support of an update of regulations for marine and coastal activities and the 1997 Saipan Lagoon Use Management Plan (SLUMP). Specifically, CRMO requires recommendations based on defensible scientific studies on current patterns and coastal erosion trends to update the SLUMP in order to balance economic growth with sustaining a beautiful and healthy coastal environment. Hence, the scope of work was to:

- understand current patterns within the confines of Saipan Lagoon and the effects of these patterns on coastal processes and the distribution of pollutants from Sadog Tasi Sewer Outfall and priority drainages; and
- understand and manage trends in erosion or accretion of coastal beaches at Puntan Muchot (Memorial Park), Sugar Dock, San Antonio and Managaha Island; and
- project future environmental trends so appropriate management policies may be developed before adverse impacts are experienced.

A companion report of the fieldwork component with details on the oceanographic data collected used to calibrate the model has been published by Kruger *et al.* (2010). This report covers the results of the three-dimensional wave-current model of Saipan lagoon set up under this study.

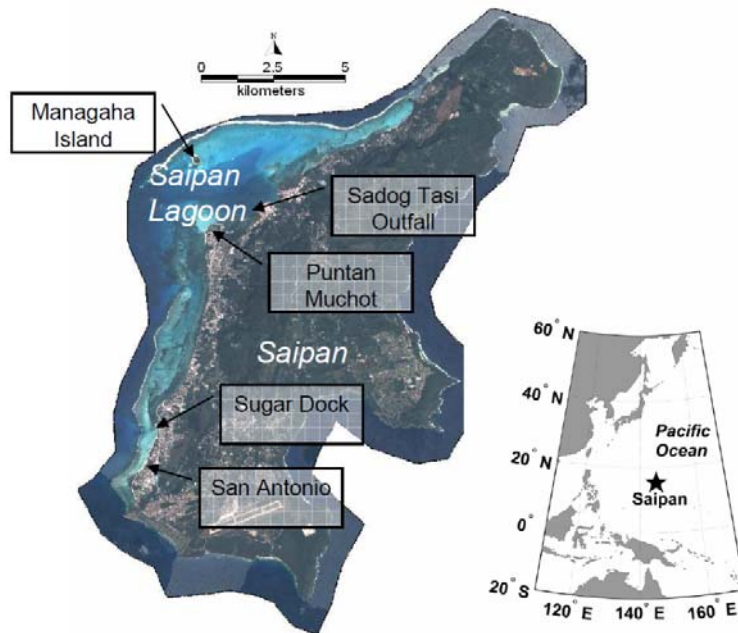


Figure 1. Satellite image of Saipan showing the lagoon bordering the western shore of the island, and the location of field sites. Image is a 2005 Quickbird satellite image provided by CRMO.

2 STUDY AREA

2.1 Location

The island of Saipan is located at 15.23°N and 145.75°E in the western north Pacific. The island is 23 km long trending in an ENE-SWS direction, and generally some 5 km wide west-east and comprises volcanic rocks overlain by younger limestone. Saipan lagoon along the western leeward side of the island has an area of approximately 32 km² (Figure 6) and supports a variety of recreational and commercial activities and many local people harvest the fisheries resources for food.

The primary sources of anthropogenic disturbances are located in the northern Saipan Lagoon waters of Tanapag Harbour (Figure 2). The Puerto Rico Industrial area extends along the coastline from Muchot Point (Smiling Cove Marine) in the south to Point Dogas in the north. This areas comprises small-boat marinas, a municipal waste dump closed in 1997, the Sadog Tasi sewer outfall, a commercial port of Saipan Harbour, and a bulk fuel facility (Denton *et al.* 2006), and has been classified as Class A waters out to 1000 m from the shore, whilst all other waters within the lagoon are Class AA (Bearden 2010). Class AA means that waters should remain in their natural pristine state as close as possible, whilst Class A allows other uses as long as they are compatible with the protection and propagation of fish, shellfish, and wildlife, and recreation in and on the water of a limited body contact nature (Bearden 2010).

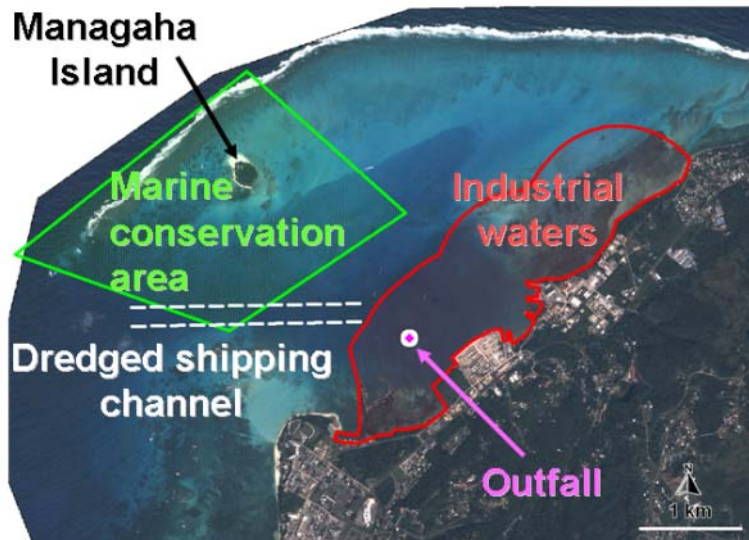


Figure 2. Locality diagram of the northern Saipan lagoon showing the competing demands on the lagoon water with an area of industrial waters (Class A, red polygon) which is inclusive of the Sadog Tasi outfall (circle), the Managaha Island marine conservation area¹, MCA, (green polygon), as well as a shipping lane (dashed lines outlining the dredged shipping channel). Backdrop is an unrectified 2005 Quickbird satellite image supplied by CRMO.

2.2 Oceanography and Meteorology

The climate of Saipan is classified tropical marine where a monsoon influences the western North Pacific from July that can bring strong southwest winds and rough seas to the western shoreline. By January the conditions return to that of a trade wind regime with winds and seas predominantly from the east (Lander 2004). The main tropical cyclone season for the western North Pacific extends from mid-May through mid-December. In the region of Saipan, the frequency of tropical cyclones is three per 5-degree latitude-longitude square per year as shown in Figure 3.

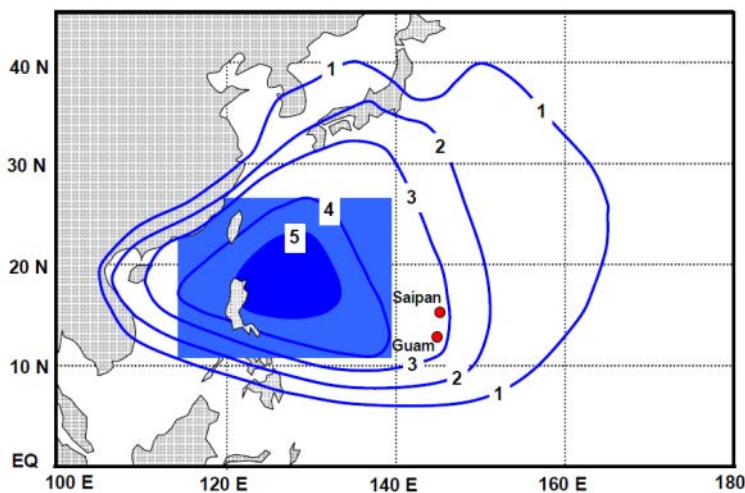


Figure 3. Mean annual number of tropical storms and typhoons traversing 5-degree latitude by 5-degree longitude squares (from Lander 2004)

The field observations presented in Kruger *et al.* (2010) demonstrated a strong link between incident offshore surface wave heights and lagoon currents. As waves break on a reef, they create a radiation stress gradient that drives wave-setup and thereby wave-induced currents. Waves therefore exert a major control on the circulation patterns of Saipan Lagoon, a process which is typical for a coral reef environment (e.g. Hench 2006, Lowe *et al.* 2009). For example, when oceanic swell is high, flow can be positive toward

¹ The boundary points of the conservation area were taken from the Managaha Marine Conservation Act of 2000 (Public Law No. 12-12 H.B. No 12-162, CSI). Other maps (e.g. Schroer 2005) show the southern most point of the conservation area lying just north of the shipping channel boundary, and not, as in Figure 2, just south of the channel. We note that the backdrop image in the figure may also not be positioned correctly as no rectified version was available at the time of writing.

the lagoon over the reef regardless of the tidal period. One of the main aims of the modelling was therefore to reproduce the strong coupling between offshore waves and lagoon circulation.

There are no long-term wave observations available for Saipan with the nearest wave buoy located at Guam (www.ndbc.com). Ocean surface wave and wind data was therefore extracted from the ERA-interim global ocean model dataset for location 147.0°E and 16.5°N (www.ecmwf.int, accessed September 2010). The data show that the months from April to September are relatively calm and variable compared to the months from October to March (see Kruger *et al.* 2010 for details). The model was run using two scenarios based on these main variations in the wave climate.

2.3 Inter-annual variations

Significant low frequency oscillations on an inter-annual (more than a year) timescales include the El Nino-Southern Oscillation (ENSO) cycle. Generally, El Nino corresponds to low sea-level, and La Nina corresponds to high sea-level in western north Pacific. For example, during the strong El Nino event of 1997, the sea level was approximately 0.2 m lower than the long-term mean (Figure 4). This has implications for lagoon circulation and water renewal times as an elevated or depressed regional water level will modulate the wave-setup over the reef and allow for more or less wave-driven circulation in the lagoon, respectively.

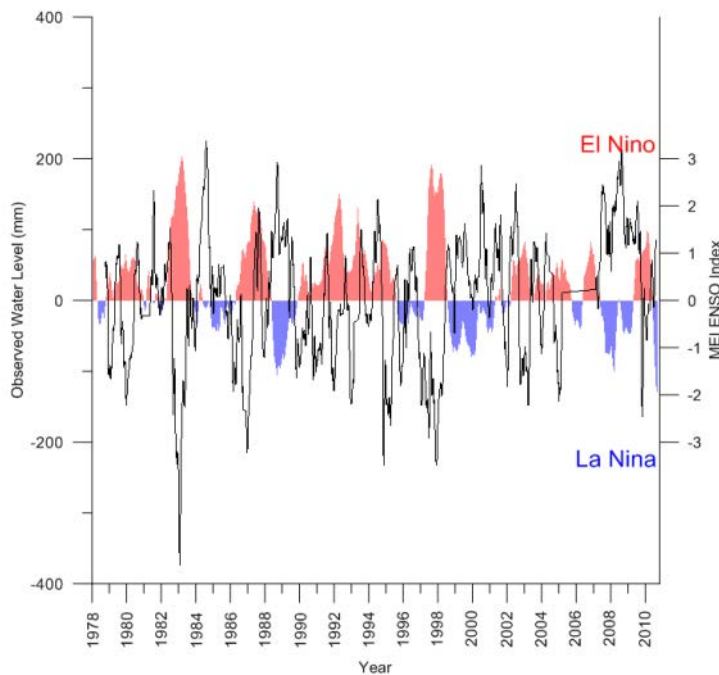


Figure 4. Time series plot of normalised monthly averaged tide gauge observations overlain on the multivariate ENSO Index. (source tide gauge: <http://ilikai.soest.hawaii.edu/uhsic/woce.html>; source MEI: <http://www.esrl.noaa.gov/psd/people/klaus.wolter/MEI/mei.html>, accessed October 2010).

3 METHODS

3.1 Physical Oceanography

SOPAC carried out an oceanographic survey of Saipan Lagoon from April to June 2010 (Figure 5) with the objective to collect sufficient data to allow the calibration of the 3D wave-current model (Kruger *et al.* 2010). The locations of the instruments were chosen in order to ascertain the role of the shipping channel in facilitating the exchange of water between the ocean and lagoon, and to understand the influence of offshore waves on the lagoon circulation. A profiler was placed near the Sadog Tasi outfall to increase the confidence on the plume dispersion processes.

Current velocities (speed and direction of water flow) were measured *in situ* using three Sontek Acoustic Doppler Current Profilers (ADPs), one Nortek Acoustic Wave and Current Meter (AWAC), and one Sontek Acoustic Doppler Velocimeter (ADV). Data from the ADP at the channel show that the flow of water is predominantly out of the lagoon at a mean speed of 13 cm/s, while data from the ADP in the lagoon show that the flow of water is predominantly to the southwest at a mean speed of 10 cm/s. The ADV shows that the current direction at Managaha Island is due south at slow magnitudes of 5 cm/s while the AWAC near the Sadog Tasi outfall shows water flow is approximately 3 cm/s in an ESE direction.

Surface wave parameters and water elevations were measured *in situ* using four RBR Tide and Wave Recorders, TWR-2050P. The TWR on the northern reef slope recorded wave heights between 0.5 to 0.8 m, with the majority of waves having a period of 8 s, while the northern reef flat TWR shows that wave heights and periods are strongly modulated by the tide. The TWR on the southern reef slope recorded wave heights of generally 0.2 m with a period of 8 s, while at the reef flat the wave heights, periods, and temperatures are strongly modulated by the tide with wave periods distinctly bi-modal with periods grouped at either less than 1 s or 5 s. The field data showed a strong coupling between incident wave forcing and lagoon circulation. Further details of this field survey can be found in the companion report by Kruger *et al.* (2010).

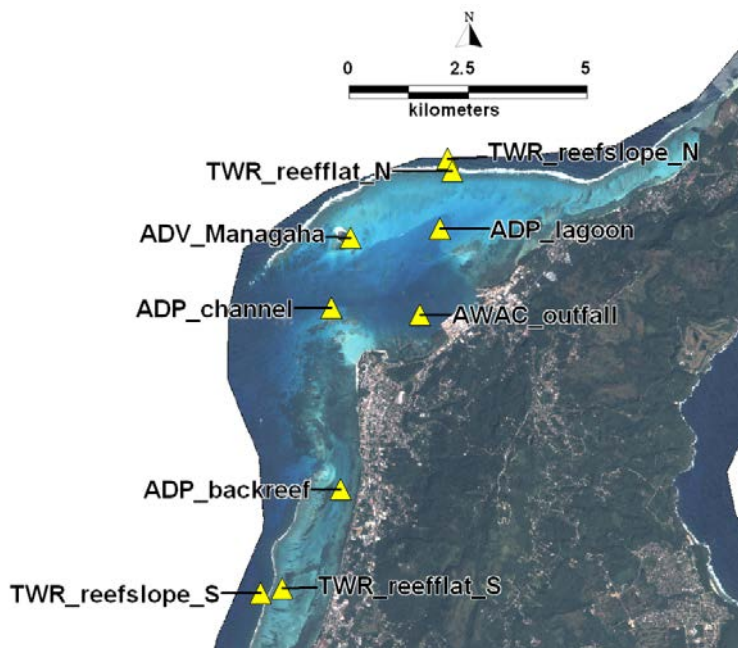


Figure 5. Equipment locations within Saipan Lagoon occupied from April to June 2010. Mooring stations are indicated by triangles with the following abbreviations: TWR, tide and wave recorder; ADV, acoustic Doppler velocimeter; ADP, acoustic Doppler profiler; AWAC, acoustic wave and current profiler. Note that the backreef ADP failed to record data. Figure from Kruger *et al.* (2010).

3.2 Three Dimensional Wave-Current Hydrodynamic Model

3.2.1 Model Description

The spectral wave model simulates the growth, decay and transformation of wind-generated waves and swells in offshore and coastal areas. The model includes wave growth by action of wind, non-linear wave-wave interaction, dissipation by white-capping, dissipation by wave breaking, dissipation due to bottom friction, refraction due to depth variations, and wave-current interaction. The second order stresses due to breaking of short period waves is included in the simulation. The radiation stresses act as driving forces for the mean flow and are used to calculate wave induced flow (source: www.mikebydhi.com, accessed October 2010).

The hydrodynamic model is based on the 3D Shallow water equations. The Temperature-Salinity module sets up additional transport equations for temperature and salinity. While temperature and salinity are initially constant, they vary in the domain due to fresh water discharge from the Sadog Tasi outfall and heat exchange processes between the atmosphere and the seawater. Additionally, the calculated temperature and salinity are fed back to the hydrodynamic equations through buoyancy-forcing induced by density gradients. The spatial and spectral discretisation is performed using a cell-centred finite volume method. The transport of material (i.e. fate of pollutants from the Sadog Tasi outfall) is based on an Eulerian approach, using forces derived from the 3D hydrodynamic model. Refer to www.mikebydhi.com for more information.

3.2.2 Gridded Domain

The domain was constructed with a combination of triangular and quadrangular meshes over a bathymetric dataset obtained from Pacific Islands Benthic Habitat Mapping Center (PIBHMC) as shown in Figure 6. Further details on the bathymetric dataset are given in Kruger *et al.* (2010).

The triangular mesh area varied in the domain to balance the accuracy of the calculation with computation time. Accordingly, the offshore region is described by a maximum triangular mesh area of 0.25 km^2 , equivalent to a 500 m grid, and the lagoon is described by a maximum triangular area of $10,000 \text{ m}^2$, equivalent to a 100 m grid.

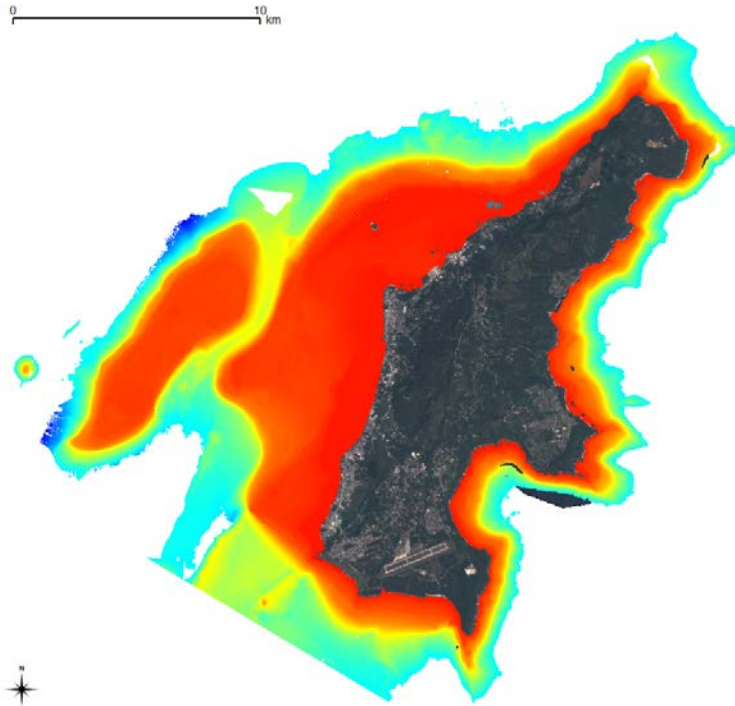


Figure 6. Composite bathymetry (LiDAR, multibeam and satellite derived sources) for Saipan Island. Shallow to deep waters (0 to 600 m) are shown as red to blue. Source: www.soest.hawaii.edu/pibhmc/.

The shallow water regions within the lagoon were further divided into four regions. Near the outfall, the mesh area is constrained to a maximum of $2,500\text{m}^2$, equivalent to a 50 m grid. The surf zone on the fringing reef system is typically narrow. Therefore a high resolution on the reef slope and reef flat is important to accurately account for wave-induced flow. Consequently, triangular mesh areas on the southern reef flat and reef slope were constrained to a maximum of $2,500\text{m}^2$. Offshore conditions dictate that the impacts from waves dominate on the northern barrier reef. A finer resolution with a maximum of $1,225\text{m}^2$ was therefore used to describe the northern reef slope, crest and flat. Additionally, in order to accurately represent the dredged channel, a quadrangular grid was introduced in the domain with a maximum stream length of 100 m and a maximum transversal length of 70 m.

In the vertical domain, a sigma layered mesh is applied as the schematic in Figure 8 shows. The vertical distribution of the layer is specified using a layer thickness attribute. The model is built vertically using four layers with the following proportional thickness, from the bottom to the surface: 0.25, 0.15, 0.45, and 0.15.

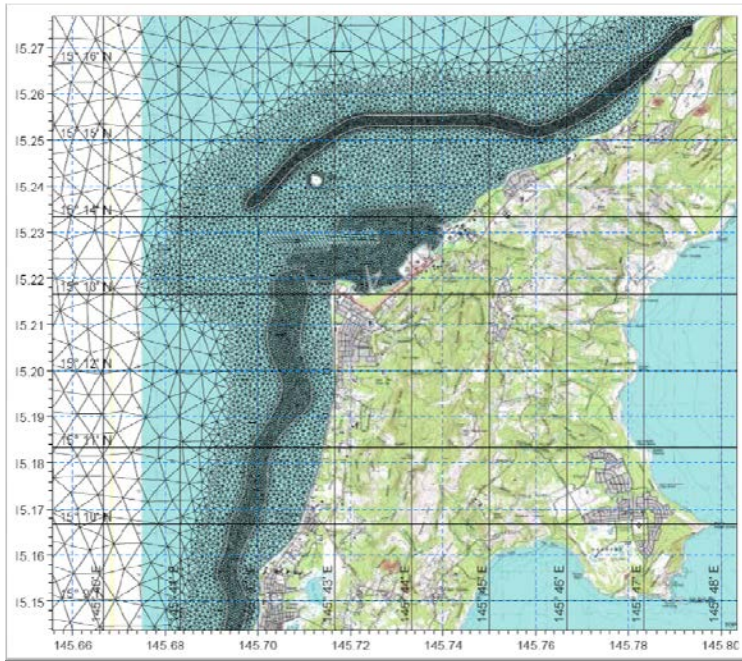


Figure 7. Detail of model grid showing finer mesh size over the reef areas and near the outfall, as well as the quadrangular mesh depicting the shipping channel. Backdrop is the Saipan topographic map, USGS 1999.

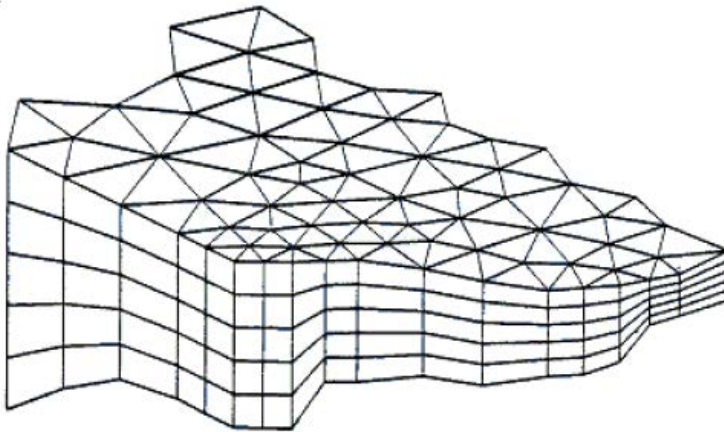


Figure 8. Example of a 3D mesh using sigma layers (source: DHI manual).

3.2.3 Model Calibration

The model was calibrated through the procedure shown in Figure 9, and by adjusting the bed roughness, eddy viscosity and wind friction. First, the wave model was calibrated against the wave data collected from the TWRs, namely, significant wave height (H_s), peak wave period (T_p), and time-averaged water level. A time series of radiation stress (the east and north components S_{xx} and S_{yy} , respectively, and the shear component S_{xy}) was extracted from each node of the wave model and included in the hydrodynamic model to account for wave forcing. Secondly, the resultant hydrodynamic model was calibrated against field data of current speed and direction from the ADPs and AWAC, as well as the water level data from the University of Hawaii tide gauge, and SOPAC deployed pressure sensors (TWRs). See Figure 5 for locations of these instruments.

Calibration results for the waves are shown in Figure 10, with good agreement between the observed and modelled values. Figure 11 shows the calibration results for the surface elevation on the reef slope and flat in the northern lagoon, with good agreement between the modelled and observed values. The model was also calibrated against the tide gauge data at the Saipan Harbour with good results between observed tide levels and modelled water levels (Figure 12). Current speed and direction profiles were recorded in three locations (see Figure 5), and the 3D model was calibrated for each site and each of the

near-bed, middle and surface layers. In each case there was good agreement between the observed and modelled velocity parameters as shown in Figure 13, Figure 14, Figure 15, and Figure 16.

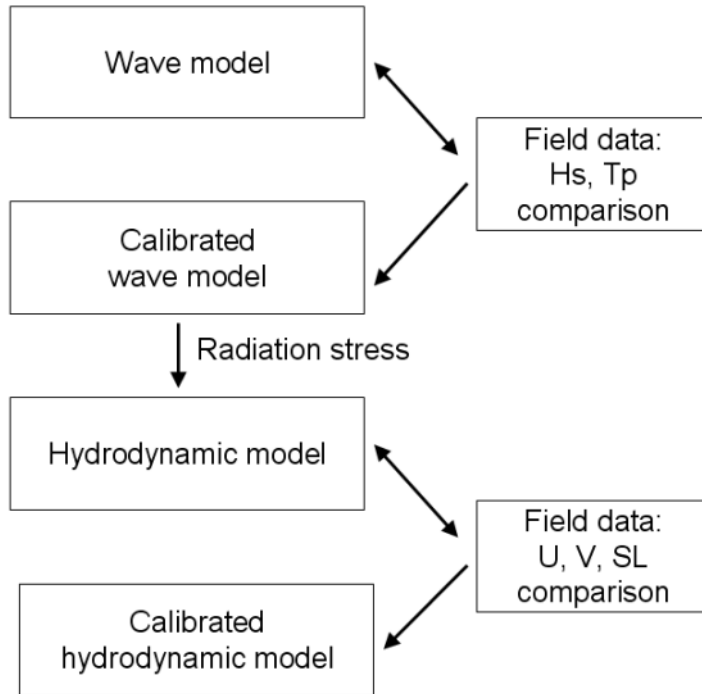


Figure 9. Flow chart showing the model calibration process. Wave height, Hs; wave period, Tp; current vector components, U and V; surface elevation, SL.

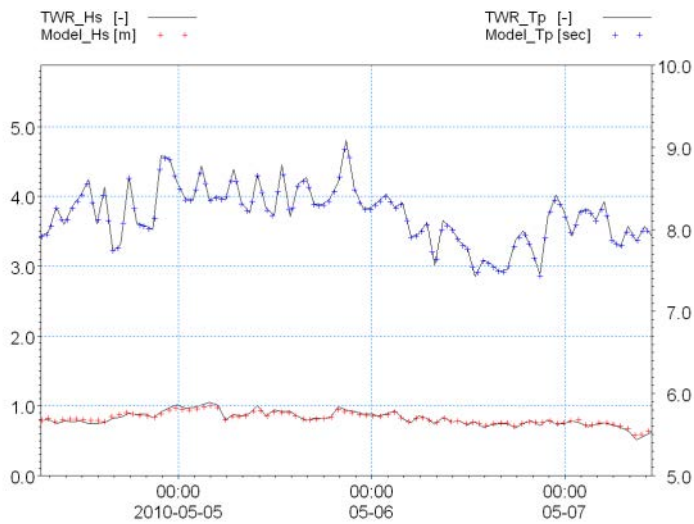


Figure 10. Time series of wave calibration for the wave gauge on the northern reef slope. Left y-axis shows significant wave height (Hs) for the model (red crosses) and corresponding observations from the wave gauge. The right y-axis shows peak wave period (Tp) from the model (blue crosses) and the corresponding wave gauge observations.

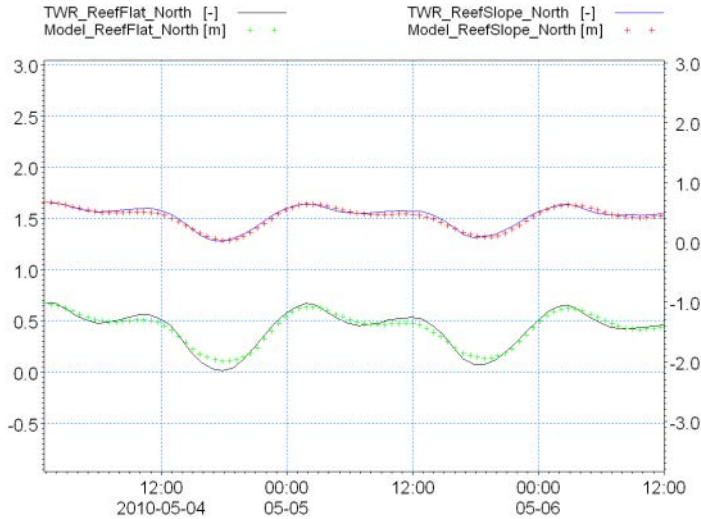


Figure 11. Time series of surface elevation calibration for the northern reef slope and flat. Left y-axis shows water elevation on the reef flat, and the right shows water elevations for the reef slope. Model output is shown as green and red crosses, respectively. The corresponding water level observations are shown as black and blue lines, respectively.

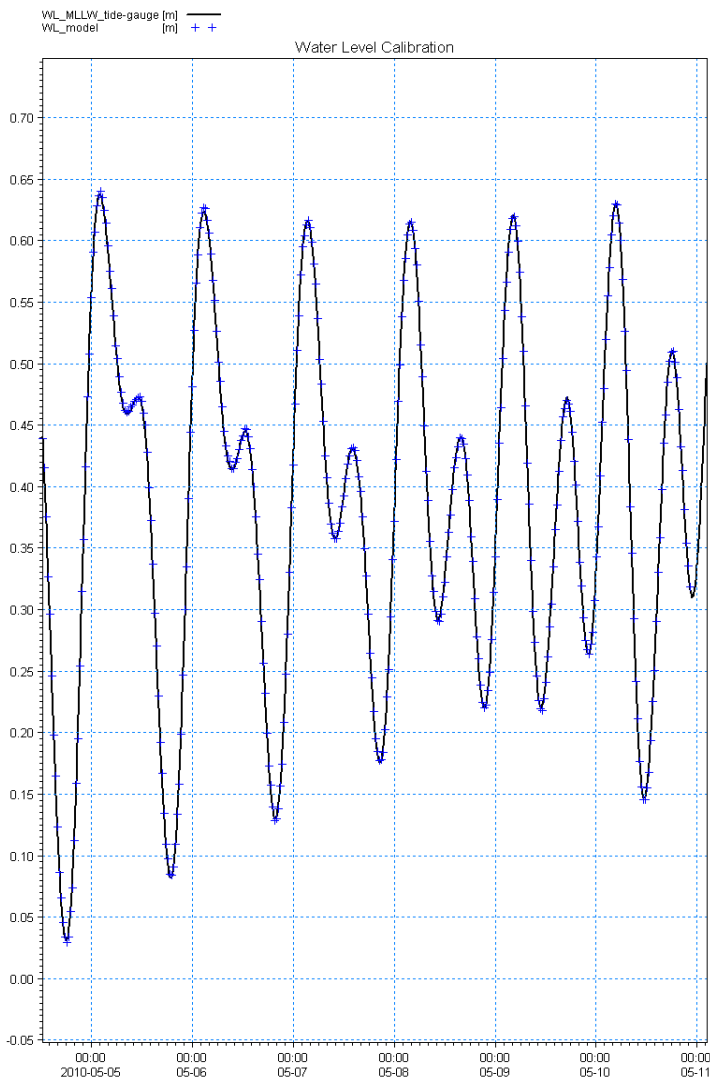


Figure 12. Time series of surface elevation observed at the tide gauge (black line), and corresponding model output (blue crosses).

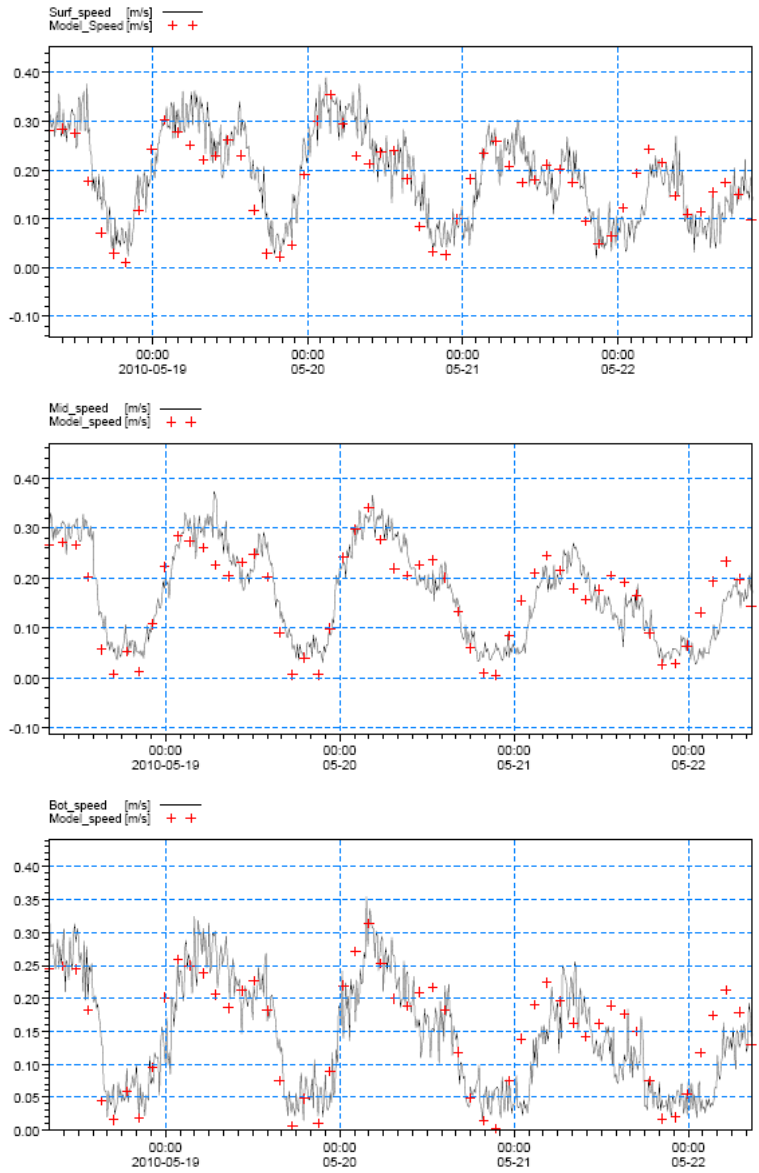


Figure 13. Calibration results between the observed current speed (black line) of the surface layer (top panel), mid water layer (centre panel), and near-bed layer (bottom panel), and those obtained from the model (crosses) for the ADP location in the channel.

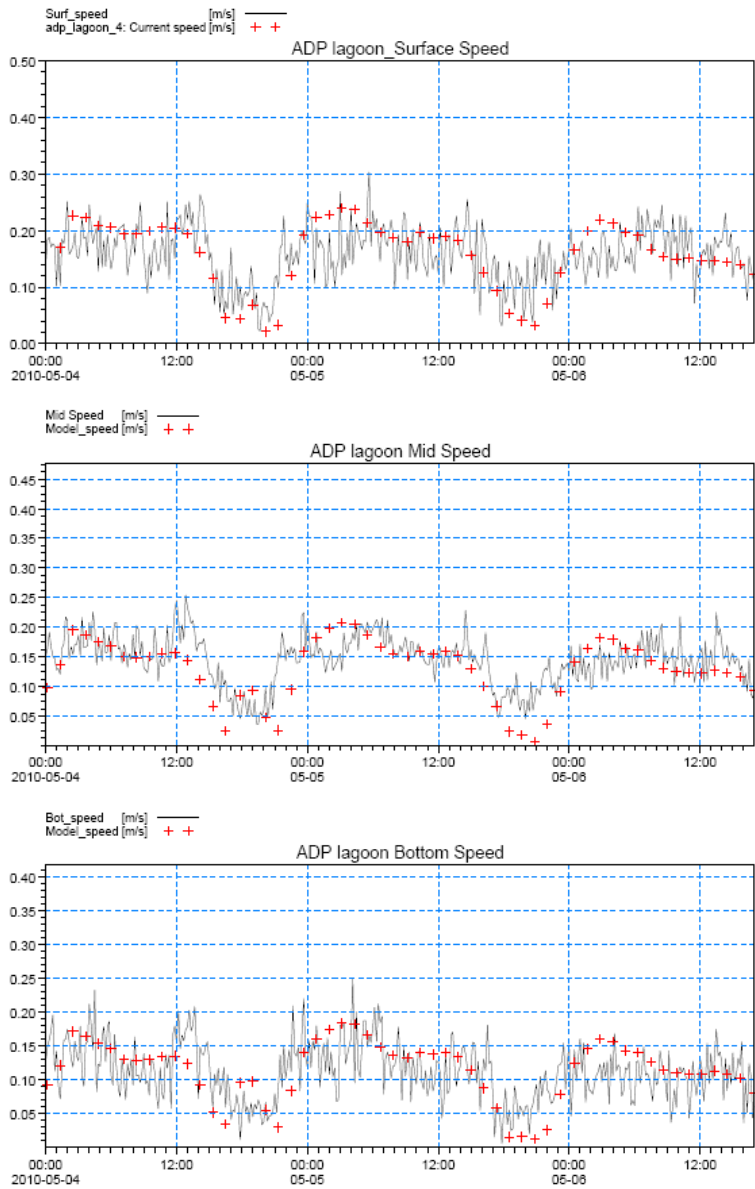


Figure 14. Calibration results between the observed current speed (black line) of the surface layer (top panel), mid water layer (centre panel), and near-bed layer (bottom panel), and those obtained from the model (crosses) for the ADP location in the lagoon.

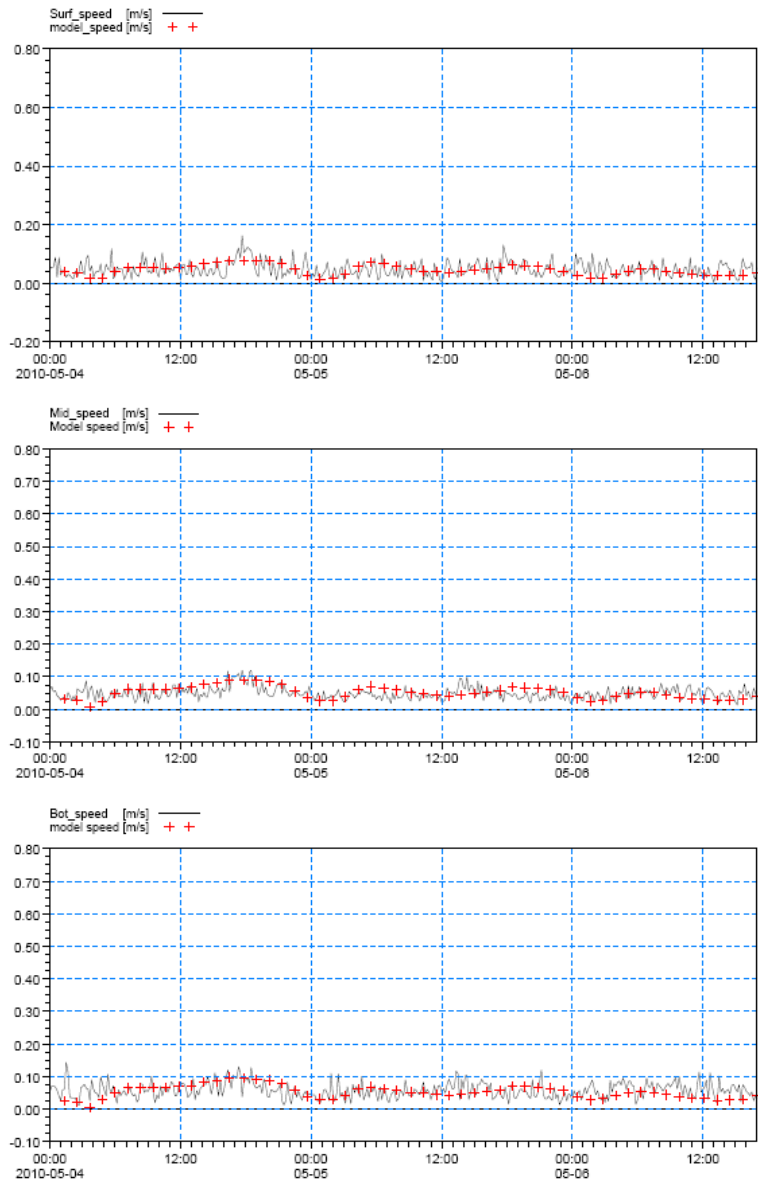


Figure 15. Calibration results between the observed current speed (black line) of the surface layer (top panel), mid water layer (centre panel), and near-bed layer (bottom panel), and those obtained from the model (crosses) for the AWAC near the outfall.

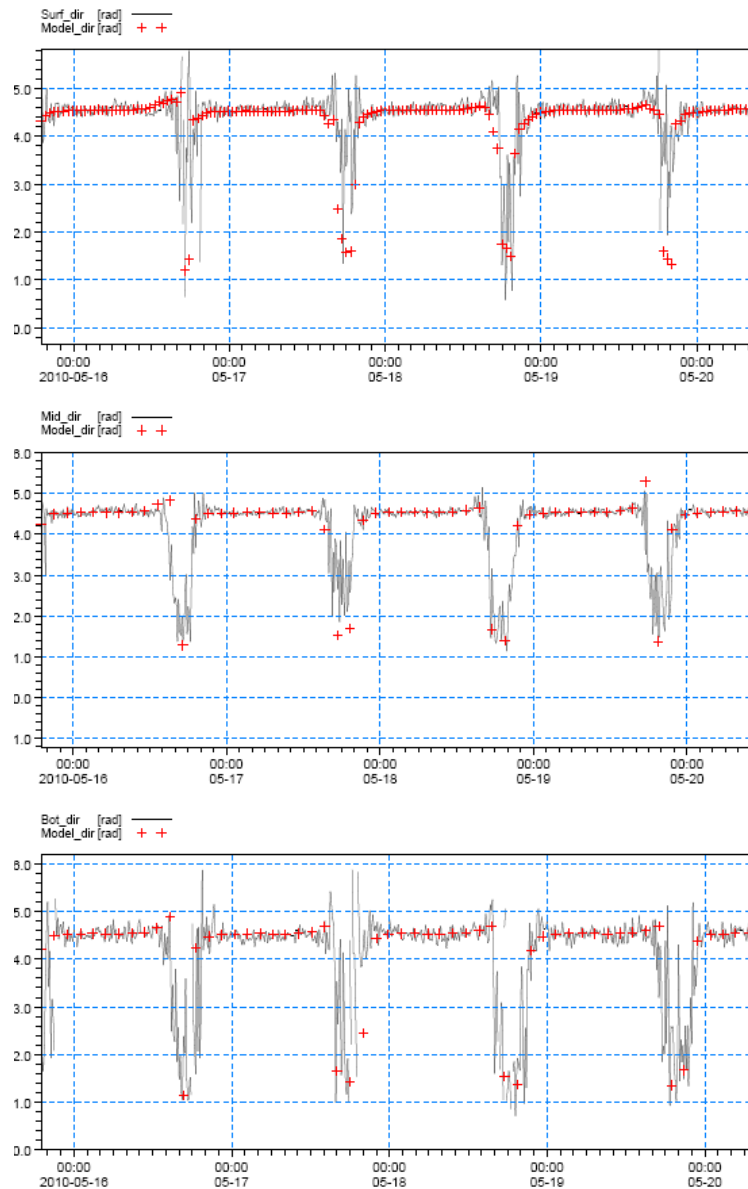


Figure 16. Calibration results for the observed current directions (line) of the surface layer (top panel), mid water layer (central panel), and near-bed layer (bottom panel), and those obtained from the model (crosses) for the ADP location in the channel.

While the hydrodynamic model was well calibrated and the drifting forces are well represented in the model, no direct calibration of the material transport model was possible. The initial dilution was estimated by the Commonwealth Utilities Corporation to be 77:1 based on the assumption that the receiving water is not stratified (H. Yelin pers. comm.). Since the material in the pipe immediately prior to discharge is equivalent to a concentration of 100%, an initial dilution of 77:1 would lead to a constant concentration of 1.3% in the water at the model cell containing the point source of the outfall.

This ratio was therefore used as a measureable indicator to test the behaviour of the plume dispersion in the model. This was done by extracting the concentration of the discharged material at two locations in the model for Scenario 2 (see below for the definition of model scenarios), one near the bed at the source, and one from the surface layer. The time series of the concentrations is shown in Figure 17. The figure shows that in the near bed layer the concentration of pollutants varies between 1.6% and 3.3%. At the surface, pollutant concentrations oscillate between 1.0% and 1.8%. More importantly, layer 3 (not shown in Figure 17), which accounts for 45% of the water column, has a mean concentration of 1.24%, equivalent to a dilution rate of 80.6. These values are in

agreement with an initial dilution of 77:1, and the plume model can therefore be assumed to be representative of the actual dispersion in at least the area near the outfall. In order to confirm plume dilution and dispersion in the far field it is recommended to map a plume of Rhodamine with a GPS-integrated fluorometer.

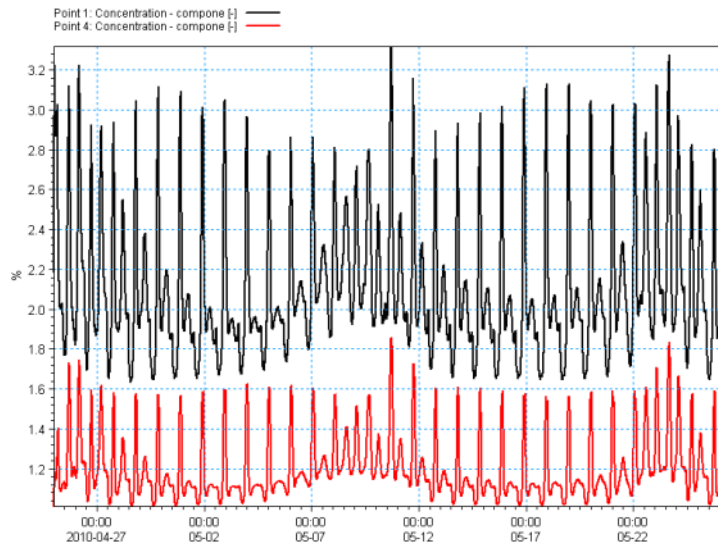


Figure 17. Time series of pollutant discharge concentration near the outfall as extracted from the model for the near bed layer (black), and surface layer (red). The source material has a concentration of 100%.

3.2.4 Model Scenarios

As discussed above under Section 2.2 the calibrated model was run using two seasonal scenarios:

- Scenario 1. Relatively high significant wave height with a south westerly wave and wind direction representative of conditions from October to March.
- Scenario 2. Relatively low significant wave height with a westerly wave and wind direction representative of conditions from April to September.

Further details of this approach can be gained from Figure 18, showing that two separate model streams were set up, one for each scenario. Each scenario was run for 30 days. In each case, the resultant 3D wave-current model was used to:

- inspect the dominant current patterns for each scenario, as presented in Sections 4.1,
- derive the dispersion of materials from the Sadog Tasi outfall, presented in Section 4.2, and
- derive the residual velocity fields, presented in Section 4.4.

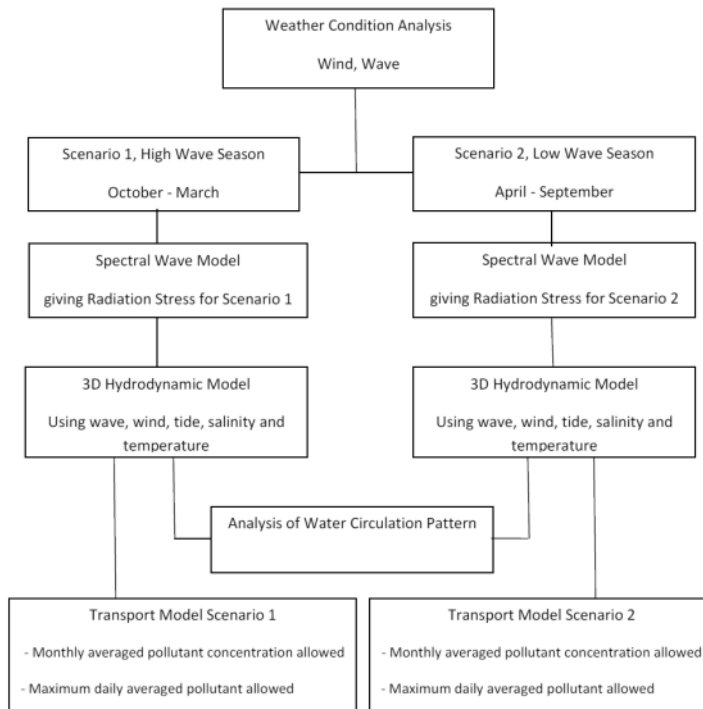


Figure 18. Chart outlining the work flow and model runs of the seasonal approach resulting in water circulation patterns (residual velocities) and plume dispersions for each of the two Scenarios.

The Sadog Tasi outfall was modelled as a point source in the bottom layer, continuously discharging into the lagoon. An effluent discharge rate of 4.8 MGD (or 0.21 m³/s) was chosen to represent the average daily design discharge through the 24 inch high density polyethylene pipe. The actual flow for the year 2009 averaged 2.9 MGD (H. Yelin, pers. comm.). At the time of discharge the material was given a temperature of 30°C and a salinity of 4.5 psu, which are parameters consistent with measured characteristics (H. Yelin, pers. comm.).

The model was used to look in detail at two types of discharge material. Firstly, the effluent was considered to be an imaginary substance with a concentration of 100 g/m³. The model was then used to investigate the diffusion of this plume in space and the variation of its concentration over time. Secondly, the discharge consisted of the 9 most common constituents (Nitrate, Total Nitrogen, Orthophosphate, Total Phosphorous, Unionized Ammonia, Copper, Nickel, Zink, TRC). This was further analysed by varying the concentration and keeping it constant according to the specific maximum monthly averaged concentration as stipulated in the 2008 Sadog Tasi permit on the one hand, and releasing the material with a daily constant concentration according to their specific maximum daily concentration allowed. Note that in this last case, a day of discharge is followed by one day of pollution free flow.

4 RESULTS

4.1 Water Circulation

This section shows water circulation patterns in Saipan lagoon as output from the 3D wave-current model depending on tidal, wave and wind stress forces related to each of the two scenarios.

4.1.1 Tanapag Lagoon

The northern Tanapag lagoon is the largest body of water on the west coast of Saipan with an approximate area of 19 km². This lagoon is characterized by a barrier reef in the northwest, with a reef crest height of 0 m (mean lower low water, MLLW), and the dredged channel in the south with a depth of approximately 12 m. The areas fronting the commercial dock area features the deepest part, with depth reaching 15 m (Figure 19). The northern region is shallower with depths of around 4 m.

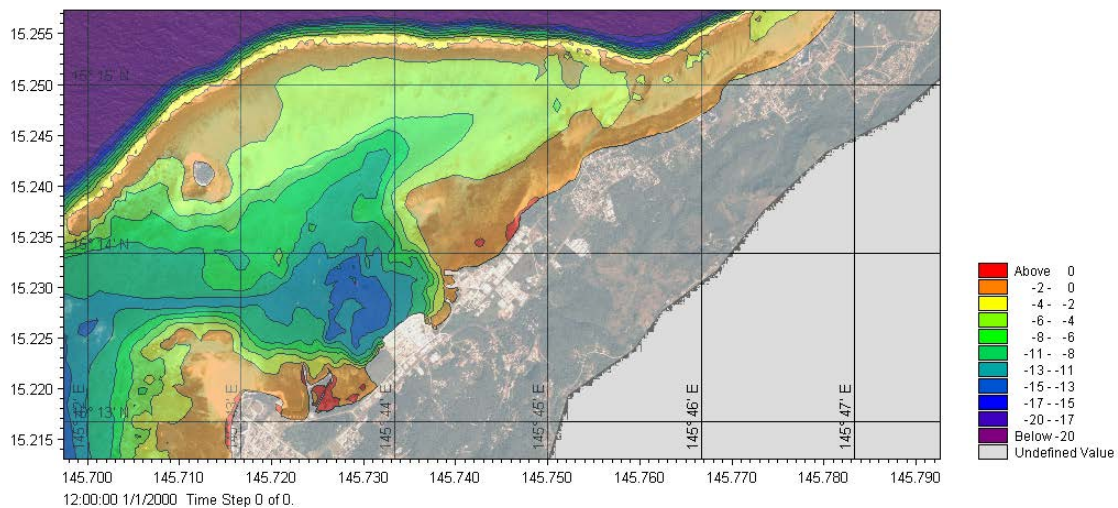


Figure 19. Bathymetry of Tanapag Lagoon. Water depths are red to blue, shallow to deep. Backdrop image is a 2005 Quickbird satellite image (source: CRMO).

As presented above, Scenario 1 (from October to March), is characterised by a strong southwest wave and wind field. Waves refract around the north of Saipan and break on the barrier reef. This is shown by the high radiation stresses in Figure 20. This induces a flow of water across the reef into the lagoon that controls water circulation in Tanapag lagoon. The water enters the lagoon across the northern reef and is flushed out through the channel or continues south past Point Muchot as shown in Figure 21. An influx of oceanic waters through the channel only occurs at spring low tide; when the northern reef falls dry (Figure 22). Current speeds are low (approx. 0.1 m/s) during this time compared to high tide conditions, when the westward current through the channel can exceed speeds of 0.5 m/s. Interestingly, the current direction along Muchot point is unidirectional towards the south throughout Scenario 1, without much influence of the stage of the tide. Also, the formation of an eddy in front of the port area is evident in both Figure 21 and Figure 22.

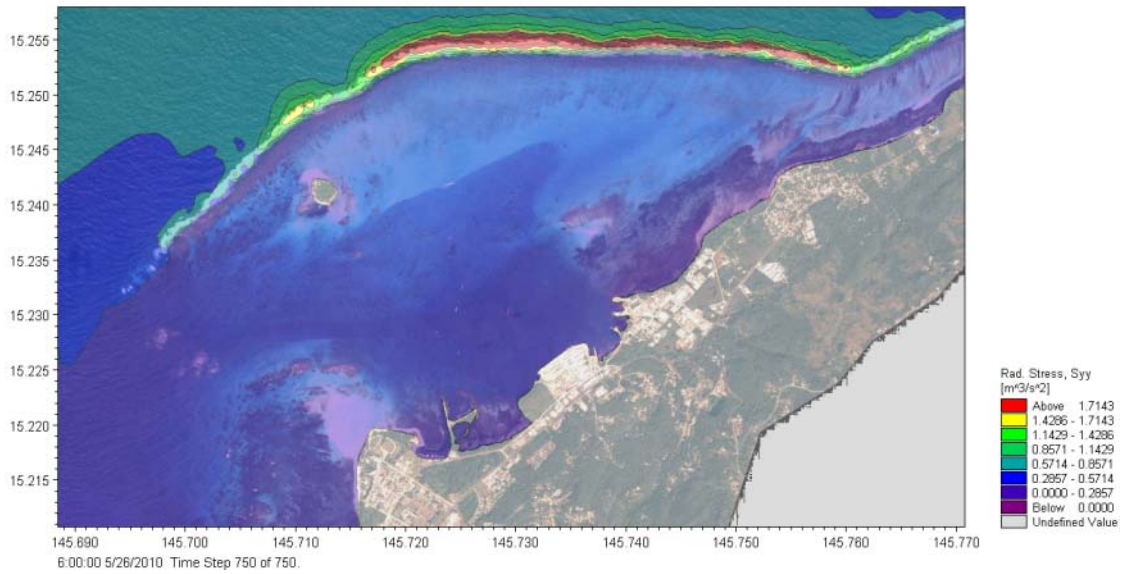


Figure 20. Snapshot of wave model output showing southward component of wave-induced radiation stress (S_{yy}) for Scenario 1. The highest stresses occur along the east-west trending barrier reef crest. Backdrop is a 2005 Quickbird satellite image (source: CRMO).

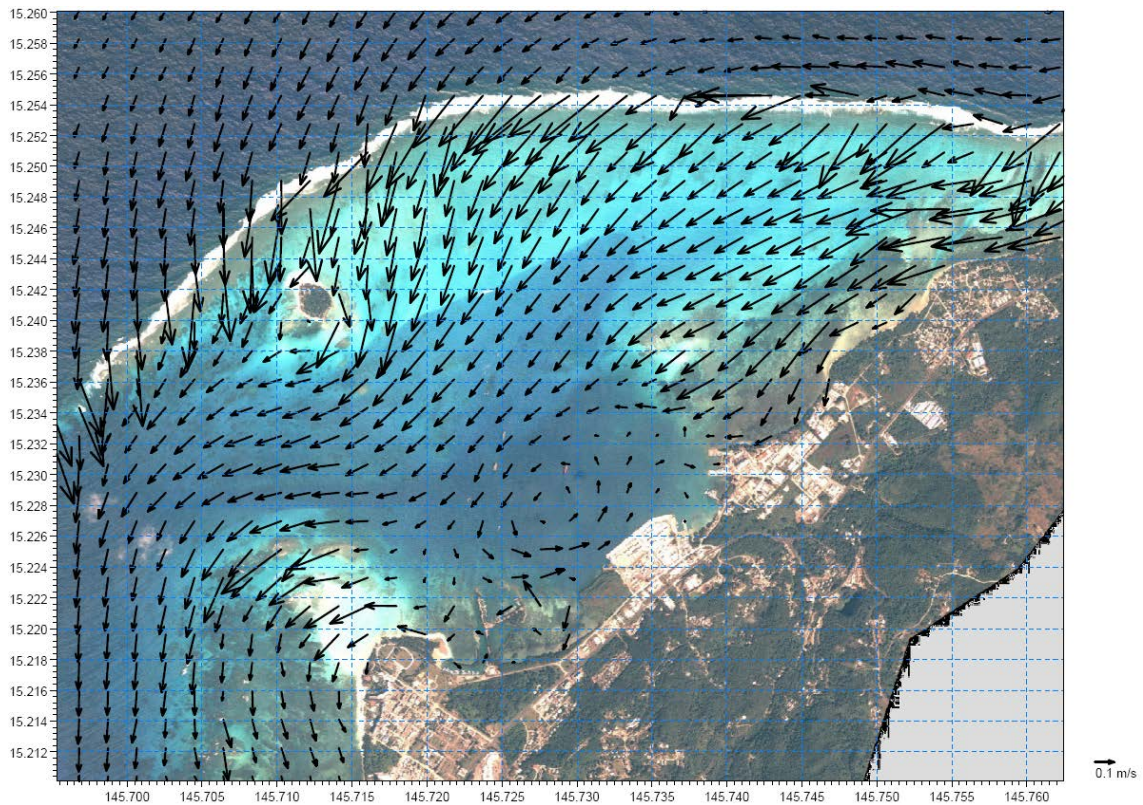


Figure 21. Snapshot of the dominant near bed current pattern in Tanapag Lagoon for Scenario 1, showing wave-driven flow across the northern barrier reef. Backdrop is a 2005 Quickbird satellite image (source: CRMO).

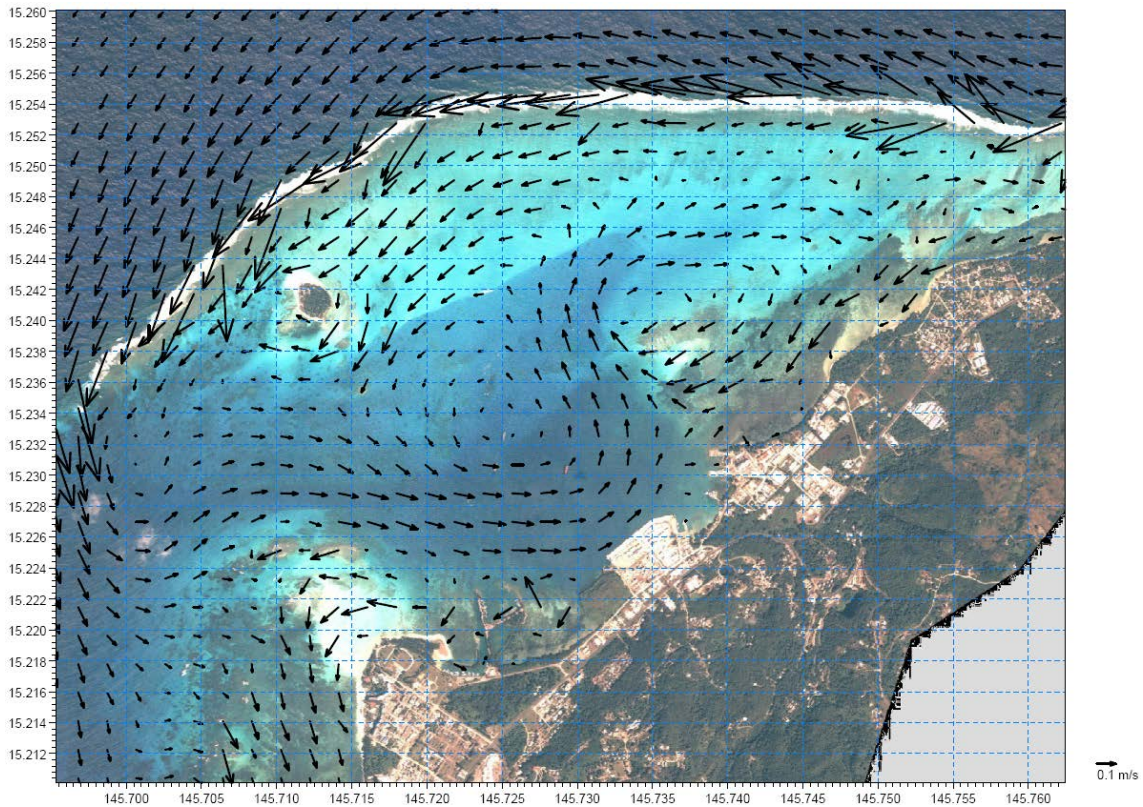


Figure 22. Snapshot of the near bed current pattern at spring low tide in Tanapag Lagoon for Scenario 1, showing lagoon-ward flow through the shipping channel. Backdrop is a 2005 Quickbird satellite image (source: CRMO).

Scenario 2, from March to October, is characterised by a moderate easterly wave and wind field. Radiation stresses on the northern barrier reef are generally much lower during this season (Figure 23) as a result of lower offshore wave height and a wave direction that requires more refraction as during Scenario 1.

The limited wave pumping across the reef generates much lower current speeds in the lagoon when compared to Scenario 1. On the ocean side, the wave field generates a southward current along the reef. A lower reef elevation at the southern tip of the barrier reef near Managaha Island allows this current to compete with the wave-induced southward flow inside the lagoon and forces water through the channel in a lagoon-ward direction (Figure 24). During this period, waves breaking on the northern barrier reef generate a southward current inside of the reef flat and around Managaha Island, while channel flush-in brings oceanic water toward the shore before veering northward along the shoreline. This shore-directed channel current entrains the southward flow west of Managaha Island into an anti-clockwise eddy, similar to the flow field evident during low spring tide in Scenario 1 (c.f. Figure 22).

It is only at the peak of the high tide that wave-induced flow dominates, strengthening the southward current in the lagoon. Especially the currents east of Managaha Island are positively affected (Figure 25). The model shows that when this current reaches its peak it can potentially overcome the ocean side current on the southern tip of the barrier reef. This circulation is similar to the dominant pattern identified under Scenario 1.

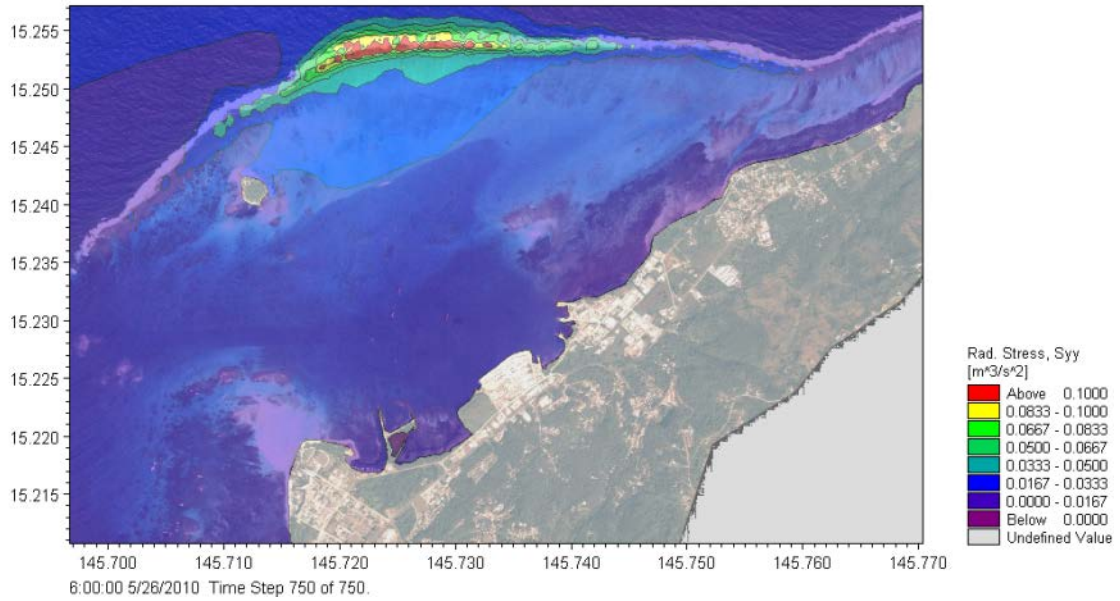


Figure 23. Snapshot of wave model output showing southward component of wave-induced radiation stress (S_{yy}) for Scenario 2. Backdrop is a 2005 Quickbird satellite image (source: CRMO).

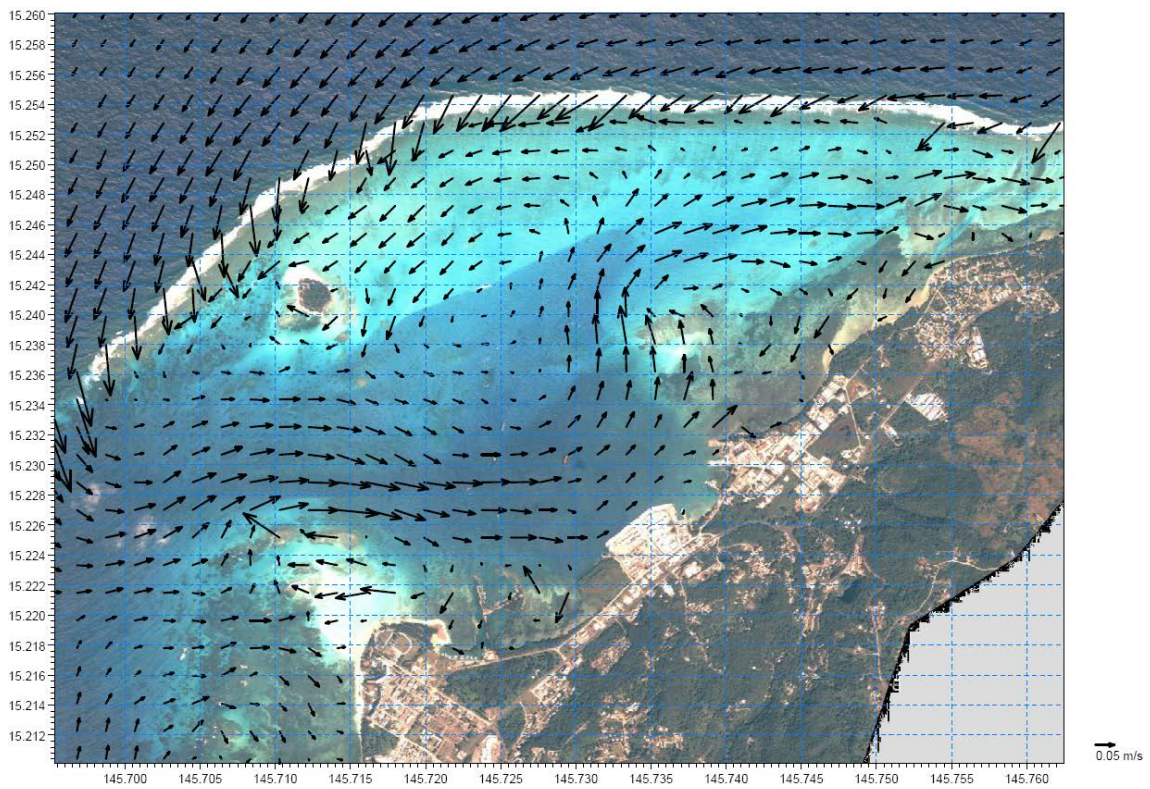


Figure 24. Snapshot of the dominant bed current pattern in Tanapag Lagoon for Scenario 2 showing lagoon-ward flow through the shipping channel. Backdrop is a 2005 Quickbird satellite image (source: CRMO).

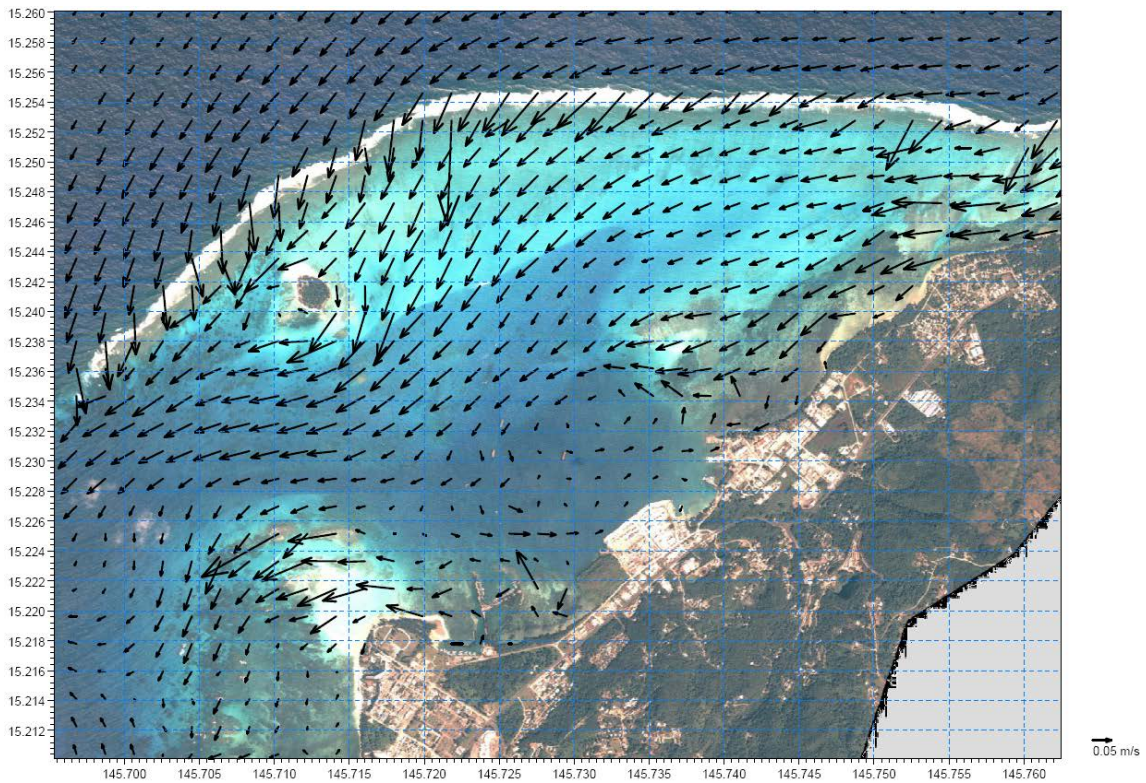


Figure 25. Snapshot of the near bed current pattern in Tanapag Lagoon at peak high tide for Scenario 2, showing influx of water over the northern reef and discharge through the shipping channel. Backdrop is a 2005 Quickbird satellite image (source: CRMO).

Time series of current speed and direction were extracted from the model at the three locations shown in Figure 26 in order to facilitate further comparison between conditions under Scenario 1 and Scenario 2.

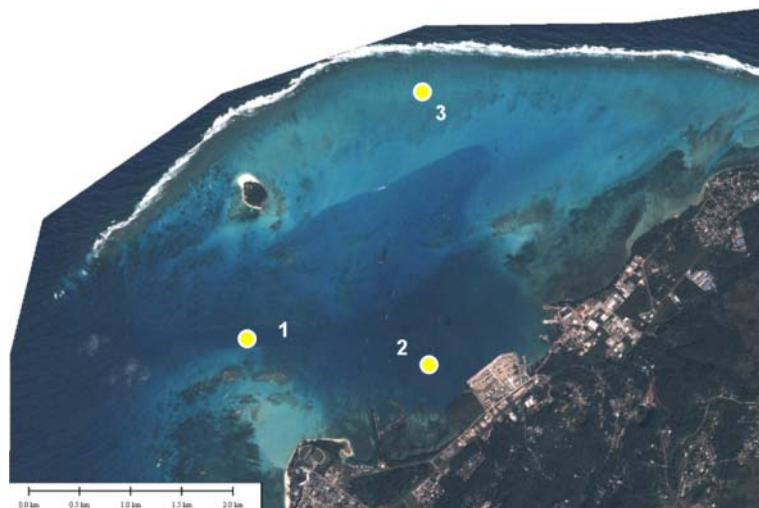


Figure 26. Locality diagram showing positions of model extraction points used to highlight the differences between scenarios 1 and 2, as well as the contribution of wind stress on the surface layer. The backdrop is a 2005 Quickbird satellite image provided by CRMO.

Figure 27 shows the data extracted for the point in the north of the lagoon, point three. Due to a stronger wave climate, current speeds during Scenario 1 are much stronger in this area, reaching values of 0.45 m/s as compared to <0.2 m/s during Scenario 2. However, the time series also shows a strong tidal modulation, with peak current occurring during high tides in both seasons as expected. By extrapolation, knowing that circulation in

Tanapag lagoon is mainly driven by offshore wave forces, overall current speed within the lagoon is much stronger under Scenario 1 than Scenario 2.

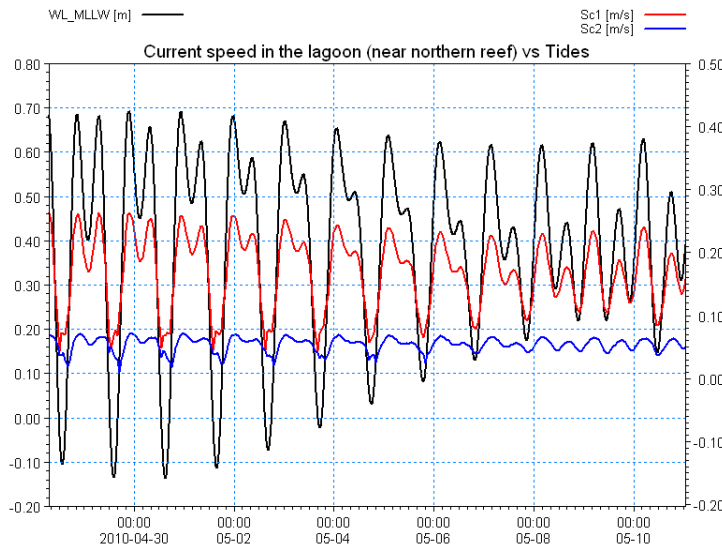


Figure 27. Comparative time series of observed surface elevation at the tide gauge (black line using the left y-axis) and current speeds extracted from the northern lagoon (point 3 in Figure 26) for Scenario 1 (red) and Scenario 2 (blue), using the right y-axis.

Figure 28 shows the current directions extracted from the model at the shipping channel, point one in Figure 26, which highlights the dominant current patterns described above. Water is mainly pumped into the lagoon by wave action and exits via the channel under Scenario 1. Minor oceanic inflow occurs only during spring ebb tide and for less than five hours per day. The important factor is that the water level does not drop under 0.1 m during neap tide (with the reef elevation at 0 m relative to MLLW), leading to permanent wave pumping and westward flux through the channel. A reverse observation can be made for Scenario 2. An east-directed inward flux of oceanic waters dominates, with outward flushing occurring for less than four hours a day during leading ebb periods.

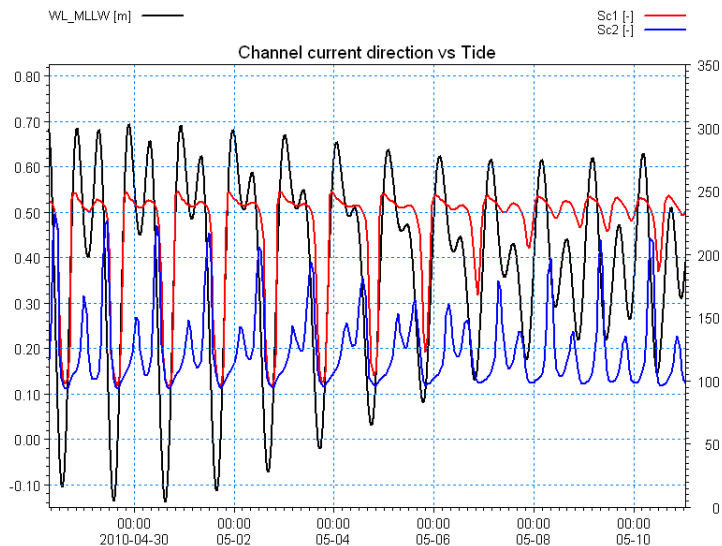


Figure 28. Comparative time series of observed surface elevation at the tide gauge (black line using the left y-axis), and current direction extracted from the model in the shipping channel for Scenario 1 (red) and Scenario 2 (blue), using the right y-axis.

Wind stress also plays an important role in the water circulation, with a significant contribution on the surface layer. The contribution fades through the water column following a logarithmic profile. Easterly winds blowing over Tanapag lagoon induce a current aligned with the wind direction generated by friction on the water surface. The contribution of the wind stress is exemplified using Figure 29, Figure 30, and Figure 31 by comparing the near bed layer and the surface layers velocities for Scenario 2 at the three sites shown in Figure 26, the channel, outfall, and northern lagoon, respectively.

As highlighted above, lagoon-ward currents dominate in the near bed layer of the channel during Scenario 2. However, winds blowing from east to west across the lagoon induce an opposing current in the surface layer. Figure 29 shows that during peak high tide, when wave-induced currents and wind-generated currents align and flow out of the channel, the surface current speeds exceed the weaker near-bed current. When current speed in the bottom layer is strong, which happens during low tide, wind stress forces (directed toward the west) oppose the direction of the surface layer current (flowing east and into the lagoon) and significantly reduce current speeds of the surface layer (during spring tide) and even reverse surface current directions (during neap tide).

Near the outfall (Figure 30), current speed is weak (in the order of 1 to 4 cm/s, surface to near bed, respectively) resulting in a strong three dimensional profile with the surface layer being controlled by the easterly wind friction. Finally, near the shoals of the northern lagoon (Figure 31), the surface currents are greater than the near-bed currents, and directions are aligned.

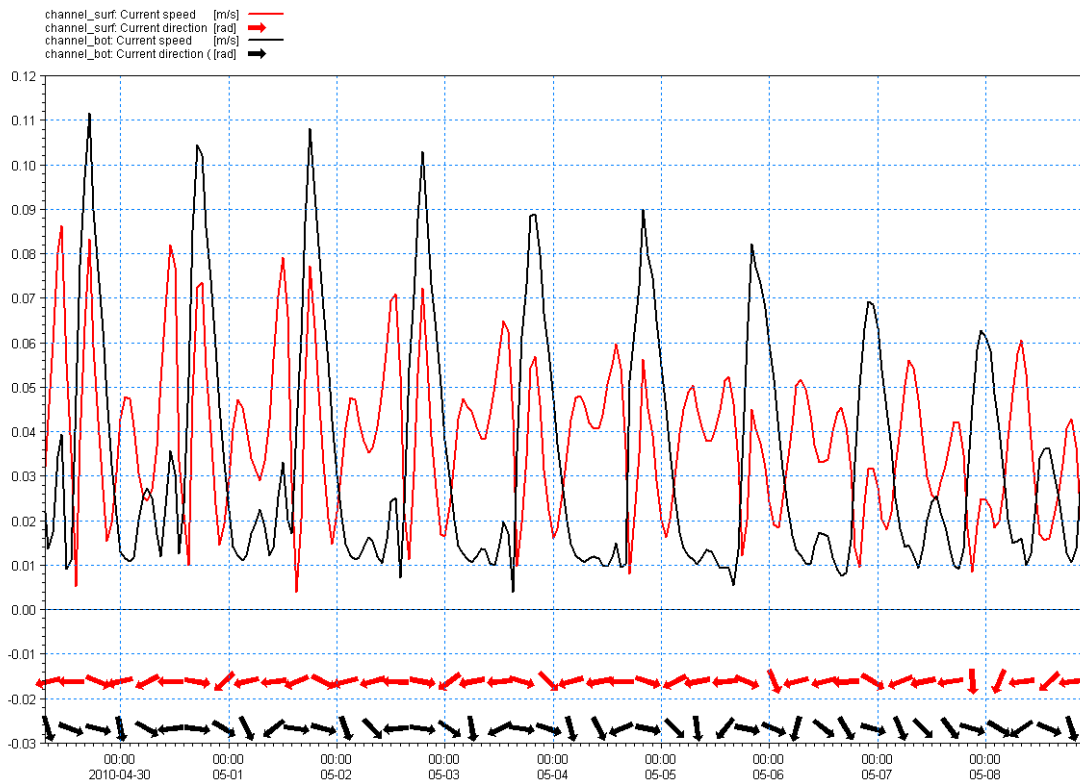


Figure 29. Time series (spring to neap tide) comparing the surface (red) and bottom (black) layer current speed and direction for Scenario 2 in the shipping channel at location 1 in Figure 26.

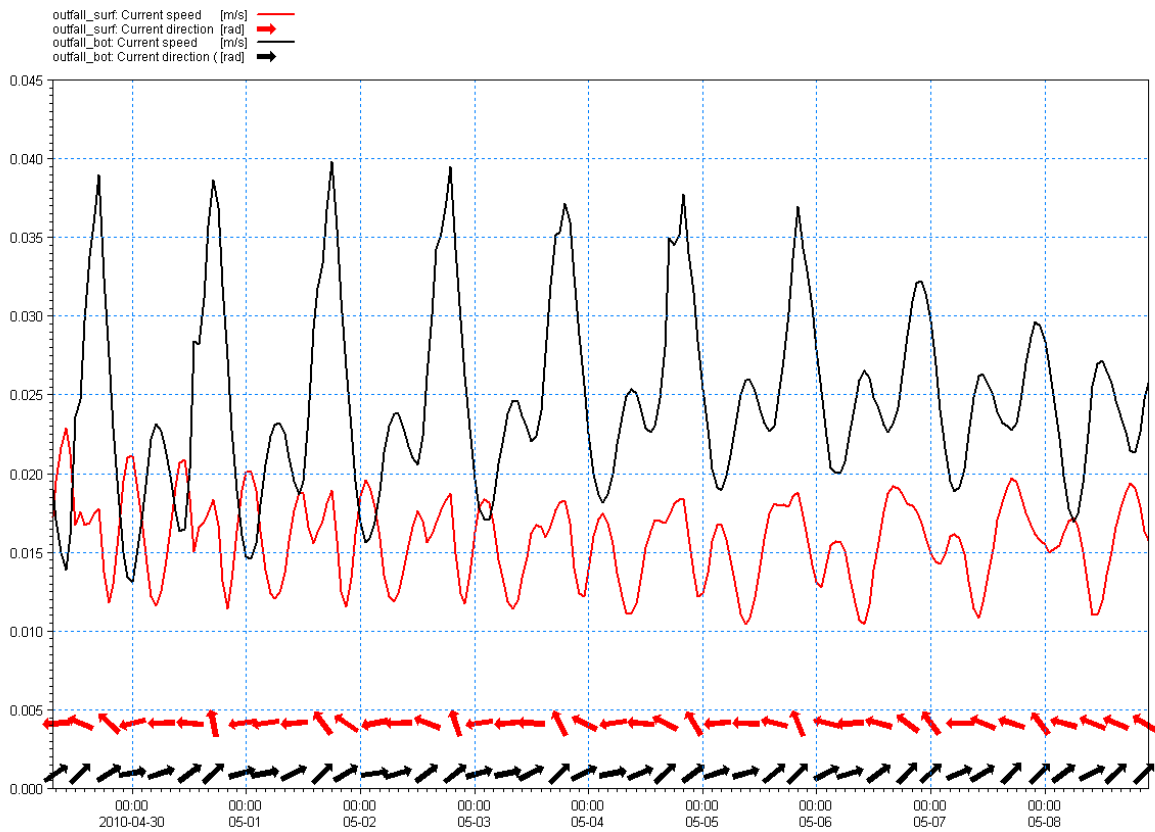


Figure 30. Time series (spring to neap tide) comparing the surface (red) and bottom (black) layer current speed and direction for Scenario 2 near the outfall at location 2 in Figure 26.

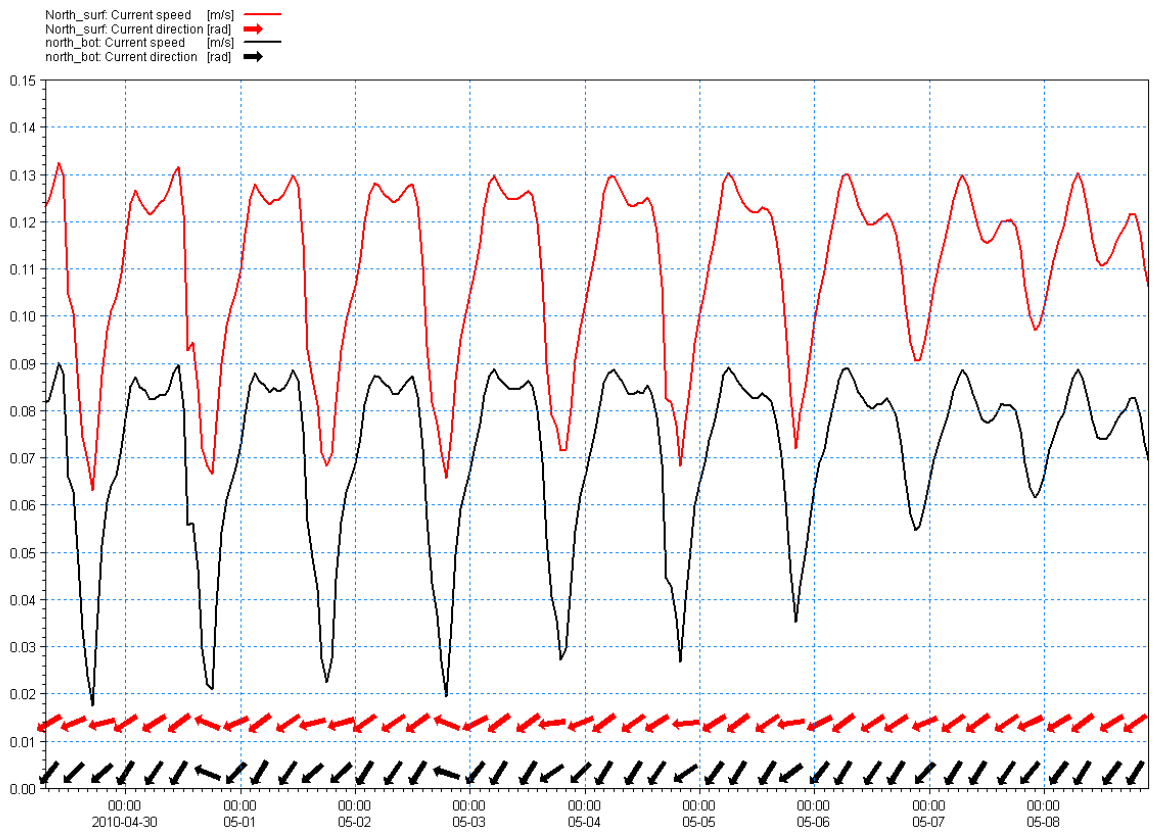


Figure 31. Time series (spring to neap tide) comparing the surface (red) and bottom (black) layer current speed and direction for Scenario 2 in the lagoon at location 3 in Figure 26.

4.1.2 Garapan Lagoon

Garapan lagoon is located south of Tanapag lagoon, along the centre of Saipan's western shoreline, between Point Muchot and the Sugar dock channel at Susupe. This lagoon is shallow with large areas being less than 1 m in water depth. The region in the north of the lagoon is deeper, with a maximum depth of 4 m near Garapan Dock (Figure 32). Additionally the north region is more open to the ocean with a scattered morphology of patch reefs which receive most of the wave energy as shown in Figure 33. The reefs in the south of Garapan lagoon are significantly lower (0.5 m below MLLW) compared to elsewhere. Relatively deep channels through the reef (maximum depth of approximately 3 m) are located at Garapan dock near the abandoned lighthouse, and at Sugar Dock, Susupe.

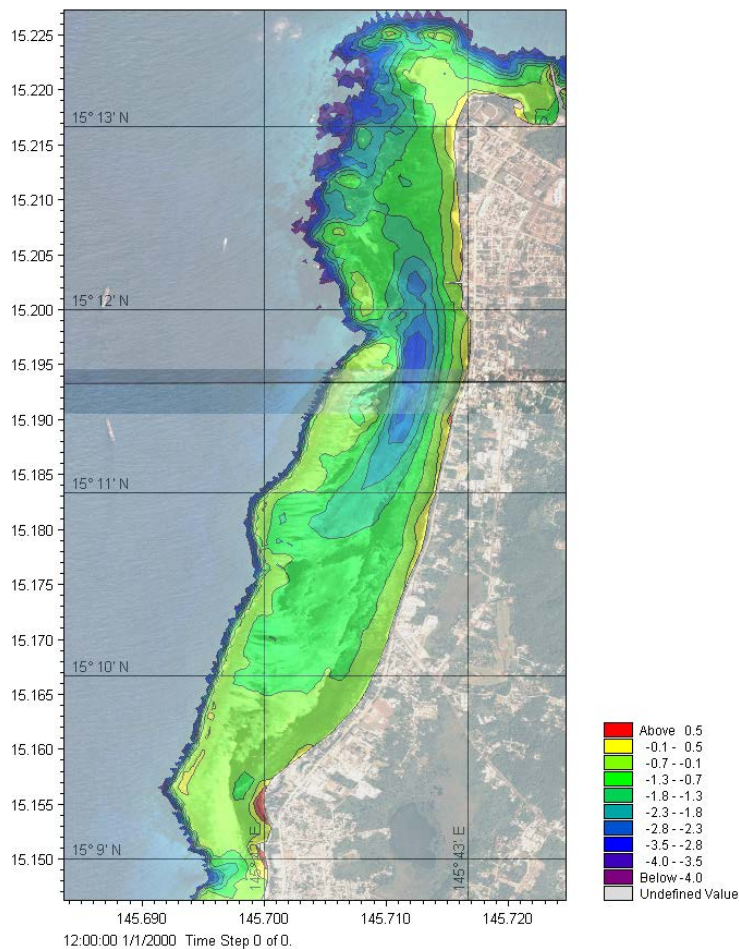


Figure 32. Bathymetry of Garapan Lagoon. Water depths are red to blue, shallow to deep. Backdrop image is a 2005 Quickbird satellite image (source: CRMO).

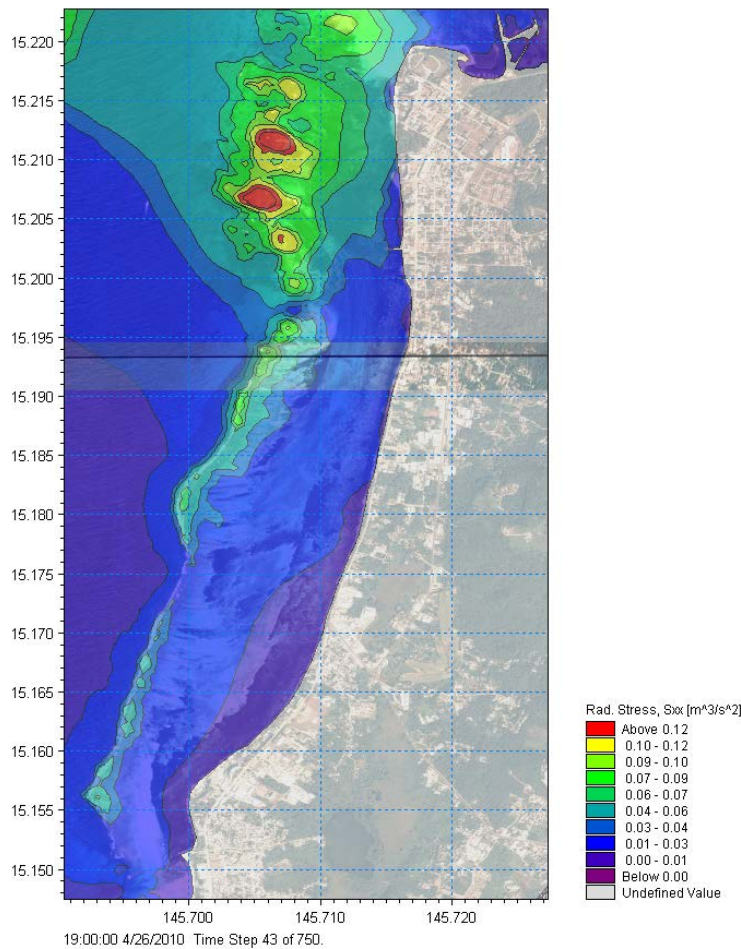


Figure 33. Snapshot of wave model output showing eastward component of wave-induced radiation stress (S_{xx}) for Season 1. Backdrop is a 2005 Quickbird satellite image (source: CRMO).

Figure 34 shows the near-bed circulation in Garapan lagoon during Scenario 1 (relatively high energy season). As Garapan lagoon adjoins Tanapag lagoon to the south it is significantly influenced by the southward currents past Point Muchot. Section 4.1.1 provided details of the water circulation in Tanapag lagoon, including a discussion on the two circulation patterns, 1. a dominant pattern controlled by wave pumping over the northern barrier reef and, 2. a minor pattern occurring during spring low tide, when the barrier reef falls dry, enabling ocean waters to enter the lagoon via an eastward current through the channel. When wave-pumping dominates in Tanapag lagoon, a relatively strong wave-induced current (<0.4 m/s) is evident at Muchot point, pushing water into Garapan lagoon from the north (Figure 34). Additional wave pumping occurs as a result of the north-easterly wave field refracting and breaking over the northern patch reefs of Garapan lagoon (Figure 33). These factors contribute to a south-directed current field within Garapan lagoon.

At low spring tide, the reef fronting Garapan inhibits wave pumping as shown by the current pattern in Figure 35. During this stage of the tide, the southward currents from Tanapag lagoon are also reduced in strength (c.f. Figure 22), minimising the water flow entering Garapan lagoon via Muchot point. However, the hydraulic gradient (ponding of waters within the lagoon) is sufficient to force water to exit the lagoon through the Garapan and Sugar Dock channels.

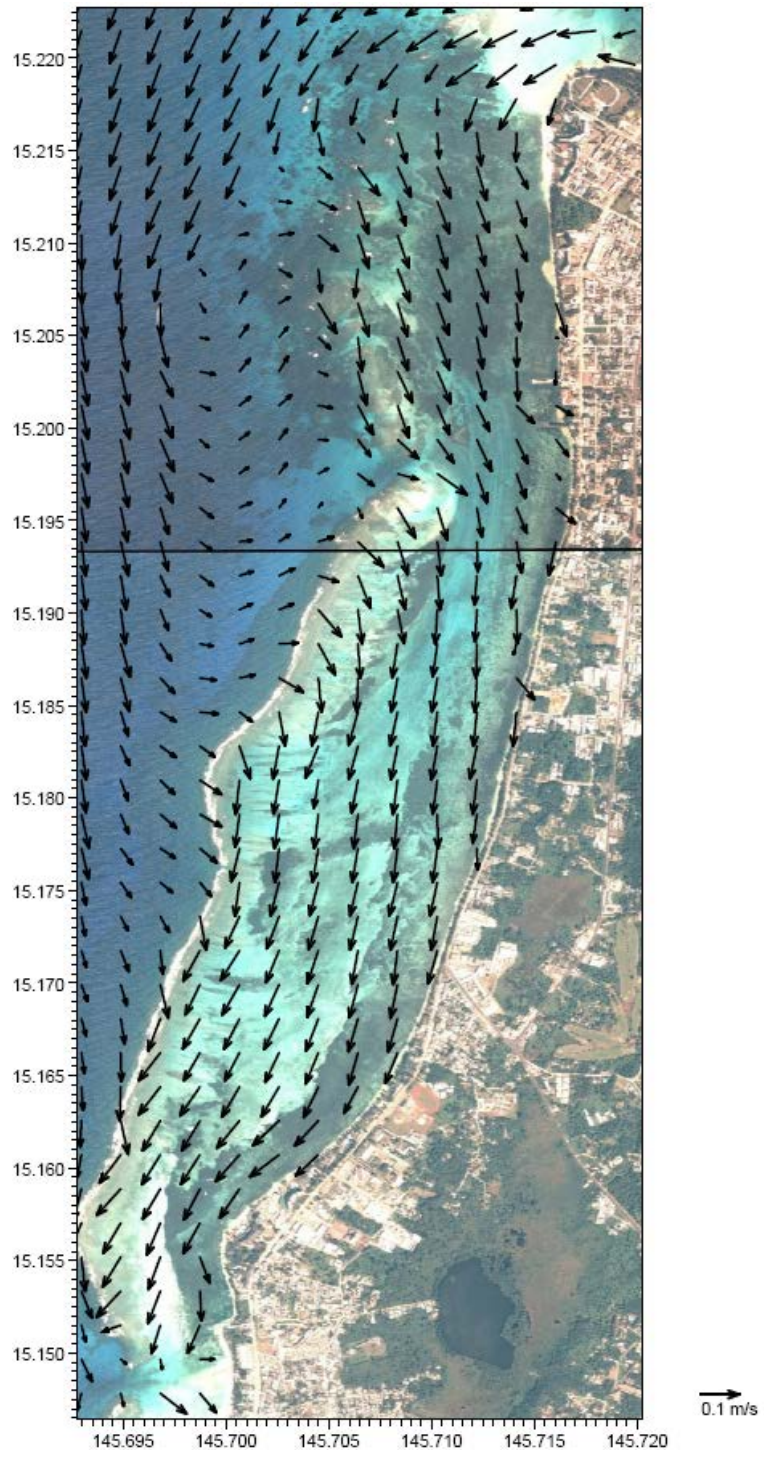


Figure 34. Snapshot of the dominant near bed current pattern in Garapan lagoon during Scenario 1 showing southward water flow. Backdrop is a 2005 Quickbird satellite image (source: CRMO).

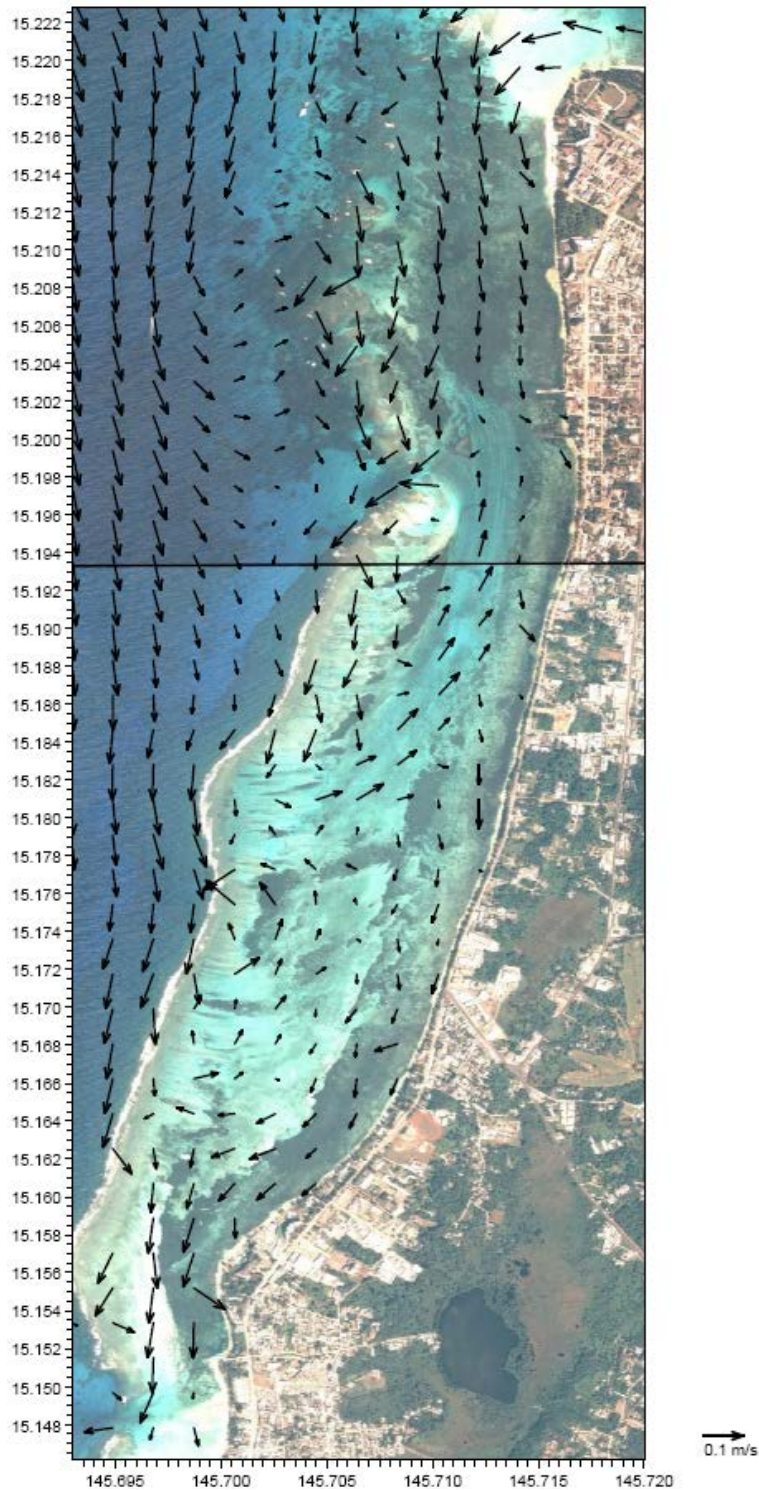


Figure 35. Snapshot of the near bed current pattern during low tide in Garapan lagoon during Scenario 1, showing outward flow through the Garapan and Sugar Dock channels. Backdrop is a 2005 Quickbird satellite image (source: CRMO).

Figure 36 shows current directions extracted from the model in the thalweg of Garapan (North Channel in the figure) and Sugar Dock (called south channel in the figure) channels. The figure highlights the change in current direction in the Garapan channel at low tide, from inward to outward directed flow, as per the forcing conditions discussed above. This also shows that the inward flux through Garapan channel dominates with outward flow occurring only for approximately two hours per day during low tide. Current direction extracted in the Sugar Dock channel shows that the channel is by-passed and waters continue southward into Chalan Kanoa lagoon.

The Sugar Dock channel also shows increasing influence due to tidal forcing. The dominant southward flow of water from Garapan to Chalan Kanoa lagoon is interrupted for approximately two hours per day during peak ebb phases when waters enter through Sugar Dock channel and veer south, bringing oceanic waters into Chalan Kanoa lagoon (Figure 37).

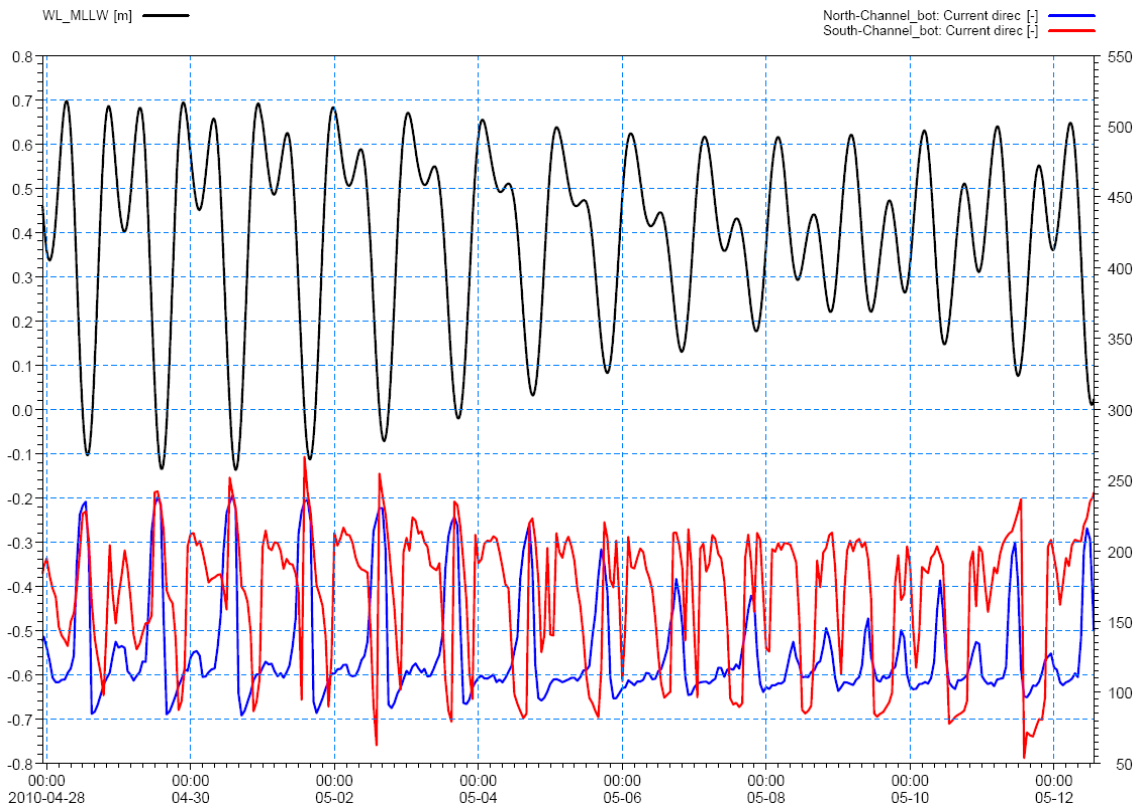


Figure 36. Comparative time series of observed surface elevation at the tide gauge (black line using the left y-axis); and current speeds extracted from the Garapan and Sugar Dock channels shown in blue and red, respectively.

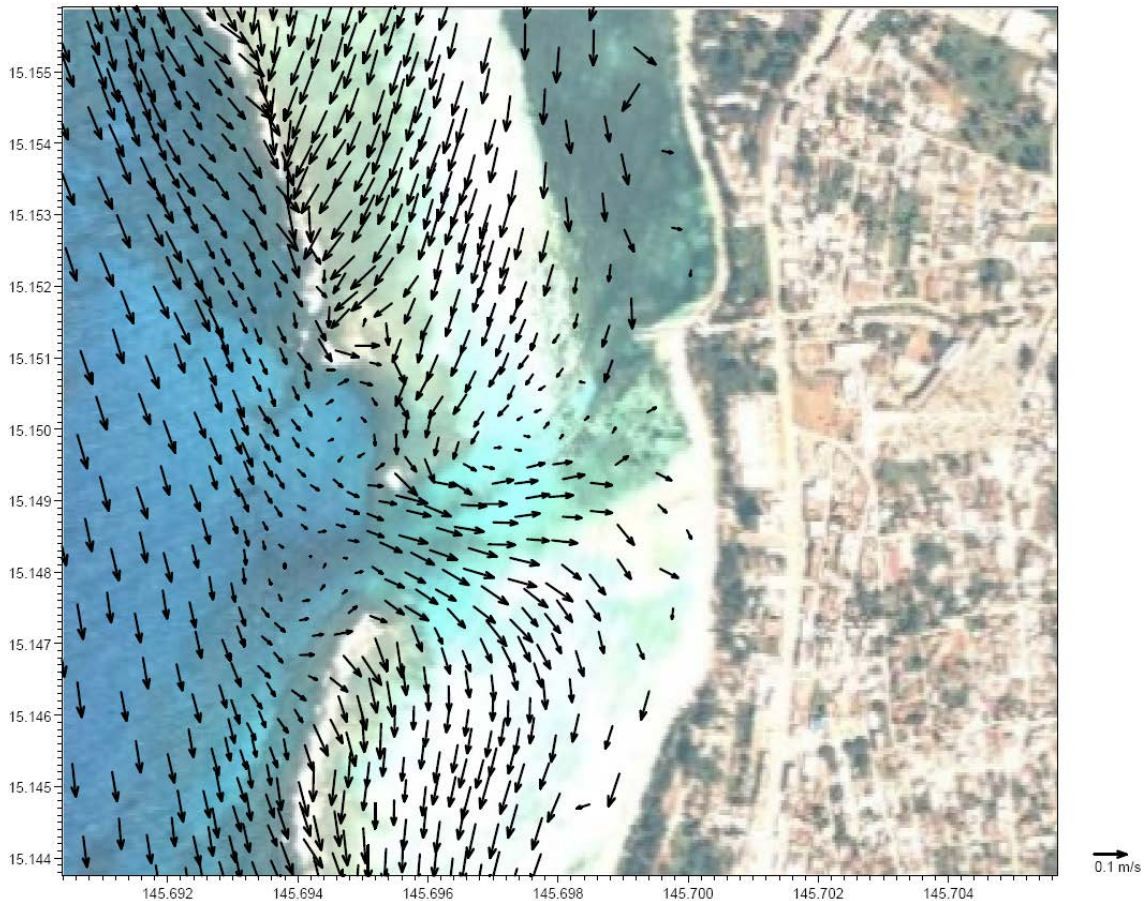


Figure 37. Close up of the Sugar Dock and channel, showing near bed lagoon-ward flow for Scenario 1. This condition exists for approximately two hours per day during periods of spring tides, and longer during neap tides. Backdrop image is a 2005 Quickbird image (source: CRMO).

The influence of wave-induced currents on Garapan lagoon is significantly reduced due to the lower offshore wave energy in Scenario 2 (Figure 38), although the dominant flux is still inward and southward (Figure 39). When high tide reaches its peak, flow induced by waves breaking on the northern barrier reef of Tanapag lagoon set up a preferred outward flow through the shipping channel. As a result, the waters in the northern region of Garapan lagoon, from Muchot point to the Garapan Dock, begin to stagnate (see Figure 40).

At low spring tide, the barrier reef in Garapan lagoon dries up, effectively turning off the dominant wave pumping regime (Figure 41). Additionally, wave pumping also stops across the northern barrier reef in Tanapag lagoon, which reduces water flow entering Garapan lagoon via Muchot point. However, the surface elevation in the lagoon is still higher than the surrounding ocean elevation, and the surface gradient acts to force water outward across the patch reefs in the northern part of Garapan lagoon. In the channels, hydraulic gradient and tidal forces compete.

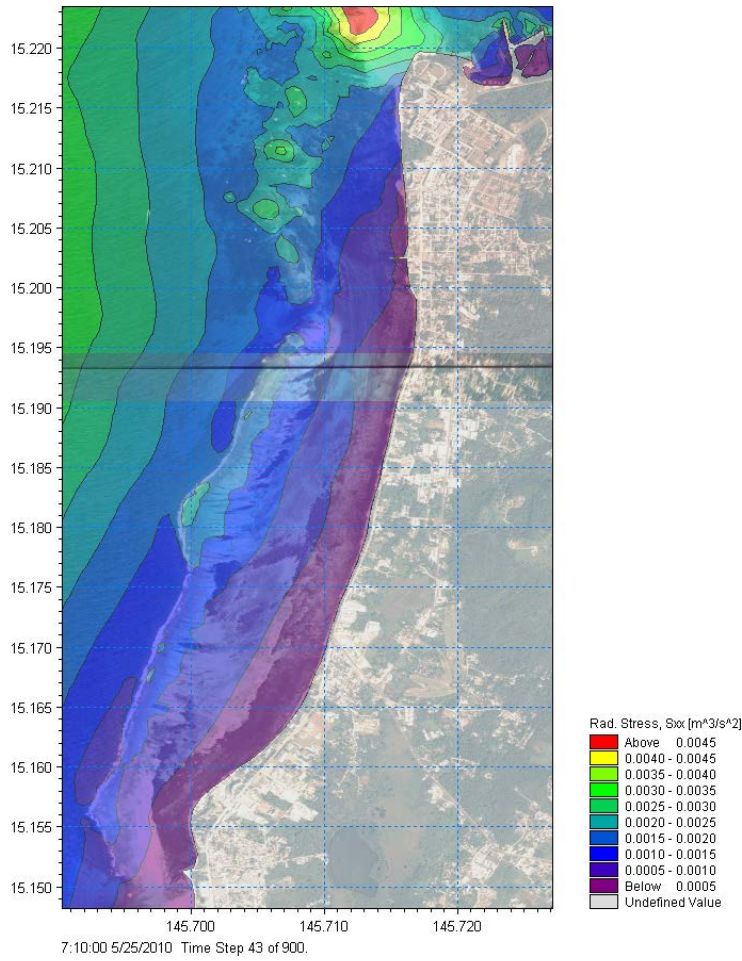


Figure 38. Snapshot of wave model output showing eastward radiation stress (S_{xx}) for Season 2. Backdrop is a 2005 Quickbird satellite image (source: CRMO).

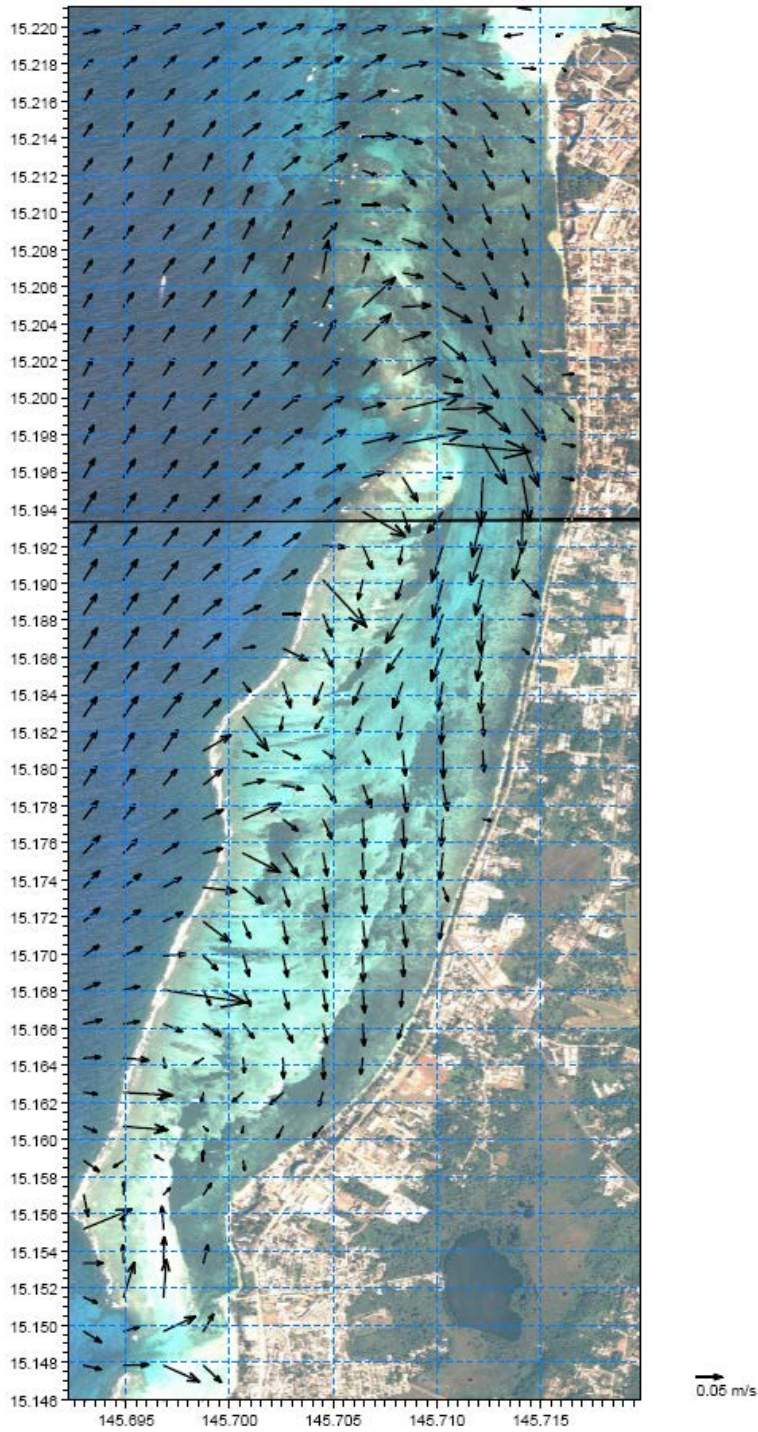


Figure 39. Snapshot of the dominant near bed current pattern in Garapan lagoon during Scenario 2 showing a predominantly inward and southward water flow. Backdrop is a 2005 Quickbird satellite image (source: CRMO).

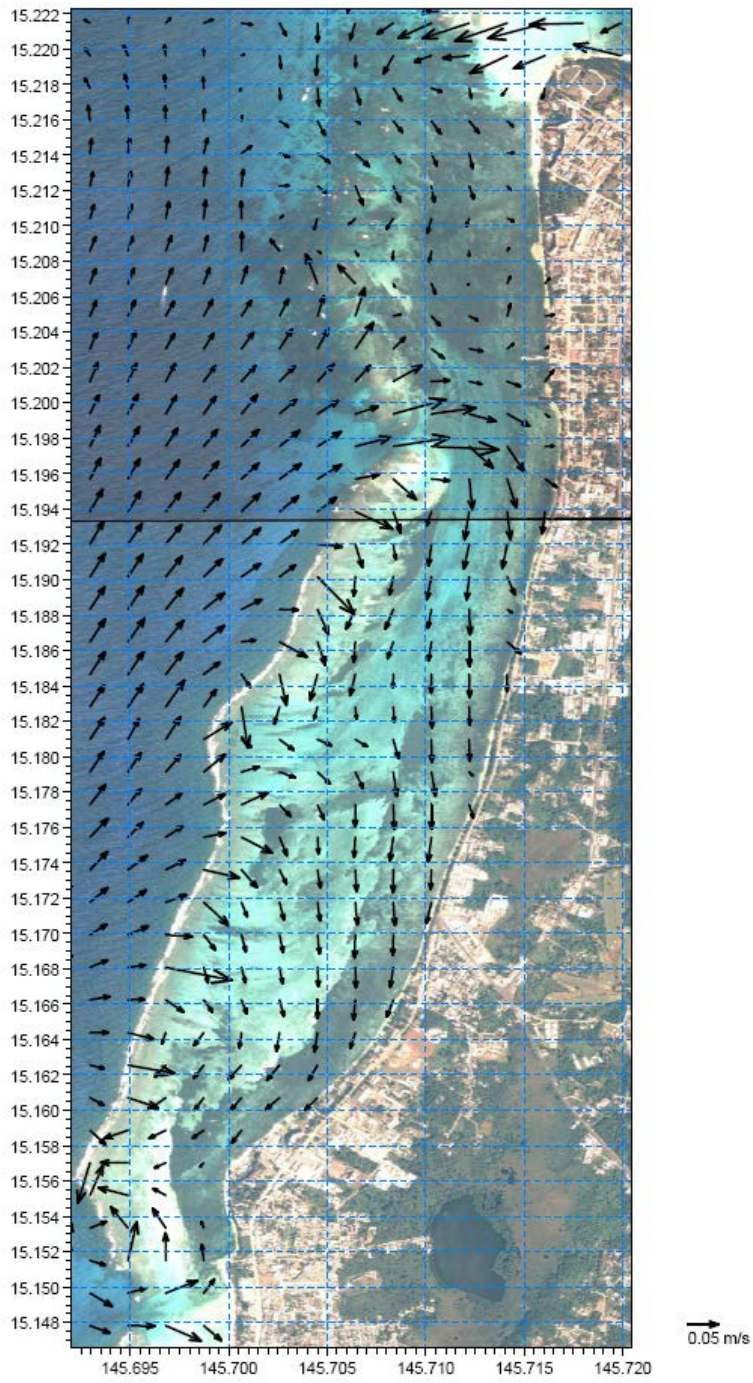


Figure 40. Near bed current patterns during Season 2 showing the influence of the dominant discharge through the shipping channel during high tide on water circulation between Puntan Muchot and Garapan pier. Backdrop is a 2005 Quickbird satellite image (source: CRMO).

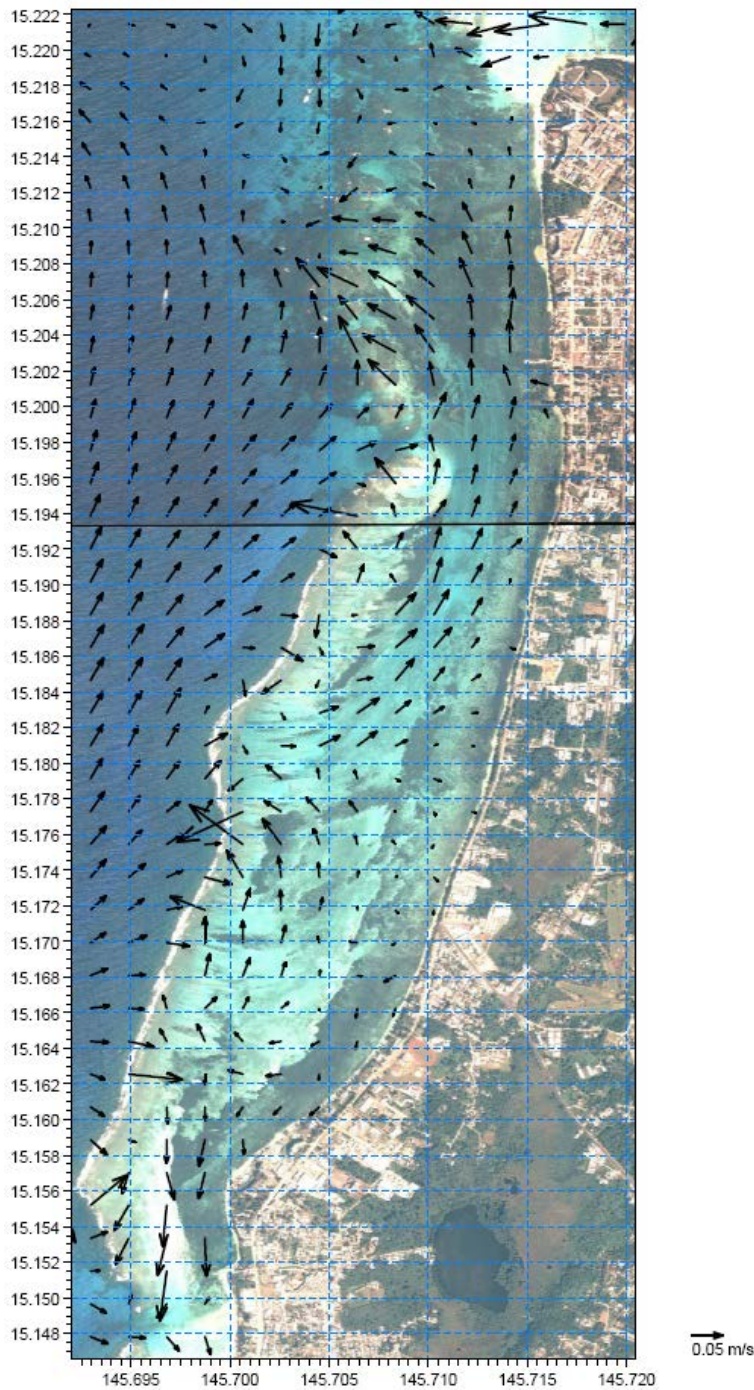


Figure 41. Near bed current patterns at low tide for Scenario 2. Dominant flow is toward the north due to a surface elevation gradient from the lagoon (higher water level) to the ocean (lower water level). Backdrop is a 2005 Quickbird satellite image (source: CRMO).

Due to the shallow nature of Garapan lagoon, wind stress is presumed to play an important role in the velocity patterns of the surface layer. While both channels within Garapan Lagoon (Garapan pier channel and Sugar Dock channel) exhibit a permanent influx of water in the near bed layer, outward flushing occurs in the surface layer. An example of this is shown in Figure 42, which compares current direction in the Garapan Dock channel between the near-bed and surface layer. The data show that an outward flux occurs in the surface layer at spring low tide, due to the influence of the wind stress.

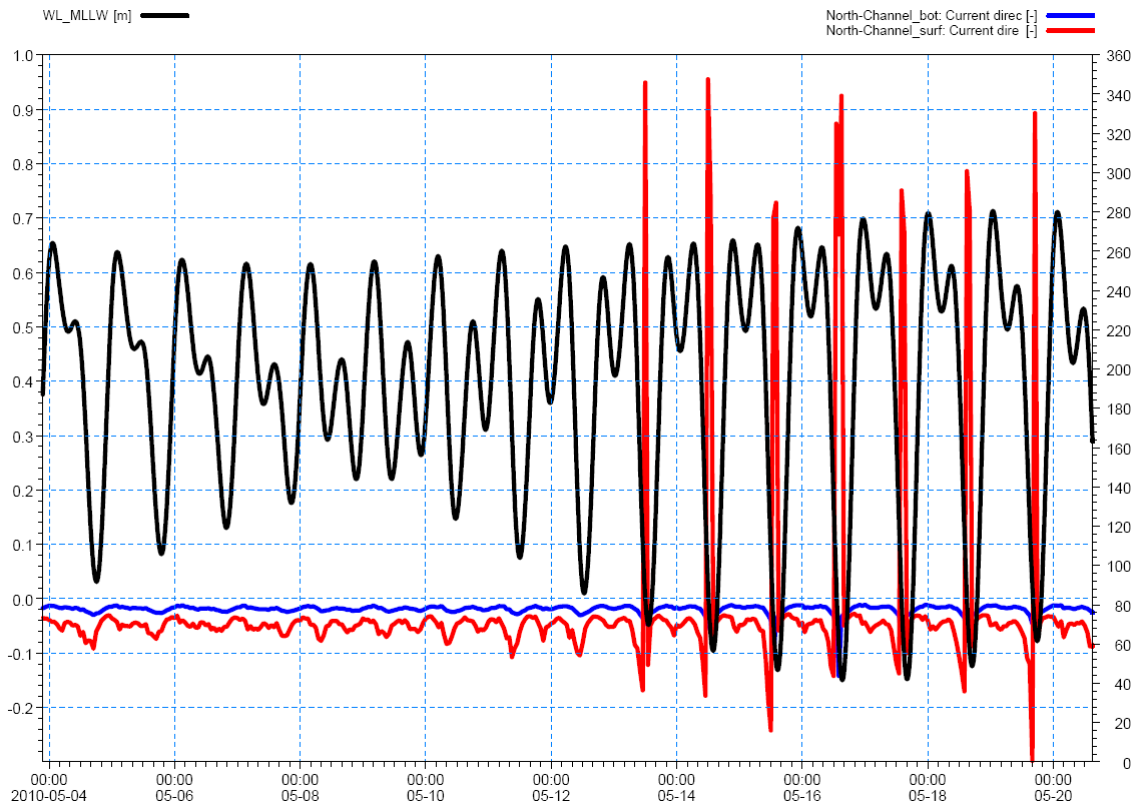


Figure 42. Comparative time series of observed surface elevation for Scenario 2 at the tide gauge (black line using the left y-axis), and current direction extracted from the model in the Garapan Dock channel for the surface layer (red) and near bed layer (blue), using the right y-axis.

A more pronounced difference between the near-bed and surface layer is evident in the Sugar Dock channel as shown in Figure 43. In this channel the near-bed current is always directed at 90°, or into the lagoon, whilst the surface layer shows a reverse direction during the ebbing tide. This is interpreted as a contribution of wind stress on the surface layer, which is aligned in direction with the ebbing current for approximately four to five hours a day.

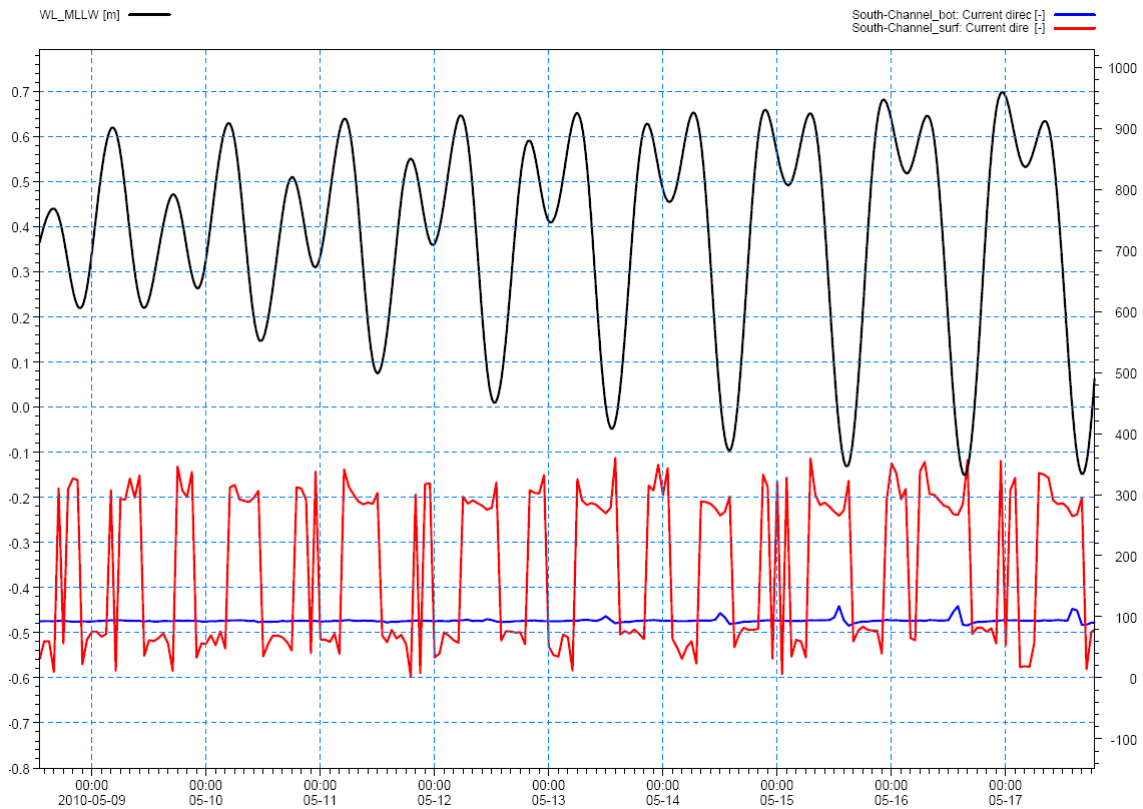


Figure 43. Comparative time series of observed surface elevation for Scenario 2 at the tide gauge (black line using the left y-axis), and current direction extracted from the model in the Sugar Dock channel for the surface layer (red) and near bed layer (blue), using the right y-axis.

4.1.3 Chalan Kanoa Lagoon

Chalan Kanoa lagoon is located between the Sugar Dock channel at Susupe and Agingan point in the south (Figure 44). This is a small and shallow lagoon with an area of less than 2 km² and an averaged depth of approximately 1 m. The lagoon is bound on the seaward side by a continuous coral reef and is therefore subject to wave-induced currents through the influence of radiation stress from wave breaking (Figure 45), as well as water flow through the Sugar Dock channel (Figure 46).

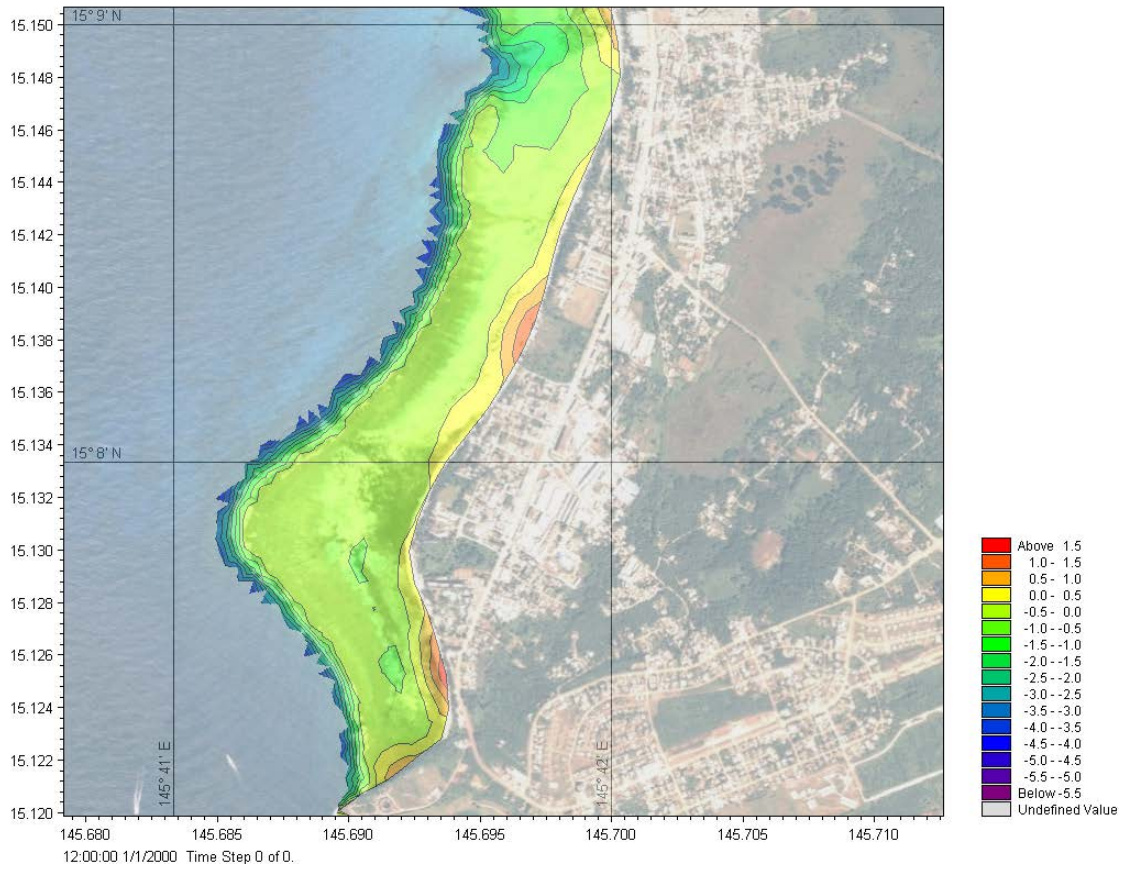


Figure 44. Bathymetry of Chalan Kanoa Lagoon. Water depths are red to blue, shallow to deep. Backdrop image is a 2005 Quickbird satellite image (source: CRMO).

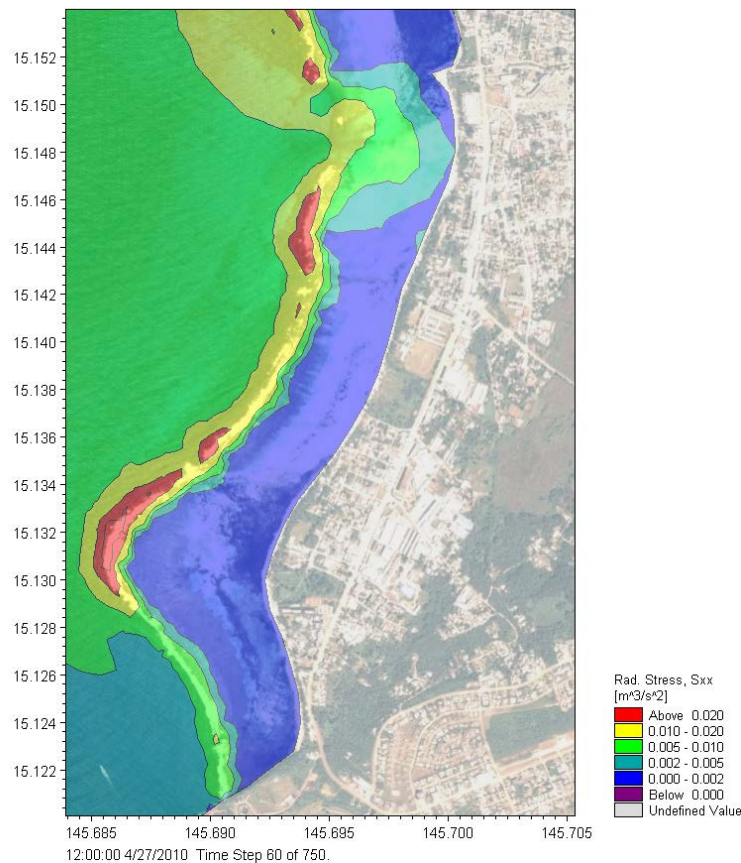


Figure 45. Snapshot of wave model output showing eastward component of wave-induced radiation stress (S_{xx}) for Scenario 1. Backdrop image is a 2005 Quickbird satellite image (source: CRMO).

Two main water circulation patterns are evident for the Chalan Kanoa lagoon from the 3D wave-current hydrodynamic model as per Scenario 1. As discussed previously, the hydrodynamics of Garapan and Chalan Kanoa lagoons are strongly interconnected, and most of the water passing through Garapan lagoon enters Chalan Kanoa lagoon due to the dominant southward current. Water is then mainly flushed out across the reef segment adjacent to Agingan point (Figure 46), where wave setup is the lowest as inferred from the map of radiation stress shown in Figure 45.

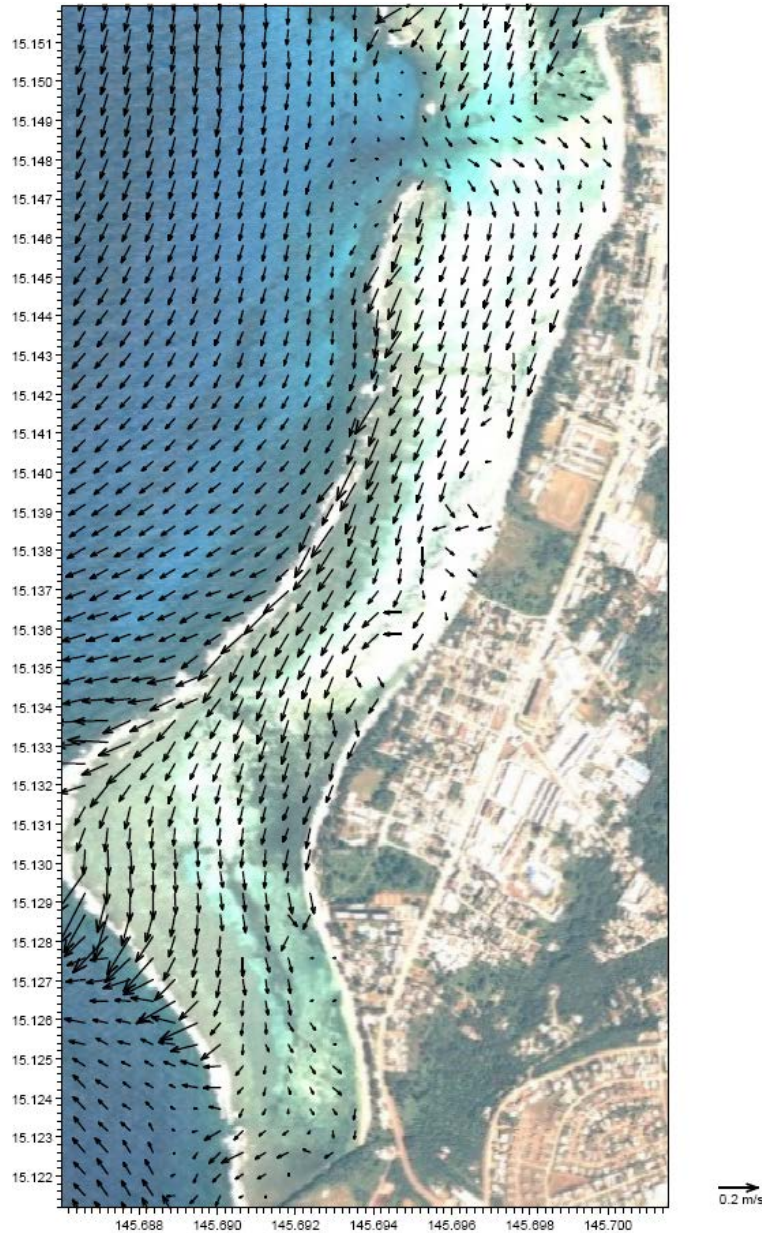


Figure 46. Snapshot of dominant near bed current pattern in Chalan Kanoa Lagoon for Scenario 1, showing dominant southward flow. Backdrop image is a 2005 Quickbird satellite image (source: CRMO).

The current pattern at low tide is difficult to determine due to the shallow nature of the lagoon, with an apparent discharge of water at low tide water through the depression in the reef northwest of Afetna point (Figure 47). In the southern end of the lagoon, water circulation is reversed during low tide as water travels northward to exit the lagoon driven by a hydraulic gradient.

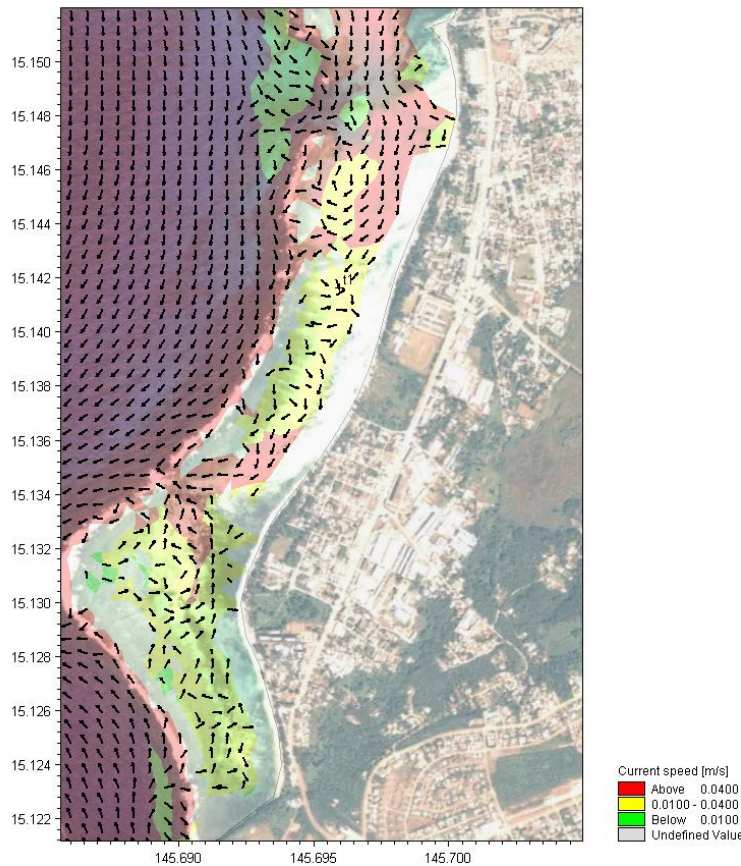


Figure 47. Snapshot of near bed current pattern during low tide in Chalán Kanoa Lagoon for Scenario 1, showing ocean ward flow through the reef at Afetna Point. Backdrop is a 2005 Quickbird satellite image (source: CRMO).

For Scenario 2, the current patterns for Chalán Kanoa lagoon are markedly different. During this period of the year, the southward current originating from Garapan lagoon in the north is significantly lower and cannot overcome the influx of oceanic waters through the Sugar Dock channel (Figure 48). As a result, water exchange between Garapan lagoon and Chalán Kanoa lagoon is null or insignificant. During this period the wave also refract around the south of Saipan and at high tide, wave setup along the reef segment between Agingan to Afetna points in the south of Chalán Kanoa lagoon induce a northward current. Figure 48 shows these two opposing currents converging at Point Afetna before draining out over the reef.

At low tide (Figure 49), the reef flat is under less than 20 cm of water and wave-induced currents are significantly reduced, and current speeds within the lagoon are generally less than 3 cm/s. A similar circulation than during low tide of season one occurs with outward flushing by hydraulic gradient forces through the reef depressions, e.g. in the reef just north of Afetna point. When wave pumping stops the water continues to drain through this depression by hydraulic gradient forces.

When water levels are low enough, south-easterly winds can increase the current speed in the south region and reverse the current in the northern region, from south to north-directed. In other words, the south-easterly wind stress reverses the current in the northern region, from southward to northward, increasing the northward current in the southern region.

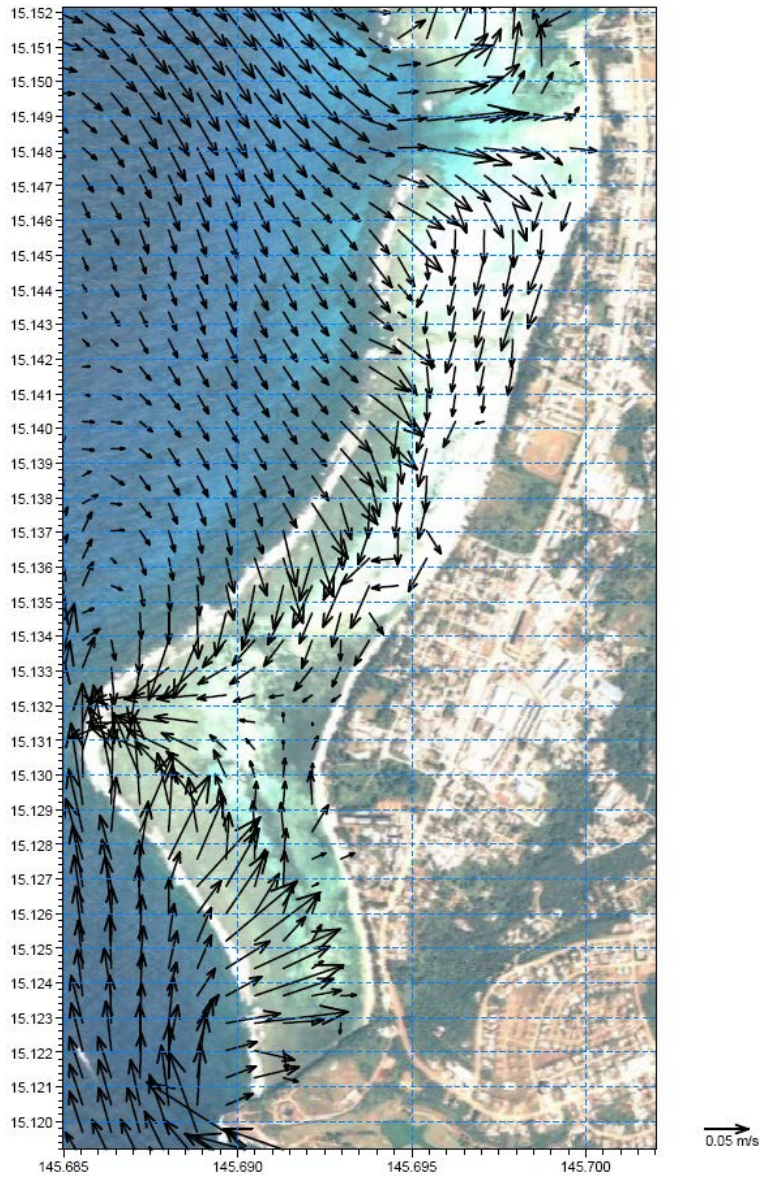


Figure 48. Snapshot of dominant near bed current pattern in Chalan Kanoa Lagoon for Scenario 2, showing wave-driven inward currents, converging at Puntan Afetna. Backdrop is a 2005 Quickbird satellite image (source: CRMO).

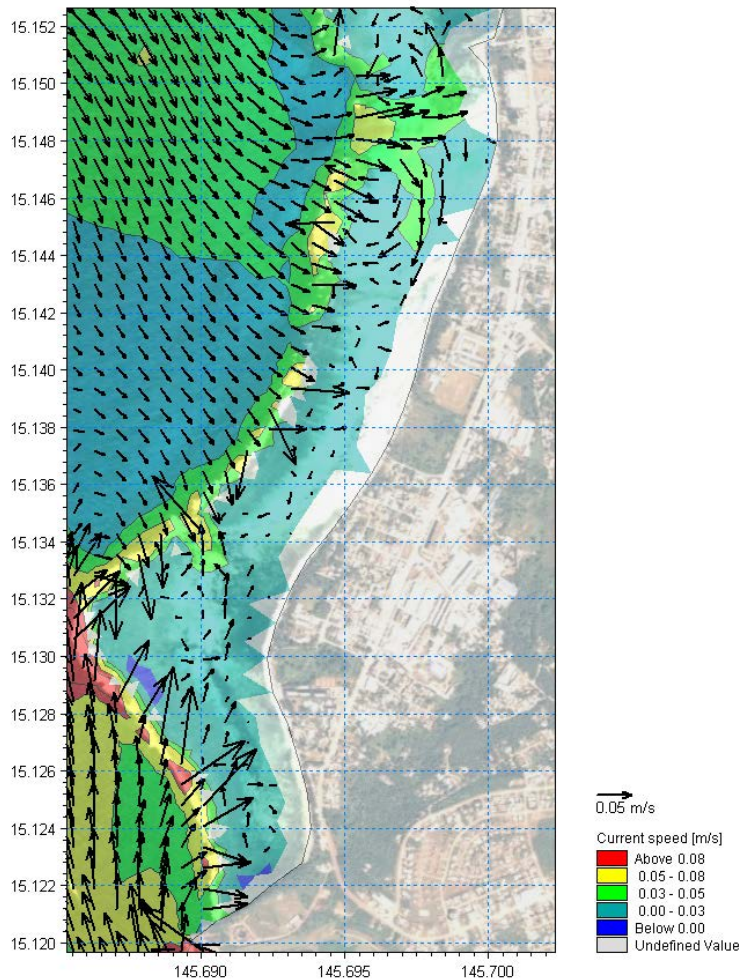


Figure 49. Snapshot of near bed current pattern at low tide in Chalan Kanoa Lagoon for Scenario 2, showing outward flow through the channel off Puntan Afetna. Backdrop is a 2005 Quickbird satellite image (source: CRMO).

4.2 Plume Dispersion

This section considers the plume in to be an imaginary substance with a concentration of 100 g/m^3 , as described in Section 3.2.4. The model was then used to investigate the diffusion of this plume in space and the variation of its concentration over time.

4.2.1 High Wave Energy Scenario 1

During the dominant wave-induced conditions of Scenario 1, the plume is driven south and into Garapan lagoon past Muchot point (Figure 50). The pollutant does not enter the Managaha marine conservation area (MCA). However, Figure 51 shows the plume being transported into Garapan lagoon with a concentration of less than 0.05% of the initial concentration. Moreover, Garapan and Chalan Kanoa lagoon are strongly connected during Scenario 1, and most of the plume that enters Garapan lagoon therefore also reaches Chalan Kanoa lagoon.

At low tide, when northern barrier reef in Tanapag lagoon dries up, lagoon-ward flow occurs through the channel which carries the plume in a northerly direction (Figure 52). This causes the introduction of a pulse of pollutants into the Tanapag lagoon proper once per tidal cycle. When wave pumping occurs again, this sub-plume is driven south again, but through the eastern margin of MCA. This shows that the plume can impact on parts of the MCA before being flushed out through the channel. The daily pollutant concentration

entering MCA does not exceed 0.15% of the initial pollutant concentration of 100%. Additionally, since the path leading the plume to enter the MCA is driven by the channel lagoon-ward flow, the greater the tidal amplitude the larger is the detached plume. After exiting the channel, the sub-plume continues south along the outside of the reef as shown in Figure 53. At this time, the main plume is again aligned with the wind-induced southward directed flow as per Figure 50 and Figure 51.

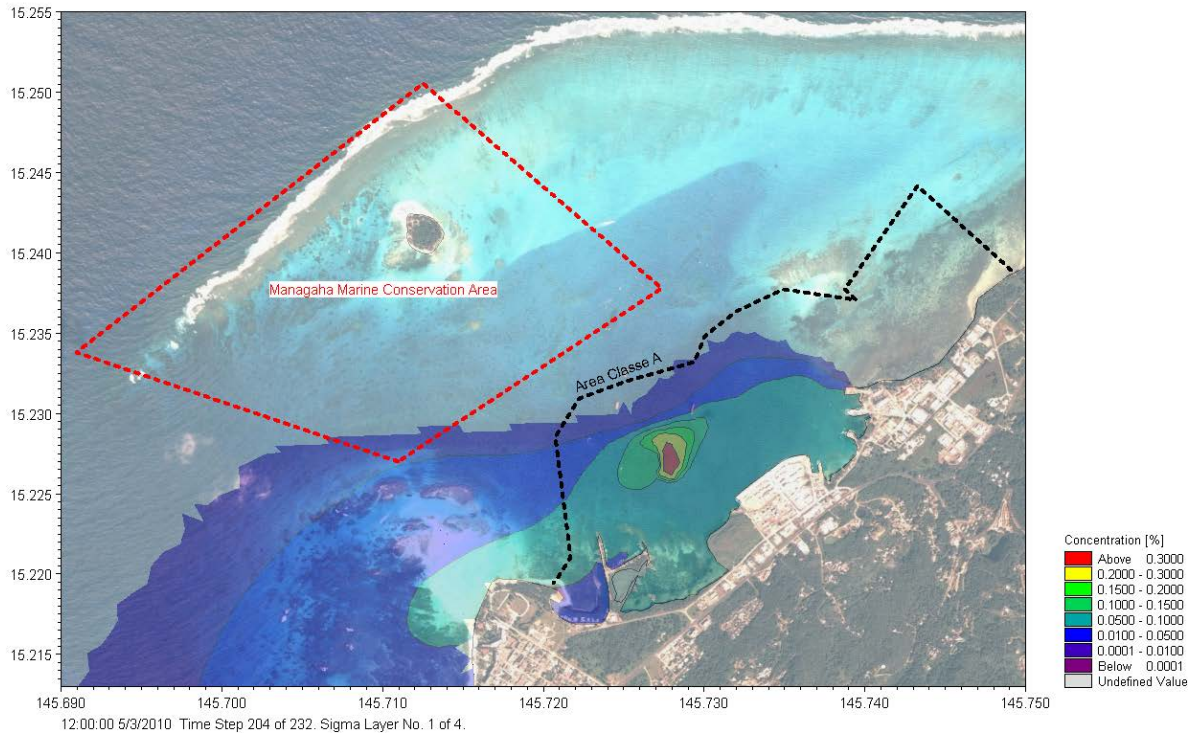


Figure 50. Snapshot of plume in Tanapag lagoon during Scenario 1, using an initial source concentration of 100%. Backdrop is a 2005 Quickbird image (source: CRMO).

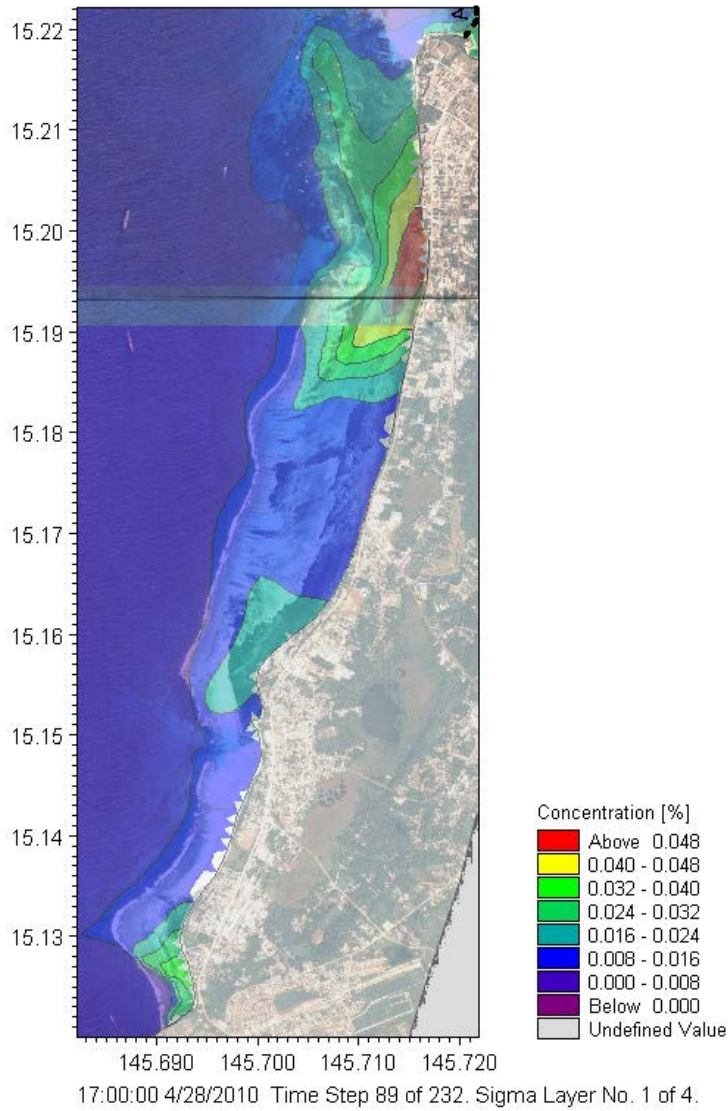


Figure 51. Snapshot of plume in the southern Saipan lagoon (Garapan and Chalan Kanoa lagoons) during Scenario 1, using an initial source concentration of 100%. Backdrop is a 2005 Quickbird image (source: CRMO).

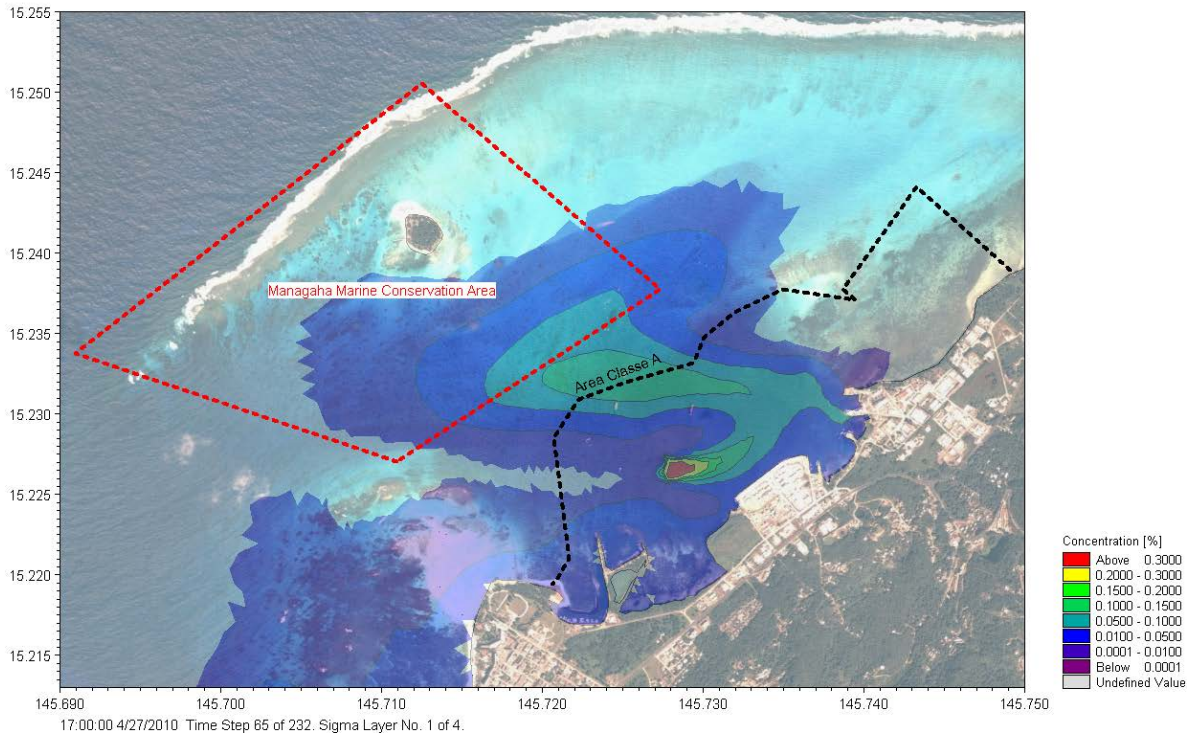


Figure 52. Snapshot of plume in Tanapag lagoon during Scenario 1 using an initial source concentration of 100%. Only concentrations >0.0001% are shown. Backdrop is a 2005 Quickbird image (source: CRMO).

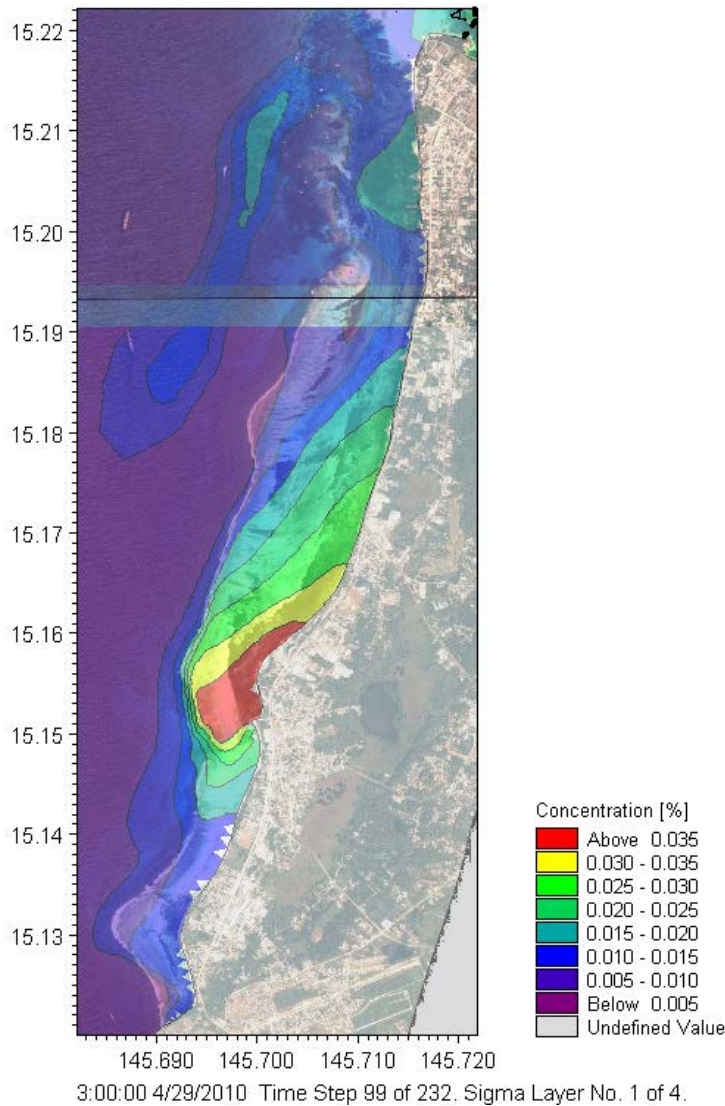


Figure 53. Snapshot of plume in the south of Saipan lagoon (Garapan and Chalan Kanoa lagoons) during Scenario 1, using an initial source concentration of 100%. Note the sub-plume on the outside of the reef that was previously detached from the main plume and flushed out through the channel after transiting through the Managaha Conservation Area. Backdrop is a 2005 Quickbird image (source: CRMO).

4.2.2 Low Wave Energy Scenario 2

Scenario 2 is characterised by an influx of oceanic waters through the channel, rather than over the reef crest as during Scenario 1. This causes the plume to be more widely dispersed within Tanapag lagoon, including significant transport toward the north of the lagoon. The model shows the plume to permanently impact on the MCA with <0.35% of the initial concentration as shown in Figure 54.

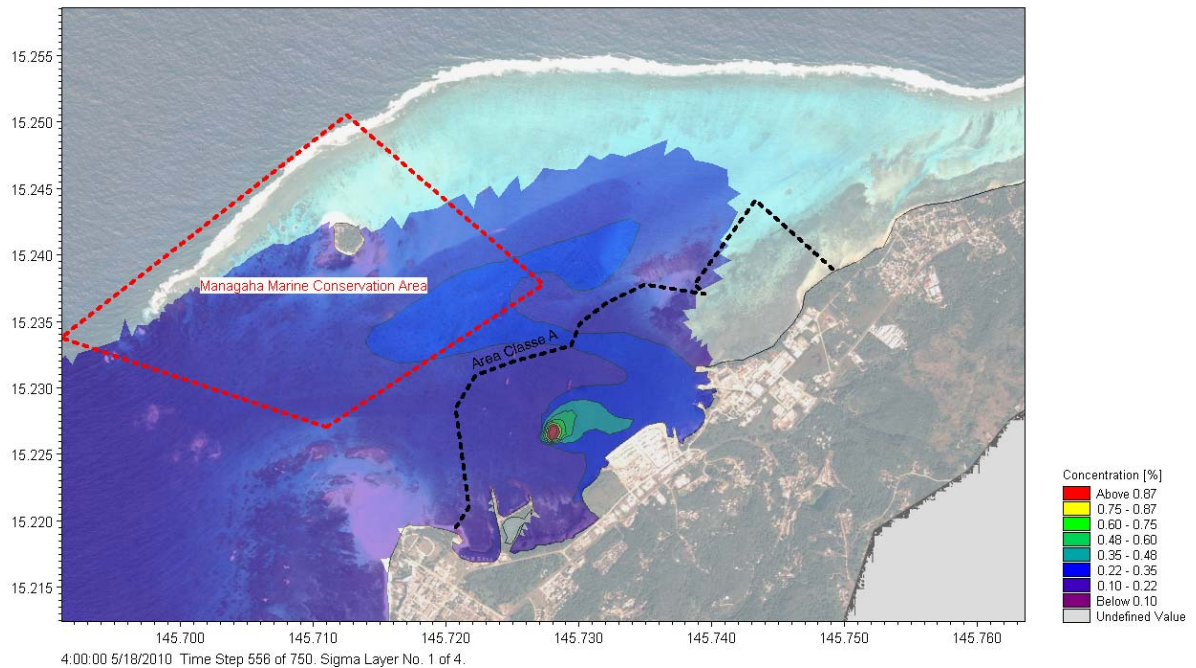


Figure 54. Snapshot of plume in Tanapag lagoon during Scenario 2, using an initial source concentration of 100%. Backdrop is a 2005 Quickbird image (source: CRMO).

Following the dominant water circulation during Scenario 2, the Sadog Tasi plume is more likely to drift westward of Tanapag lagoon, staying north of latitude 15.20° (Figure 55). Additionally, the fraction of the plume that enters Garapan lagoon via Puntan Muchot has a very low concentration of ($<5.0 \times 10^{-4}\%$ of the initial pollutant concentration). Figure 55 shows this plume to reach as far south as Susupe point, before being flushed out through the Sugar dock channel. As discussed previously, water exchange between Garapan lagoon and Chalan Kanoa lagoon is insignificant during Scenario 2, which leads the southern-most part of Saipan lagoon to remain pollutant free ($<1.0 \times 10^{-6}\%$) and unaffected by the discharge from the Sadog Tasi outfall during this time of the year (April to September).

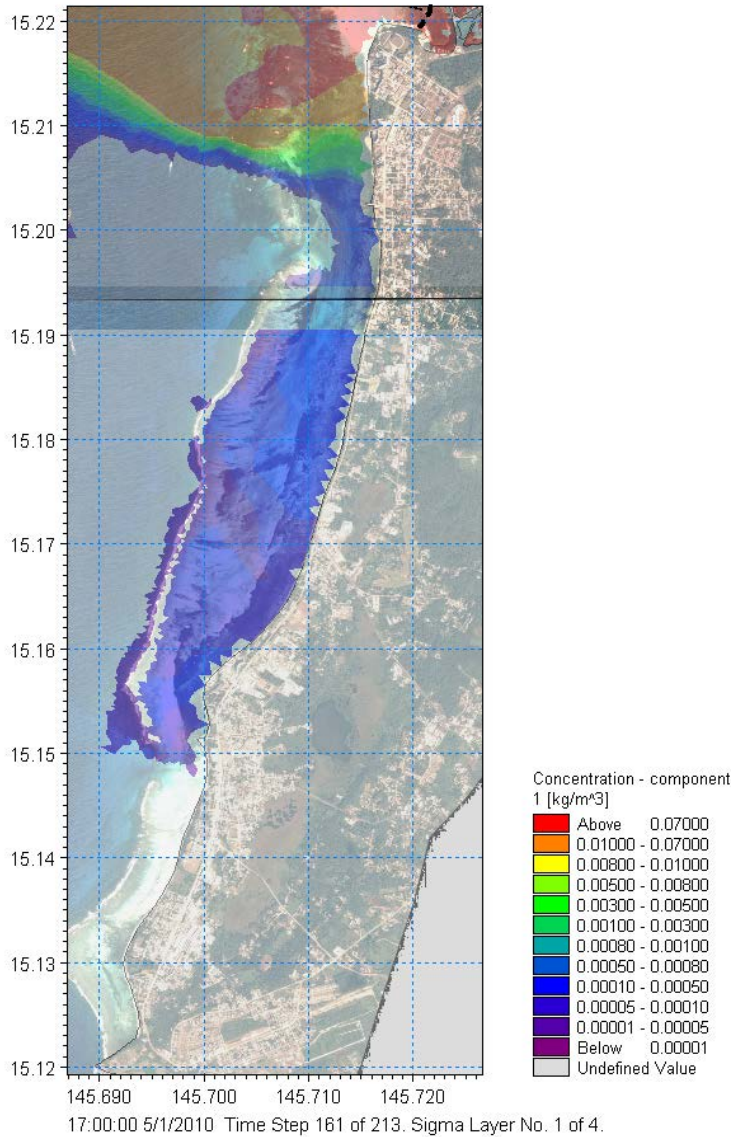


Figure 55. Snapshot of plume in the southern Saipan lagoon (Garapan and Chalan Kanoa lagoons) during Scenario 2, using an initial source concentration of 100%. Backdrop is a 2005 Quickbird image (source: CRMO).

4.3 Component Plume Dispersion

This section details the transport of constituents within the plume using a monthly averaged discharge and maximum daily discharge. The transport of a specific pollutant depends on its initial concentration as the diffusion term varies throughout the domain and with time. While the transport of a particular pollutant follows the same path for each constituent as governed by the hydrodynamics, the distribution throughout the plume is concentration specific. The transport and dispersion of nine main constituents (Nitrate, Total Nitrogen, Orthophosphate, Total Phosphorous, Unionized Ammonia, Copper, Nickel, Zink, TRC) was therefore investigated in more detail. The concentration of the constituents is then discussed according with reference to the Commonwealth of the northern Marina Islands water quality standards (*CNMIWQS*). See figure captions for details.

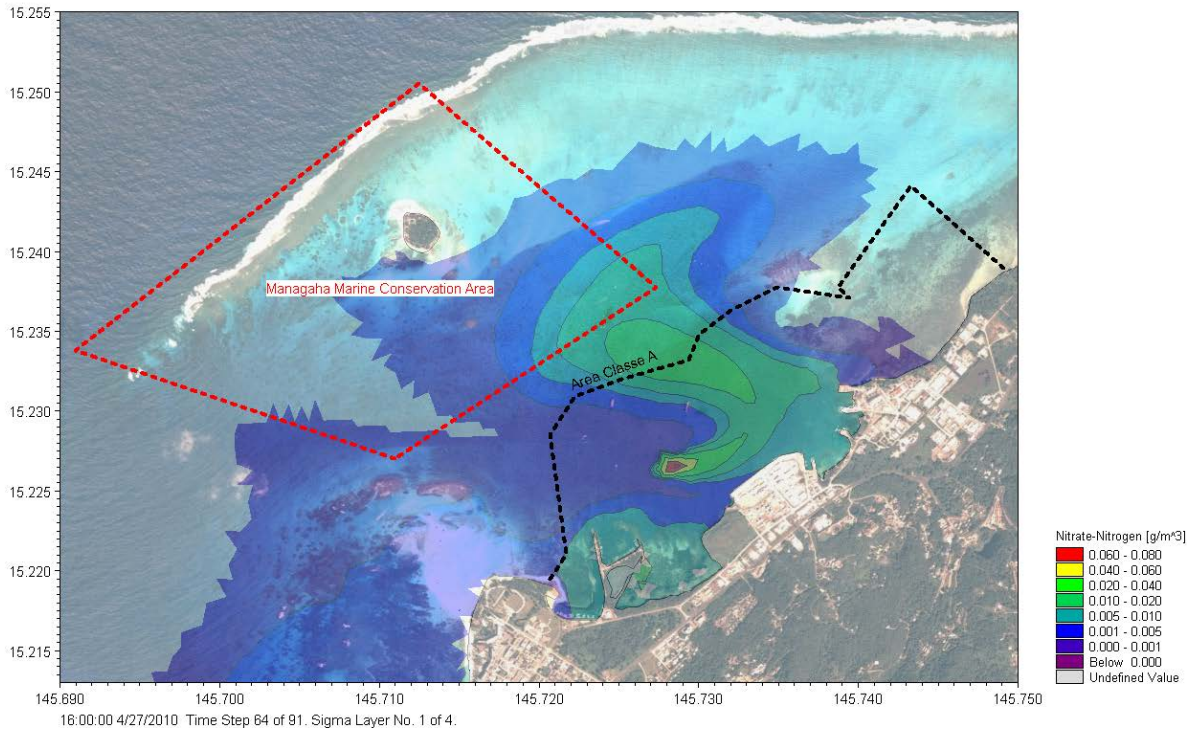


Figure 56. Snapshot of plume of Nitrate under Scenario 1. With a maximum monthly discharge of 19 g/m³ of nitrate, its concentration in the lagoon is well below the limit of 0.2g/m³, given by the CNMIWQS for water of Class AA.

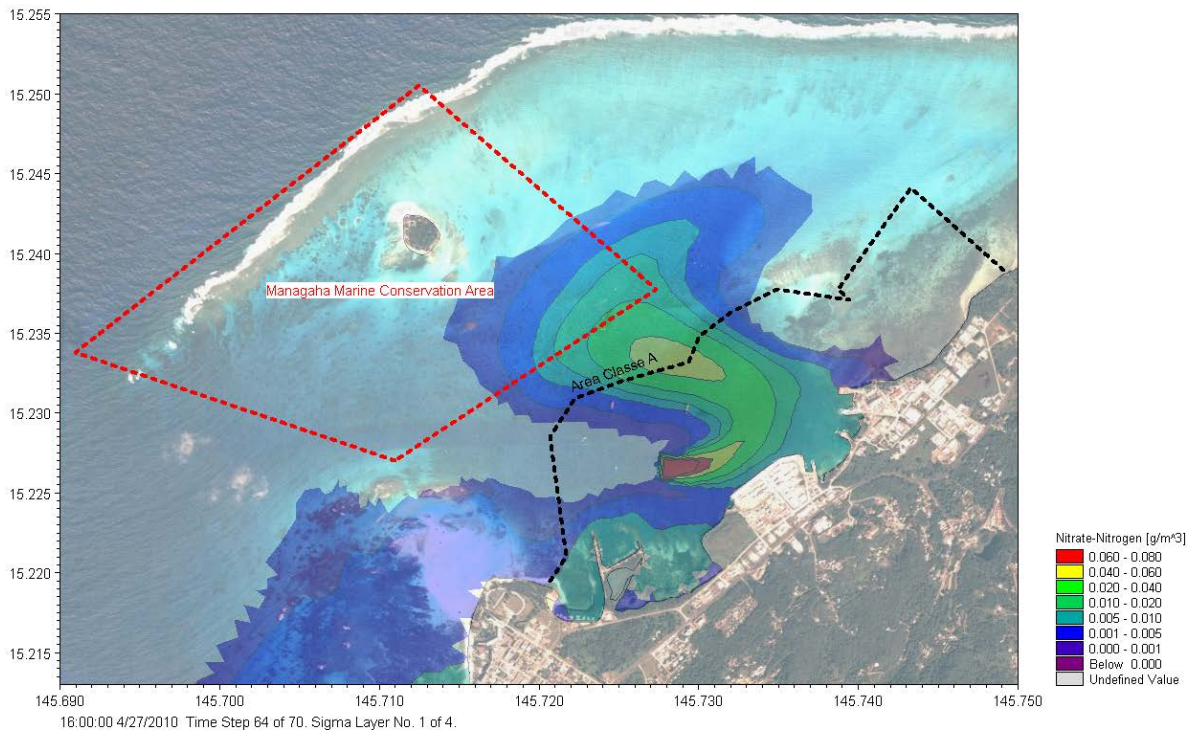


Figure 57. Snapshot of plume of Nitrate under Scenario 1. With a maximum daily discharge of 39 g/m³ of nitrate, its concentration in the lagoon is well below the limit of 0.2g/m³, given by the CNMIWQS for water of Class AA.

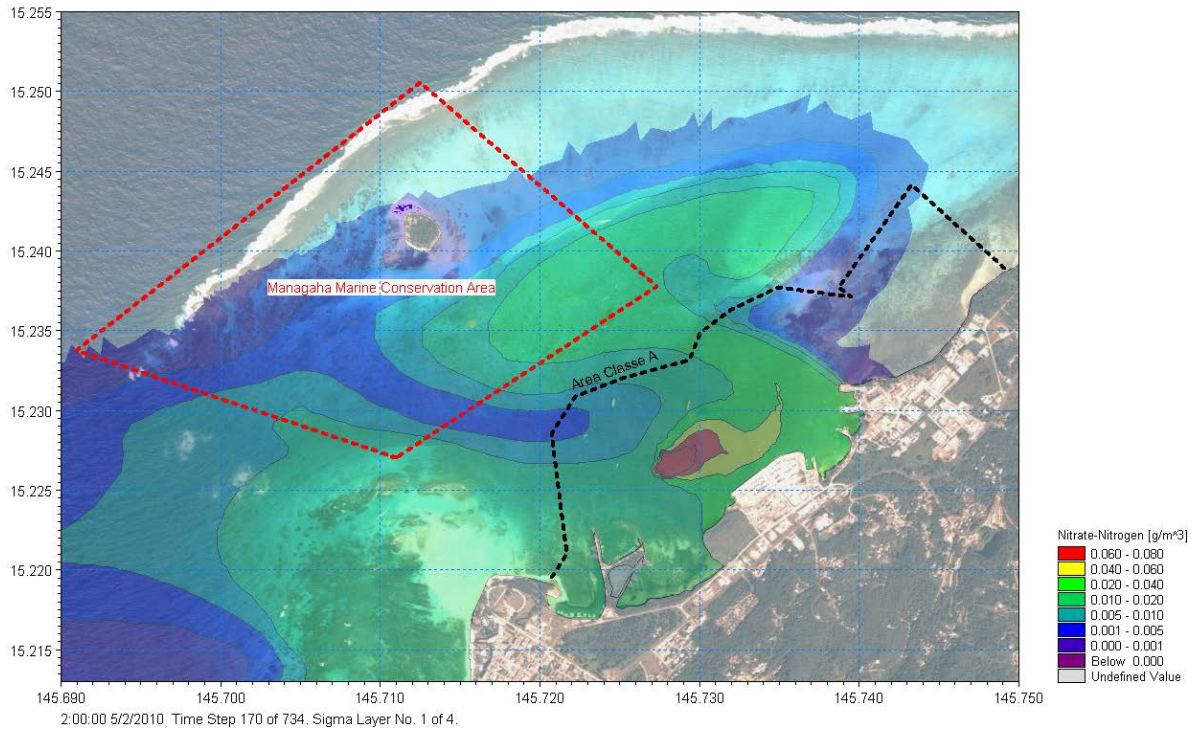


Figure 58. Snapshot of plume of Nitrate under Scenario 2. With a maximum monthly discharge of 19 g/m³ of nitrate, concentration in the lagoon will only exceed 0.2g/m³ away from the outfall.

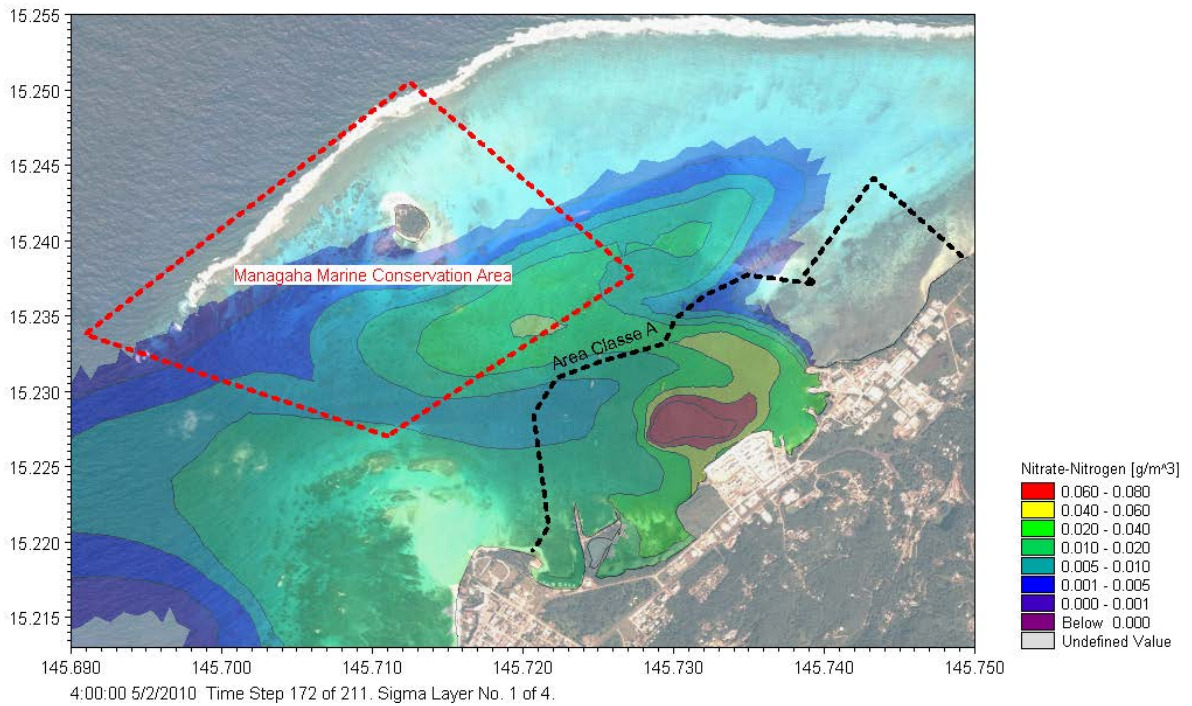


Figure 59. Snapshot of plume of Nitrate under Scenario 2. With a maximum daily discharge of 39 g/m³ of nitrate, concentration in the lagoon does not exceed 0.2g/m³.

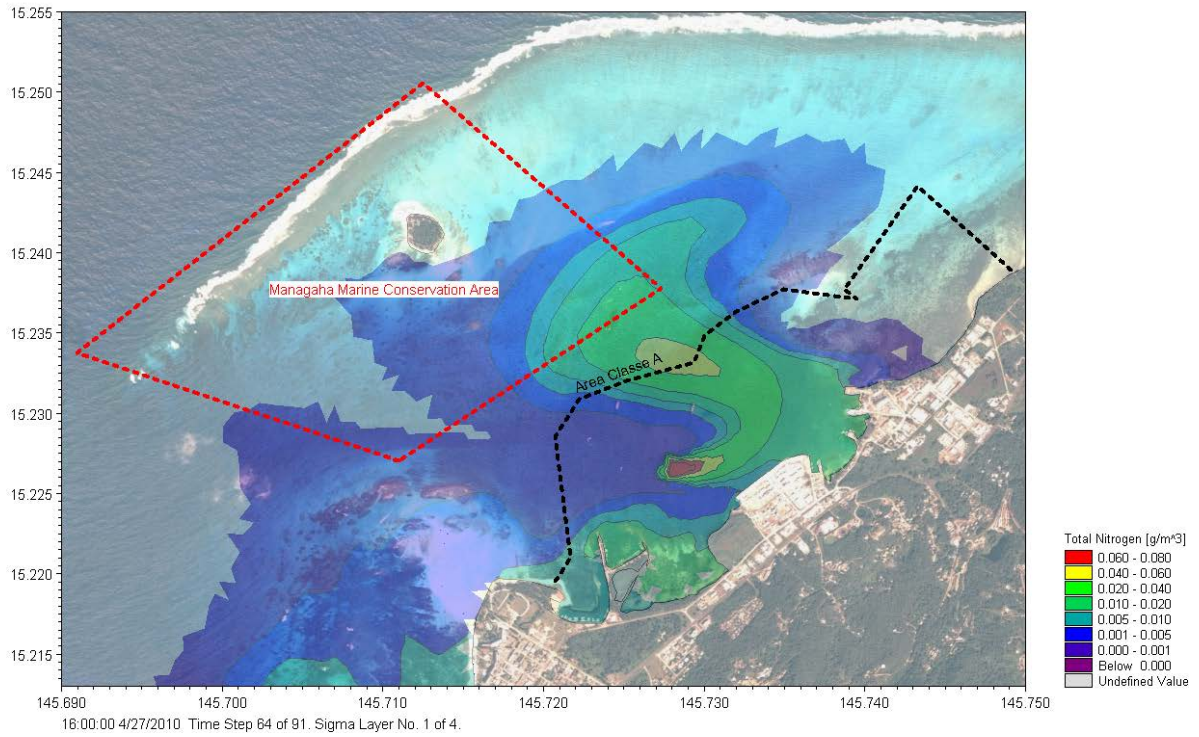


Figure 60. Snapshot of plume of Total Nitrogen under Scenario 1. With a maximum monthly discharge of 29 g/m³ of total nitrogen, its concentration is well below the limit of 0.4g/m³ in water of Class AA given by the CNMIWQS. In water of class A, the limit of 0.75g/m³ is not exceeded.

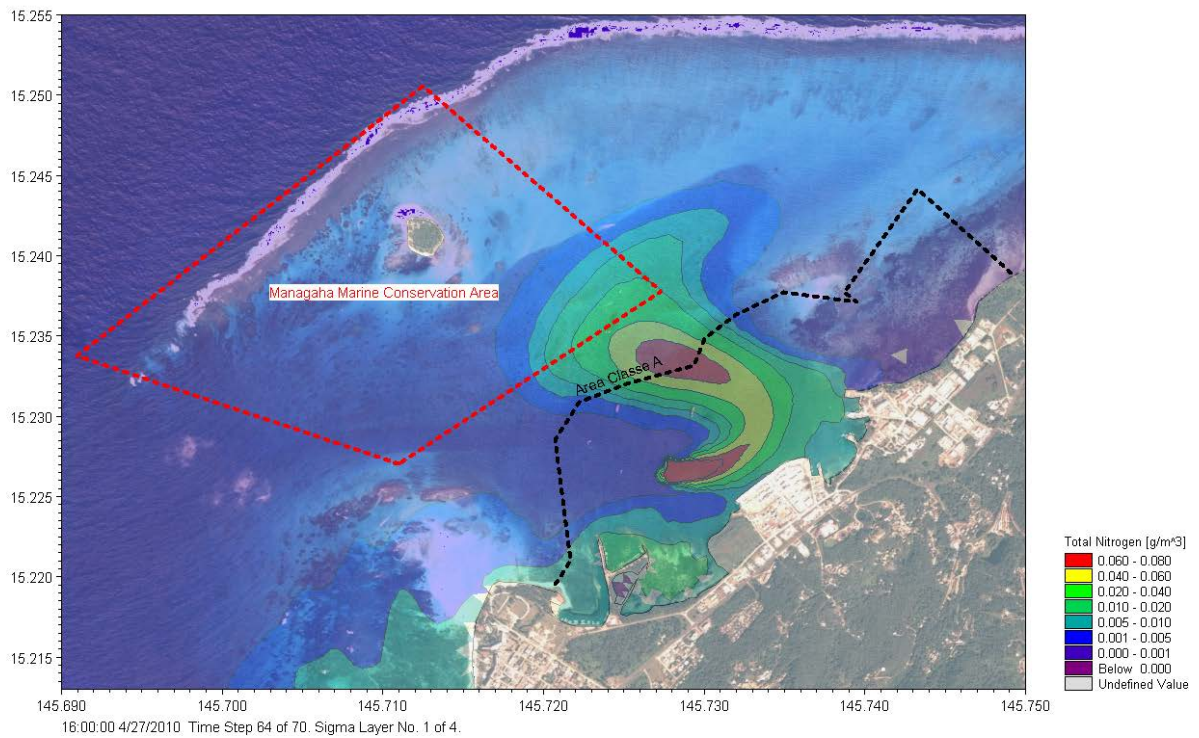


Figure 61. Snapshot of plume of Total Nitrogen under Scenario 1. With a maximum daily discharge of 58 g/m³ of total nitrogen, its concentration is well below the limit of 0.4g/m³ in water of Class AA given by the CNMIWQS. In water of class A, the limit of 0.75g/m³ is not exceeded.

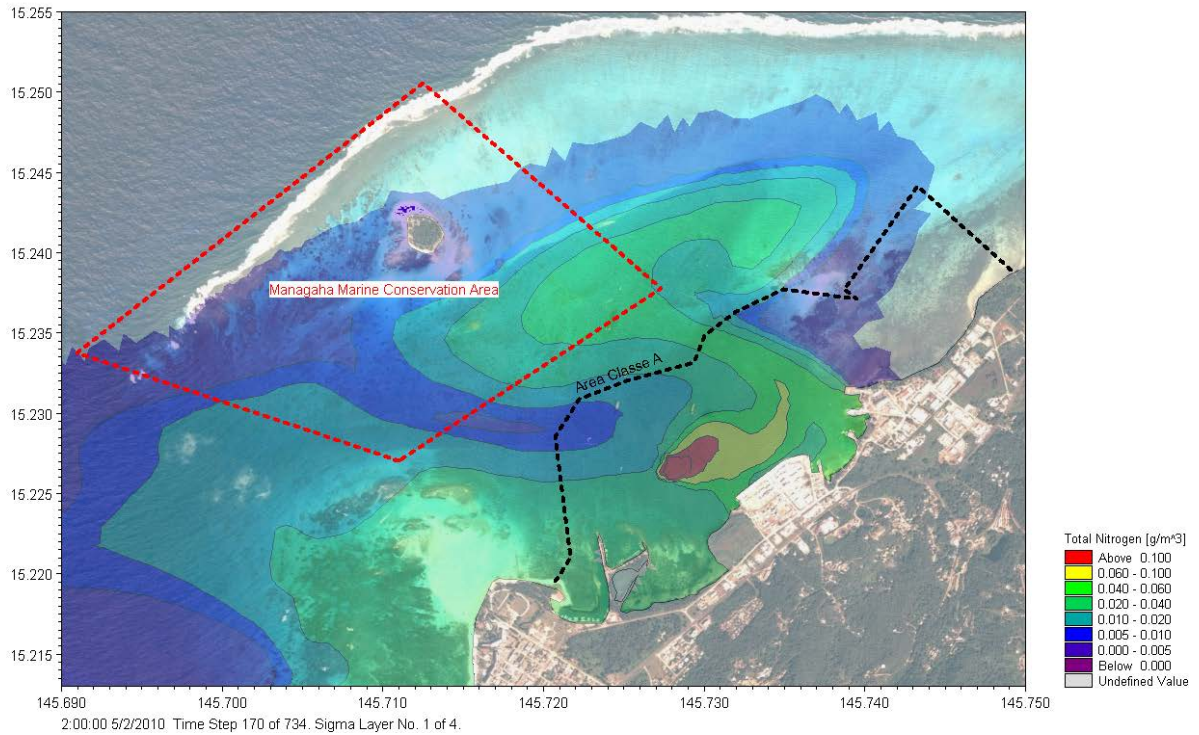


Figure 62. Snapshot of plume of Total Nitrogen under Scenario 2. With a maximum monthly discharge of 29 g/m³ of total nitrogen, its concentration is well below the limit of 0.4g/m³ in water of Class AA given by the CNMIWQS. In water of class A, the limit of 0.75g/m³ is not exceeded.

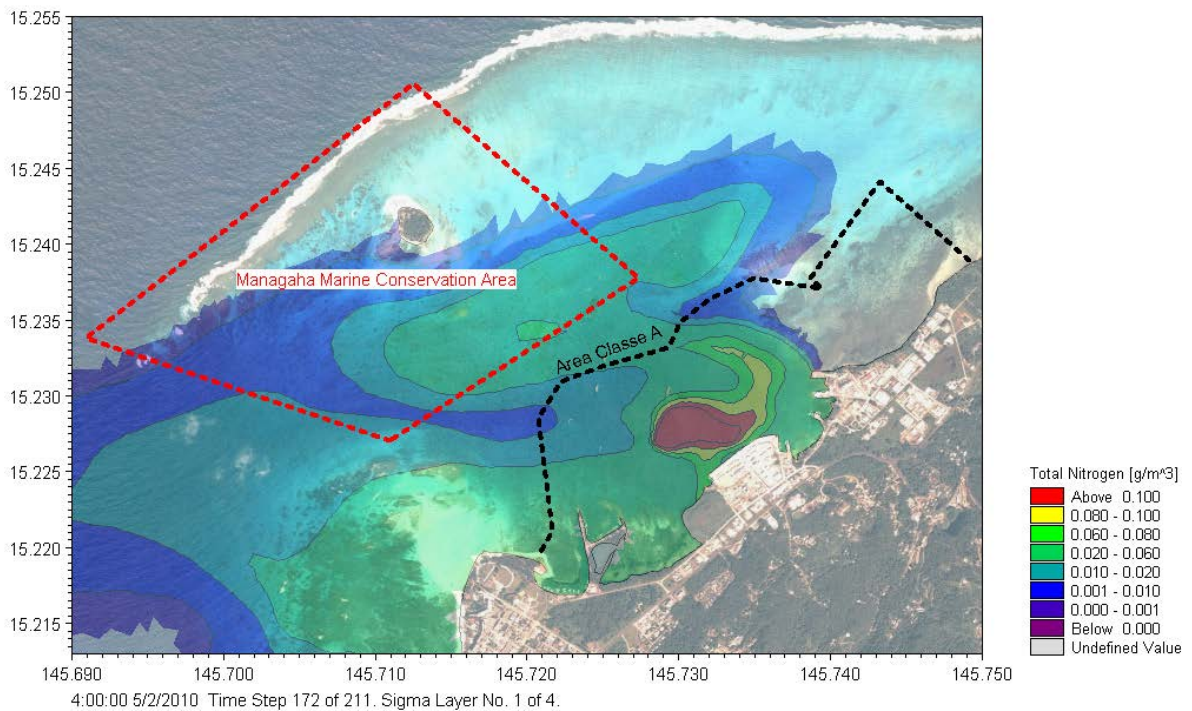


Figure 63. Snapshot of plume of Total Nitrogen under Scenario 2. With a maximum daily discharge of 29 g/m³ of total nitrogen, its concentration is well below the limit of 0.4g/m³ in water of Class AA given by the CNMIWQS. In water of class A, the limit of 0.75g/m³ is not exceeded.

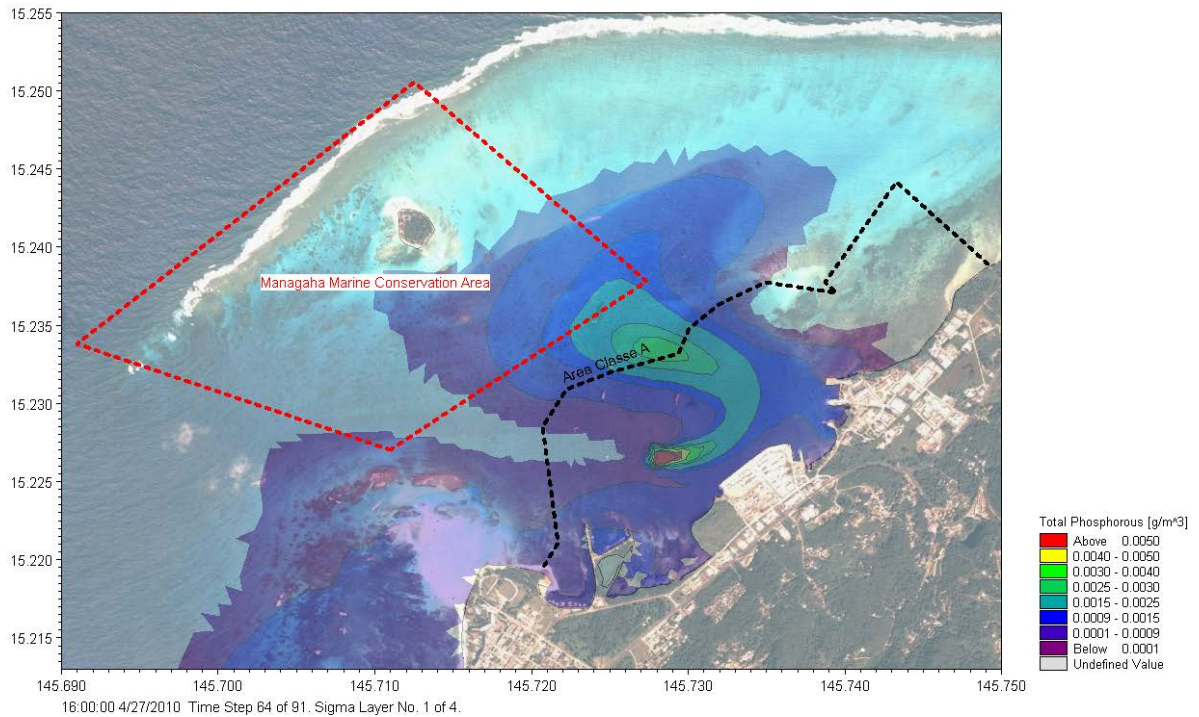


Figure 64. Snapshot of plume of Orthophosphate and Total Phosphorus under Scenario 1. With a maximum monthly discharge of 2g/m³ of Total Phosphorous and Orthophosphate, their concentration in the Class AA and Class A waters are well below their respective limits of 0.025g/m³ and 0.05g/m³.

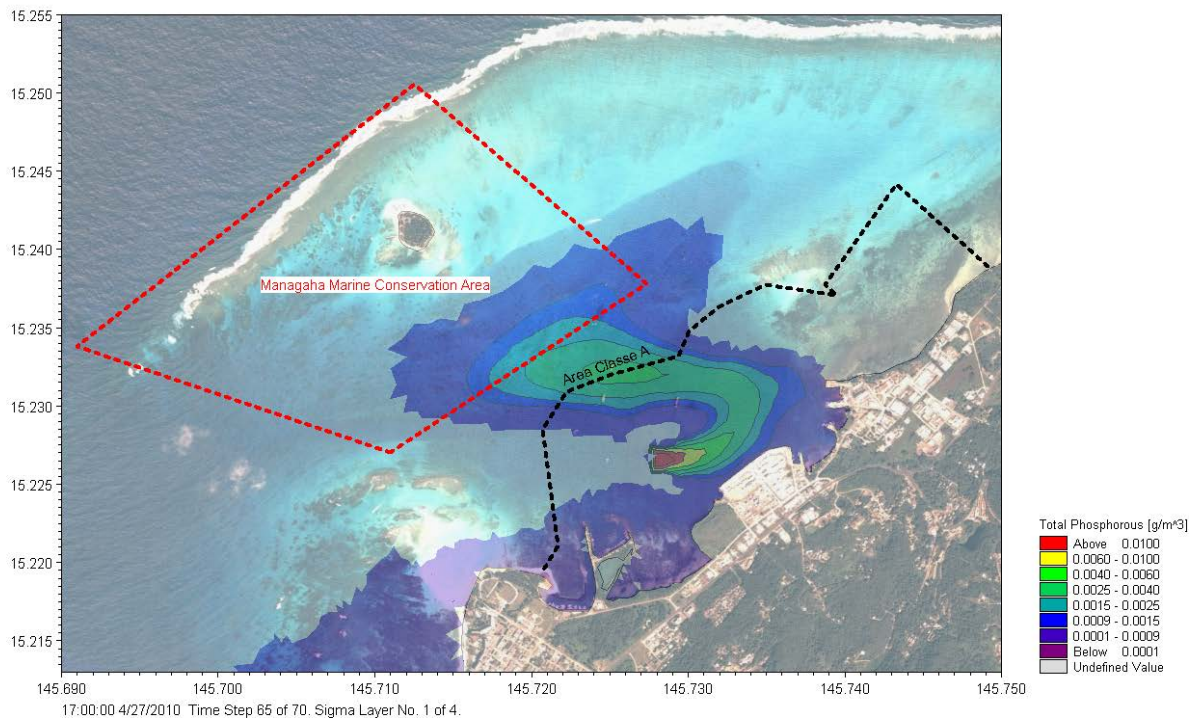


Figure 65. Snapshot of plume of Orthophosphate and Total Phosphorus under Scenario 1. With a maximum daily discharge of 4g/m³ of Total Phosphorous and Orthophosphate, their concentration in the Class AA and Class A waters are well below their respective limits of 0.025g/m³ and 0.05g/m³.

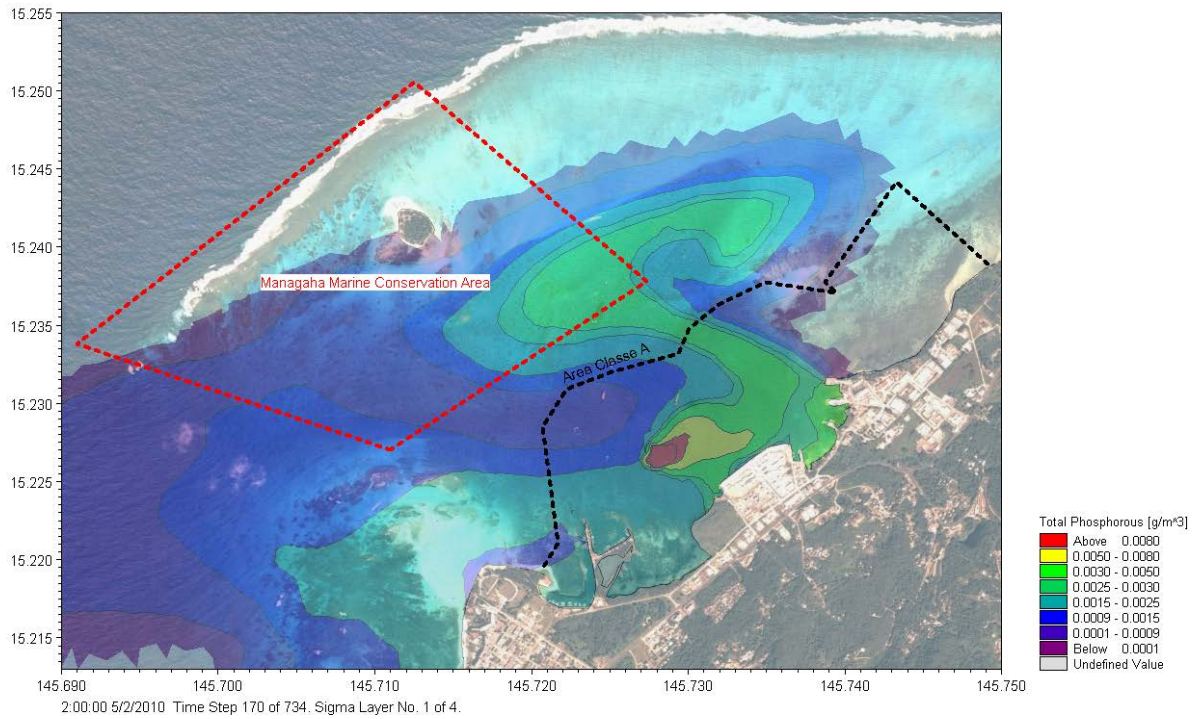


Figure 66. Snapshot of plume of Orthophosphate and Total Phosphorus under Scenario 2. With a maximum monthly discharge of 2g/m³ of Total Phosphorous and Orthophosphate, their concentration in the Class AA and Class A waters are well below their respective limits of 0.025g/m³ and 0.05g/m³.

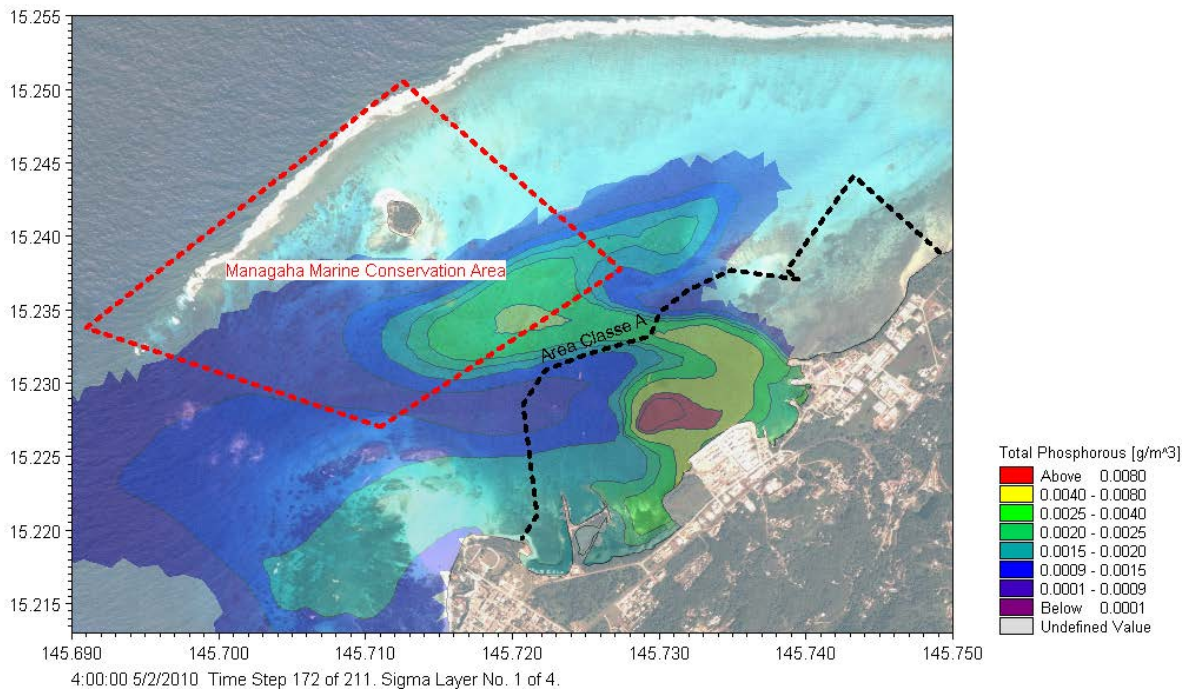


Figure 67. Snapshot of plume of Orthophosphate and Total Phosphorus under Scenario 2. With a maximum daily discharge of 4g/m³ of Total Phosphorous and Orthophosphate, their concentration in the Class AA and Class A waters are well below their respective limits of 0.025g/m³ and 0.05g/m³.

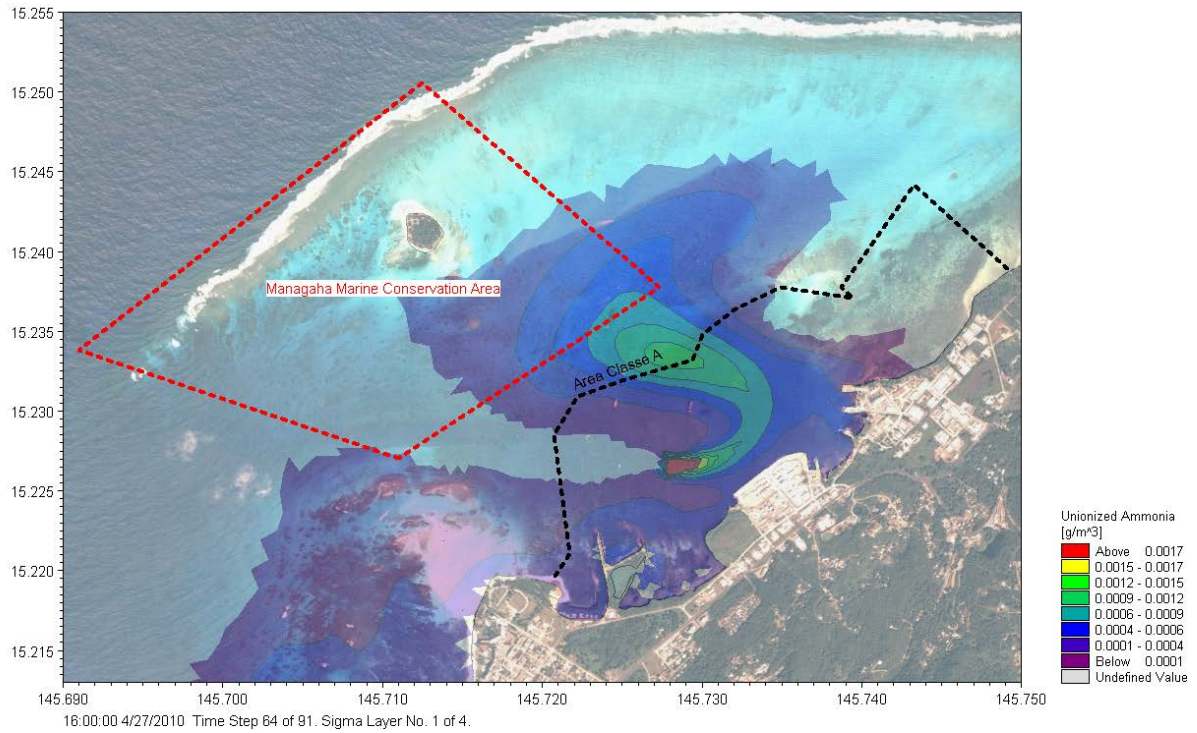


Figure 68. Snapshot of plume of unionised Ammonia under Scenario 1. With a maximum monthly discharge of 0.8g/m^3 of Unionized Ammonia, its concentration in the Class AA is well below 0.02g/m^3 , the limit given by the CNMIWQS for water of Class AA. In water of class A, the limit of 0.05g/m^3 is not exceeded.

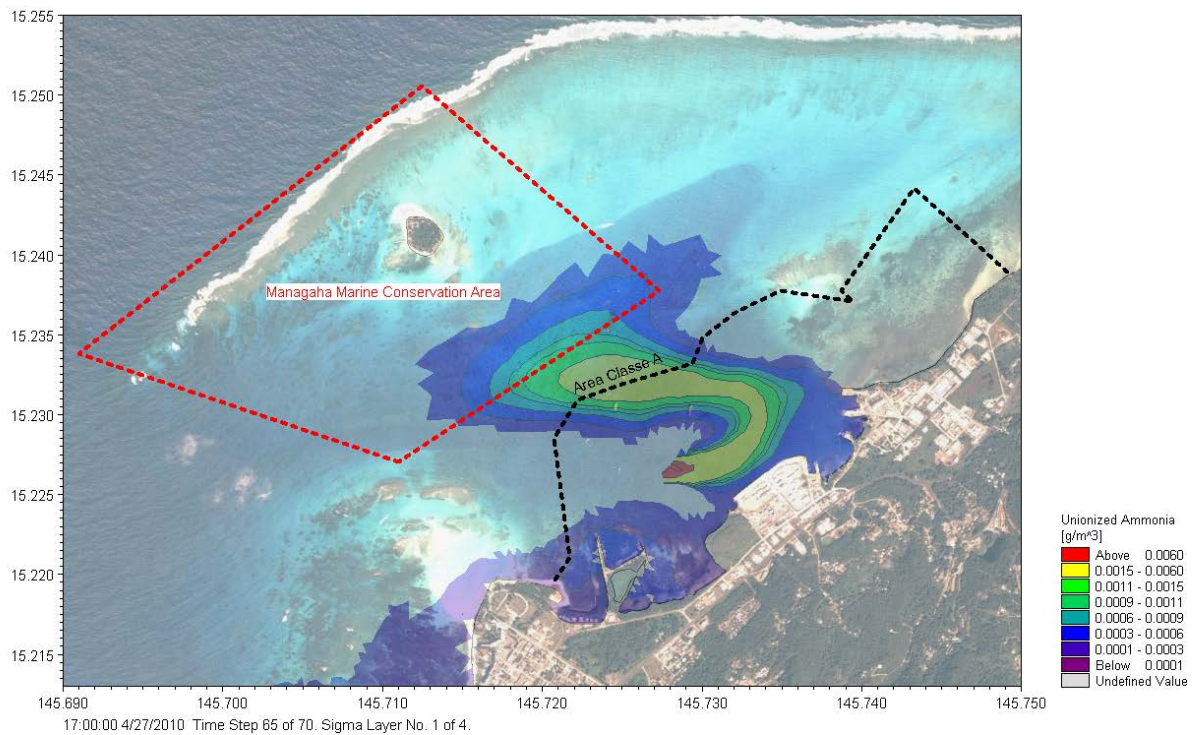


Figure 69. Snapshot of plume of unionised Ammonia under Scenario 1. With a maximum daily discharge of 2g/m^3 of Unionized Ammonia, its concentration in the Class AA is well below 0.02g/m^3 , the limit given by the CNMIWQS for water of Class AA. In water of class A, the limit of 0.05g/m^3 is not exceeded.

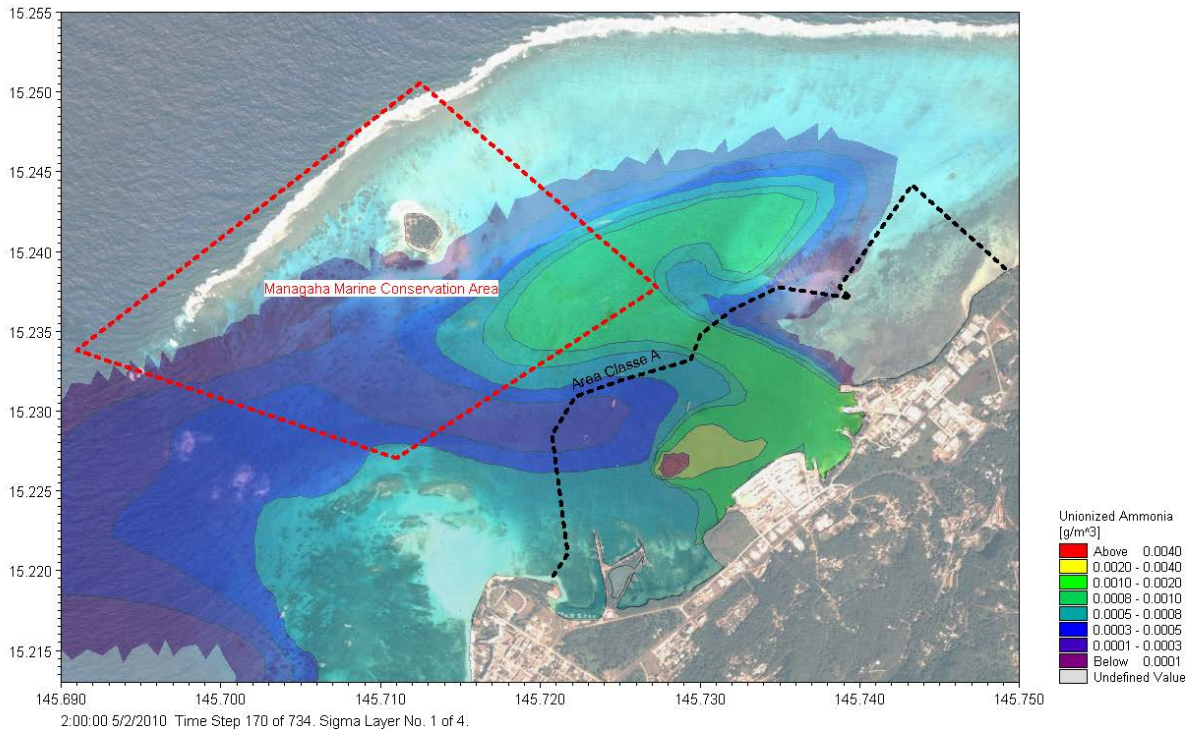


Figure 70. Snapshot of plume of unionised Ammonia under Scenario 2. With a maximum monthly discharge of 0.8g/m^3 of Unionized Ammonia, its concentration in the Class AA is well below 0.02g/m^3 , the limit given by the CNMIWQS for water of Class AA. In water of class A, the limit of 0.05g/m^3 is not exceeded.

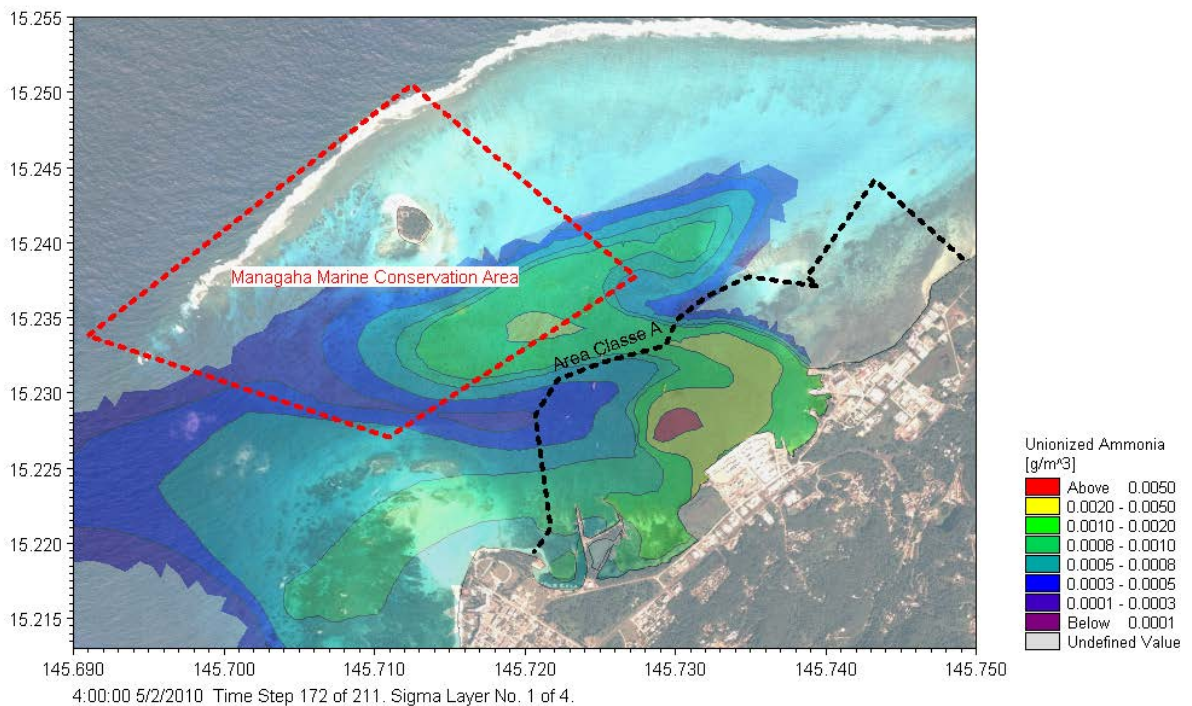


Figure 71. Snapshot of plume of unionised Ammonia under Scenario 2. With a maximum daily discharge of 2g/m^3 of Unionized Ammonia, its concentration in the Class AA is well below 0.02g/m^3 , the limit given by the CNMIWQS for water of Class AA. In water of class A, the limit of 0.05g/m^3 is not exceeded.

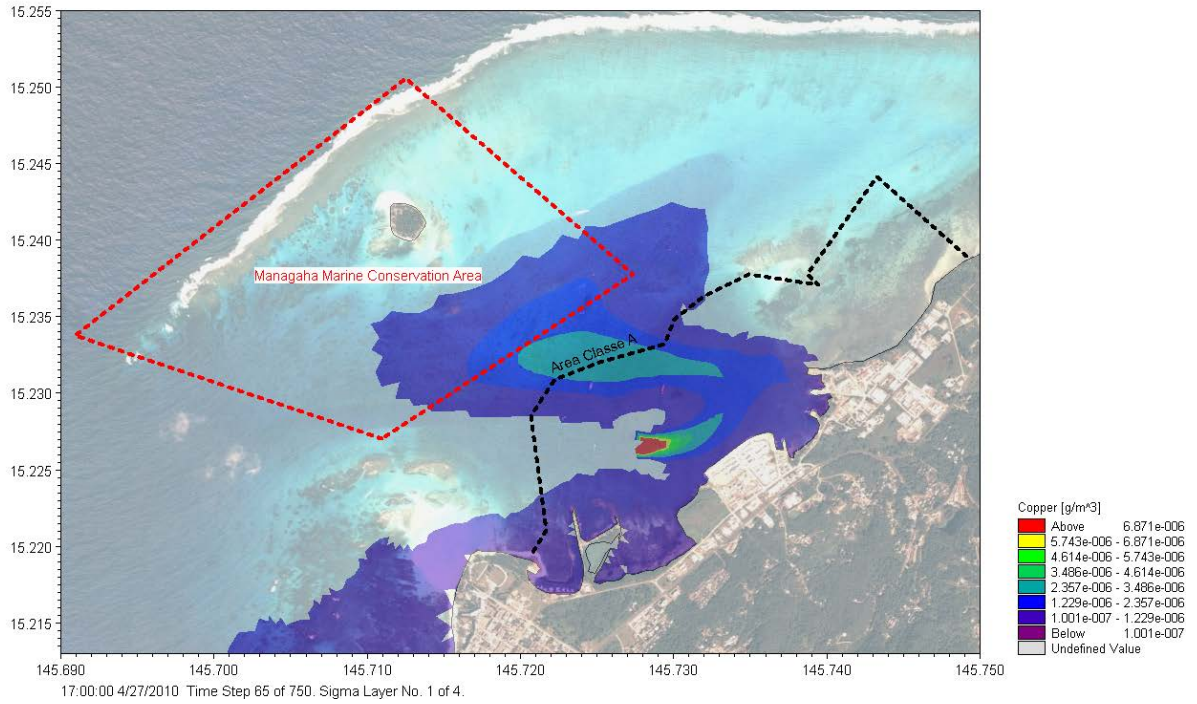


Figure 72. Snapshot of plume of Copper under Scenario 1. With a maximum monthly discharge of $2.4 \mu g/l$ of copper, concentration in the Class AA is well below the saltwater acute criterion of $4.8 mg/m^3$ and the saltwater chronic criterion of $3.1 mg/m^3$ (EPA-822-H-04-001).

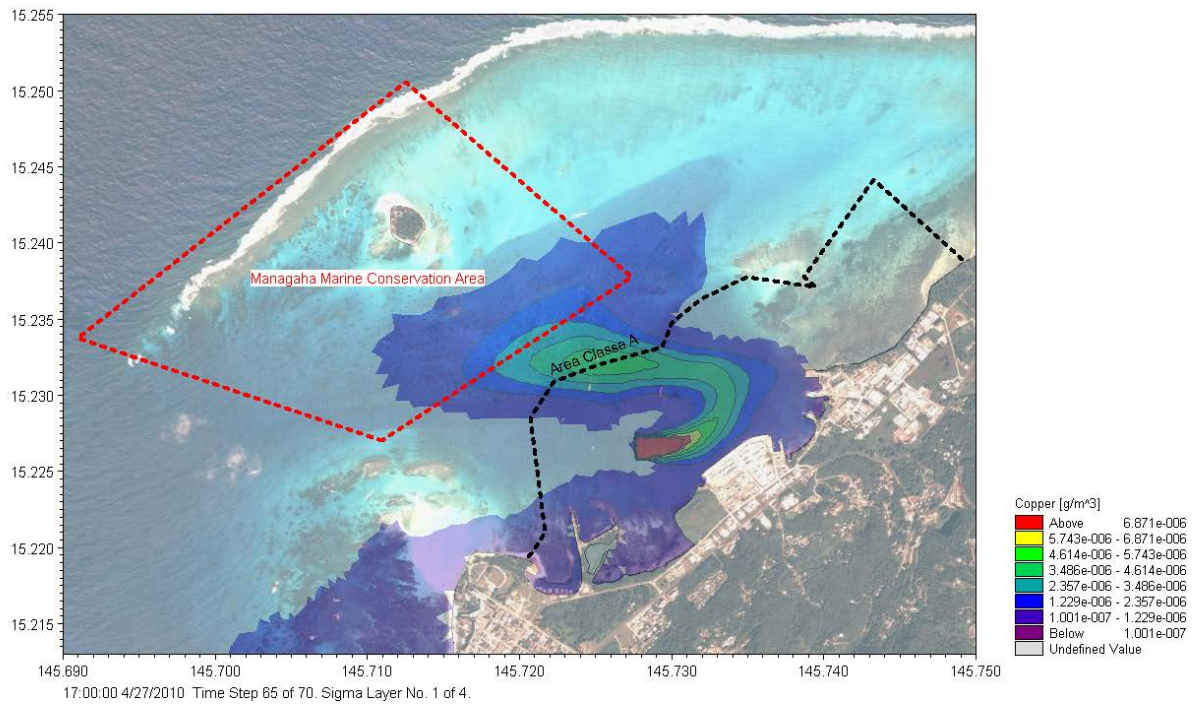


Figure 73. Snapshot of plume of Copper under Scenario 1. With a maximum daily discharge of $4.8 \mu g/l$ of copper, concentration in the Class AA is well below the saltwater acute criterion of $4.8 mg/m^3$ and the saltwater chronic criterion of $3.1 mg/m^3$ (EPA-822-H-04-001).

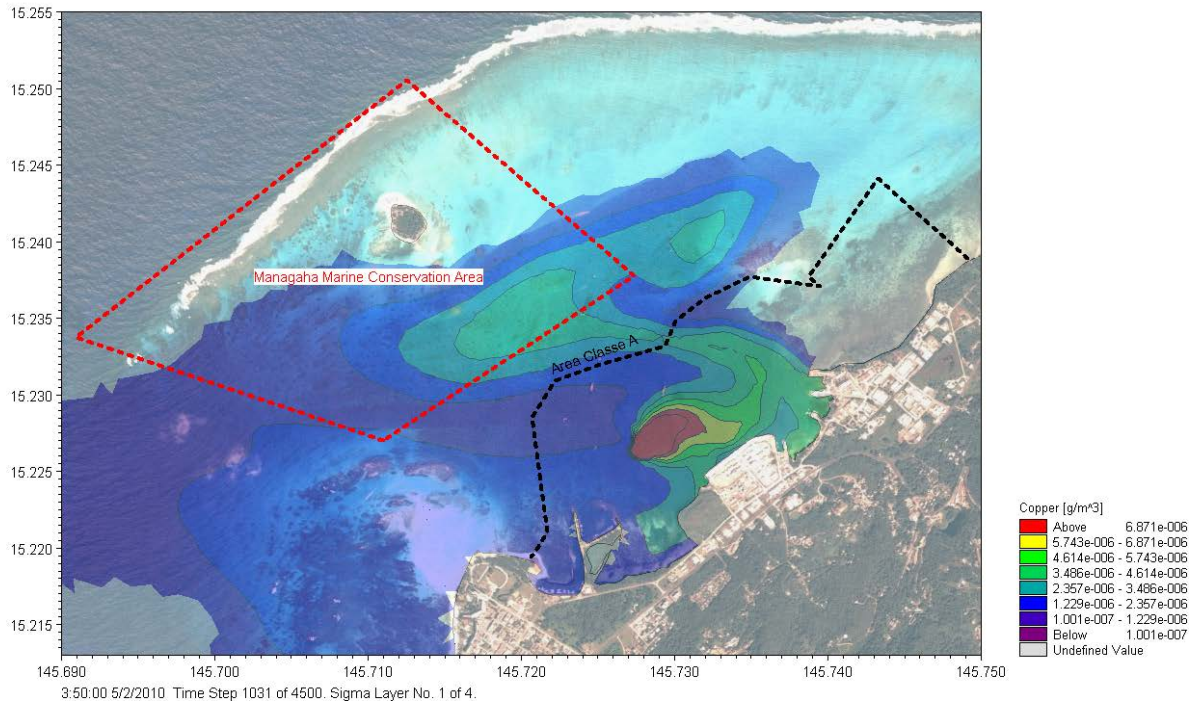


Figure 74. Snapshot of plume of Copper under Scenario 2. With a maximum monthly discharge of 2.4 µg/l of copper, concentration in the Class AA is well below the saltwater acute criterion of 4.8mg/m³ and the saltwater chronic criterion of 3.1mg/m³ (EPA-822-H-04-001).

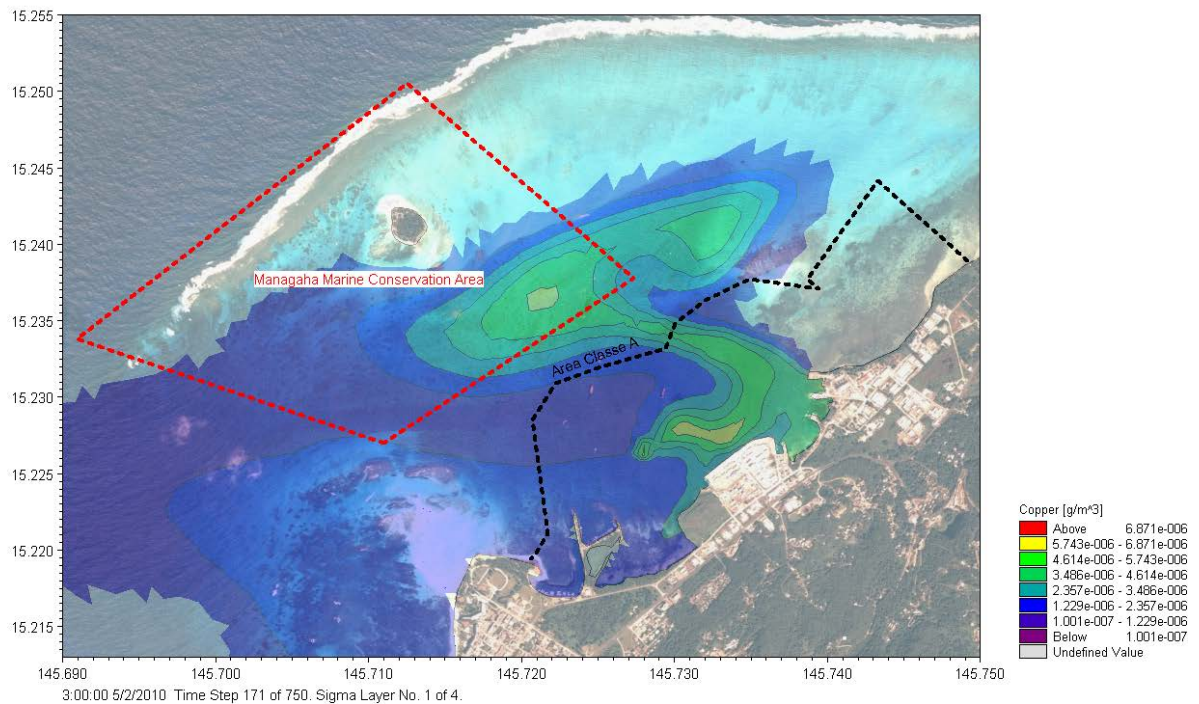


Figure 75. Snapshot of plume of Copper under Scenario 2. With a maximum daily discharge of 4.8 µg/l of copper, concentration in the Class AA is well below the saltwater acute criterion of 4.8mg/m³ and the saltwater chronic criterion of 3.1mg/m³ (EPA-822-H-04-001).

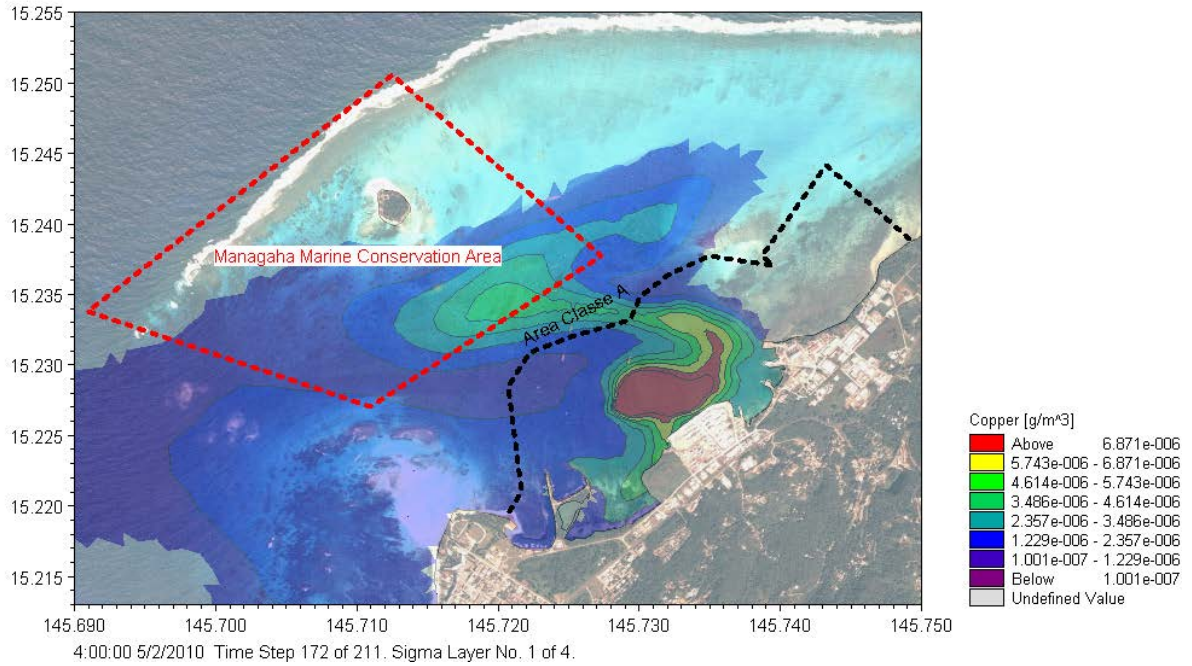


Figure 76. Snapshot of plume of Nickel under Scenario 1. With a maximum monthly discharge of 6.7 µg/l of copper, concentration in the Class AA is well below the saltwater acute criterion of 7.4mg/m³ and the saltwater chronic criterion of 8.2mg/m³ (EPA-822-H-04-001).

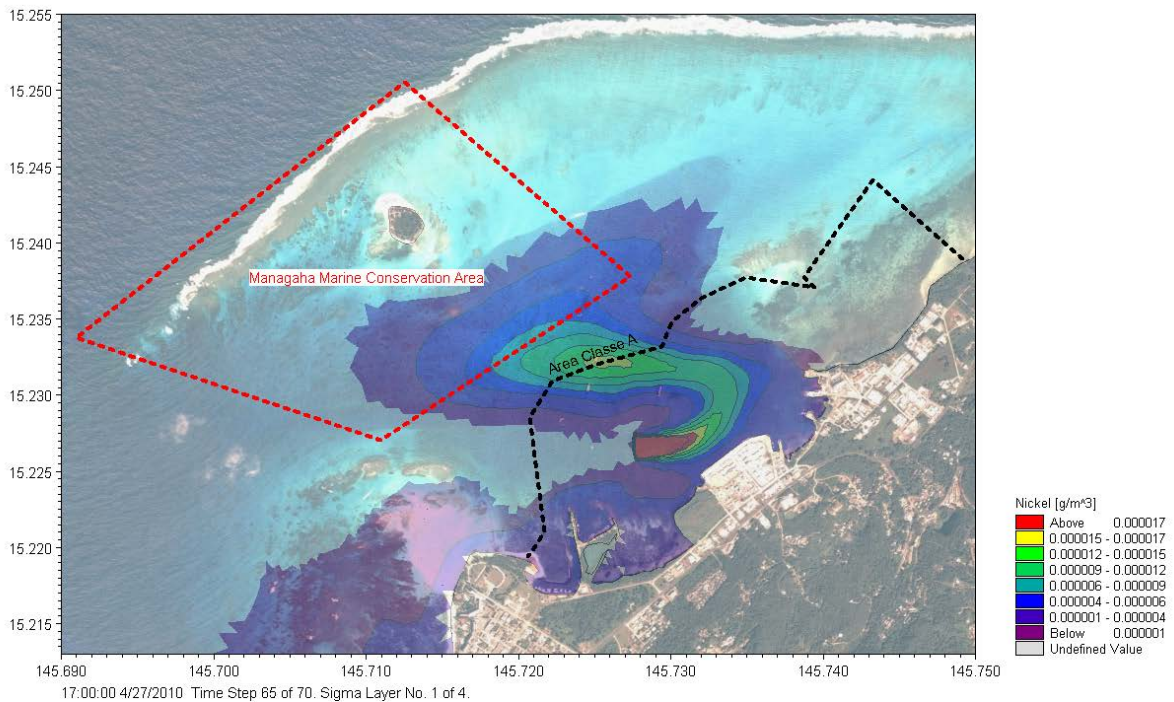


Figure 77. Snapshot of plume of Nickel under Scenario 1. With a maximum daily discharge of 13.4 µg/l of copper, concentration in the Class AA is well below the saltwater acute criterion of 7.4mg/m³ and the saltwater chronic criterion of 8.2mg/m³ (EPA-822-H-04-001).

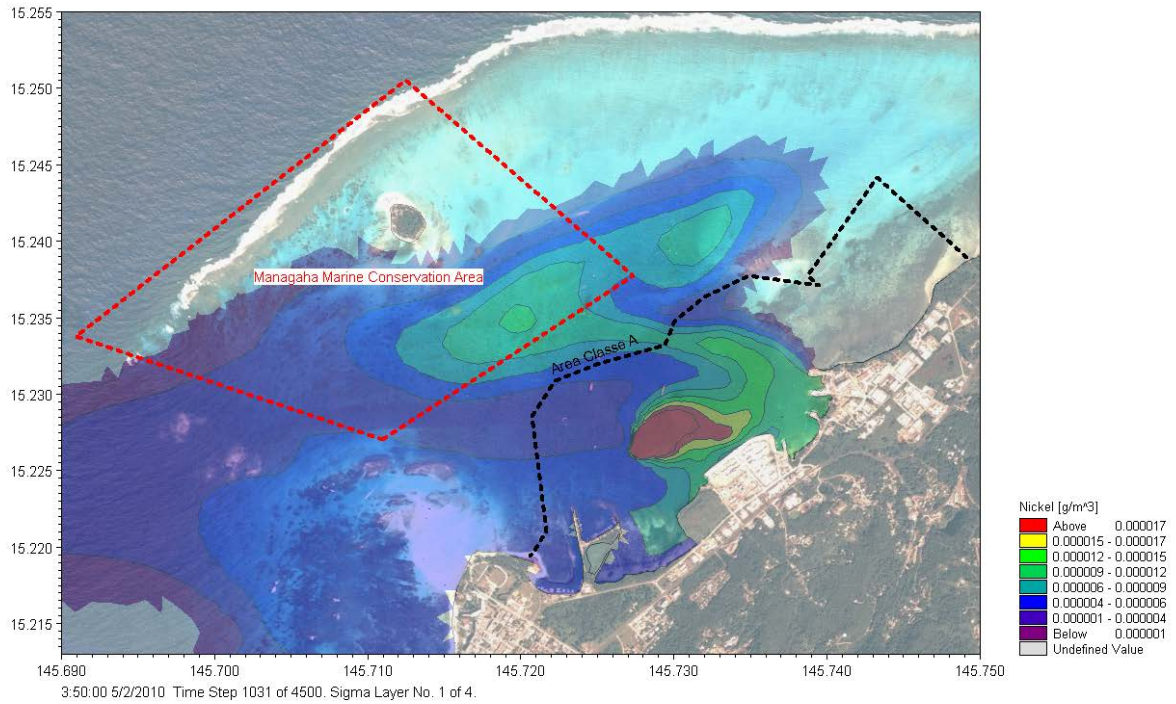


Figure 78. Snapshot of plume of Nickel under Scenario 2. With a maximum monthly discharge of 6.7 µg/l of copper, concentration in the Class AA is well below the saltwater acute criterion of 7.4mg/m³ and the saltwater chronic criterion of 8.2mg/m³ (EPA-822-H-04-001).

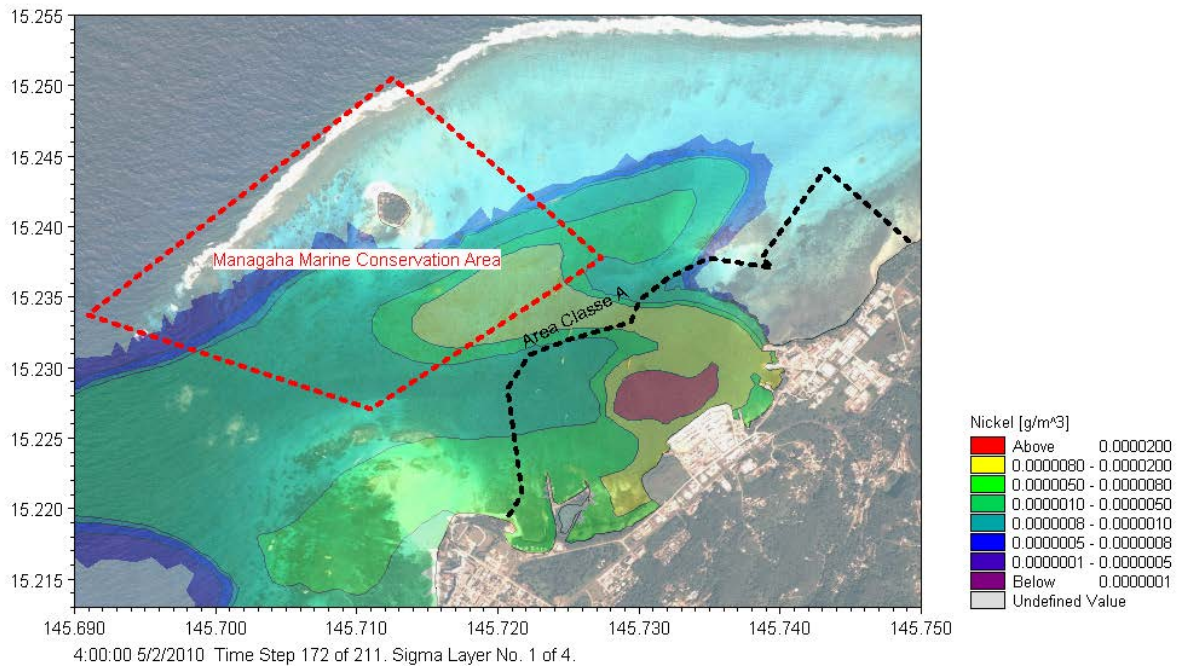


Figure 79. Snapshot of plume of Nickel under Scenario 2. With a maximum daily discharge of 13.4 µg/l of copper, concentration in the Class AA is well below the saltwater acute criterion of 7.4mg/m³ and the saltwater chronic criterion of 8.2mg/m³ (EPA-822-H-04-001).

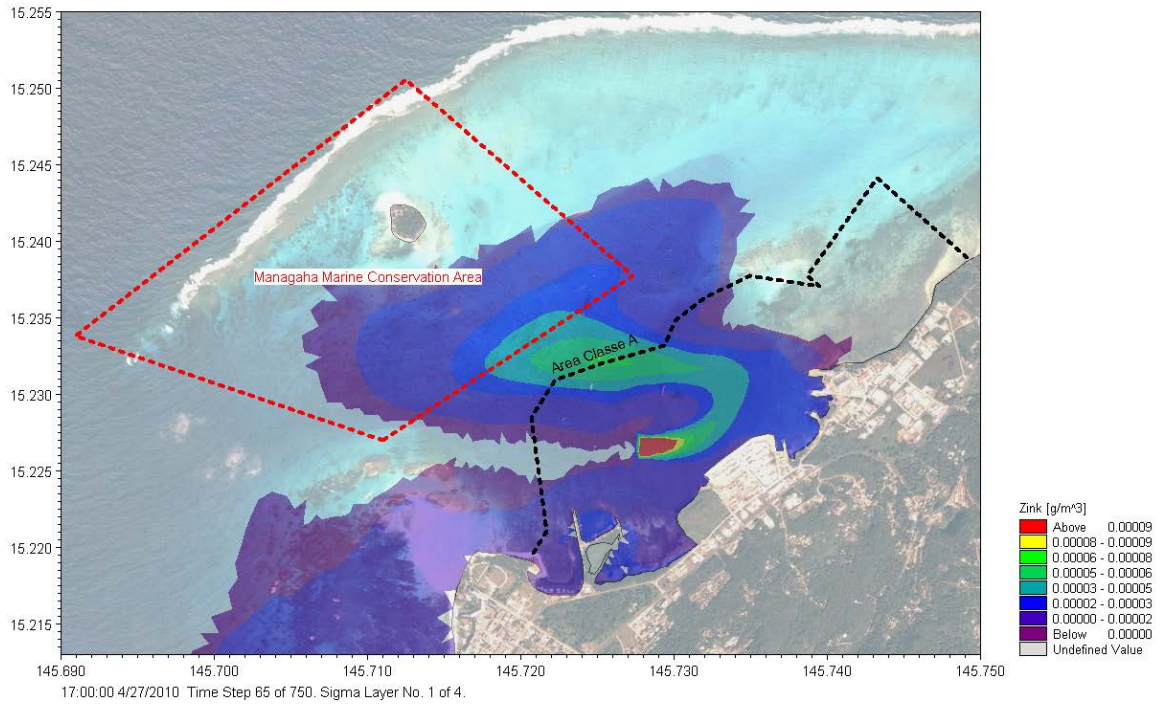


Figure 80. Snapshot of plume of Zink under Scenario 1. With a maximum monthly discharge of 45 µg/l of copper, concentration in the Class AA is well below the saltwater acute criterion of 90mg/m³ and the saltwater chronic criterion of 81mg/m³ (EPA-822-H-04-001).

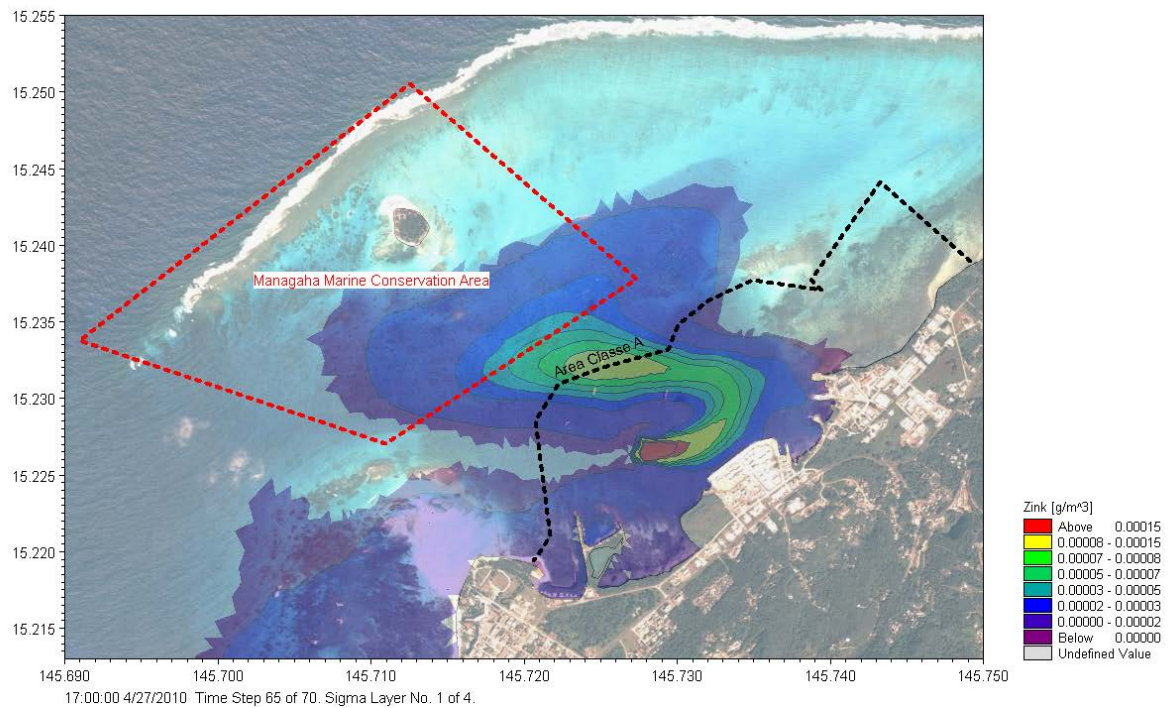


Figure 81. Snapshot of plume of Zink under Scenario 1. With a maximum monthly discharge of 90 µg/l of copper, concentration in the Class AA is well below the saltwater acute criterion of 90mg/m³ and the saltwater chronic criterion of 81mg/m³ (EPA-822-H-04-001).

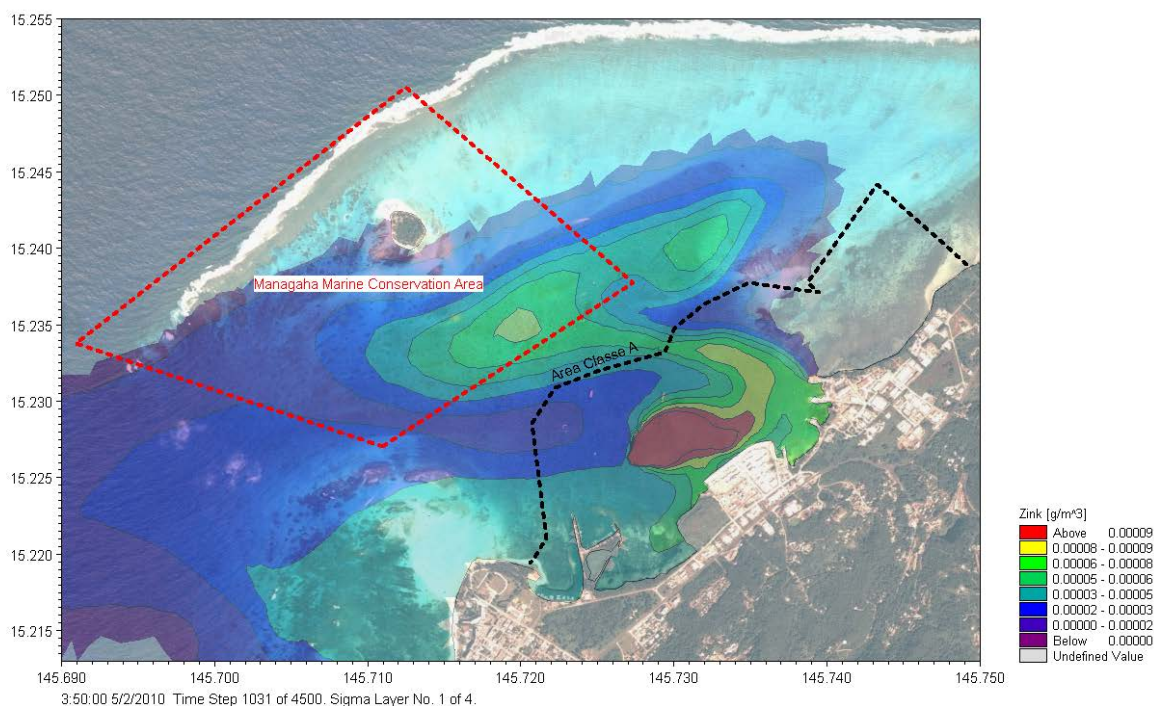


Figure 82. Snapshot of plume of Zink under Scenario 2. With a maximum monthly discharge of 45 µg/l of copper, concentration in the Class AA is well below the saltwater acute criterion of 90mg/m³ and the saltwater chronic criterion of 81mg/m³ (EPA-822-H-04-001).

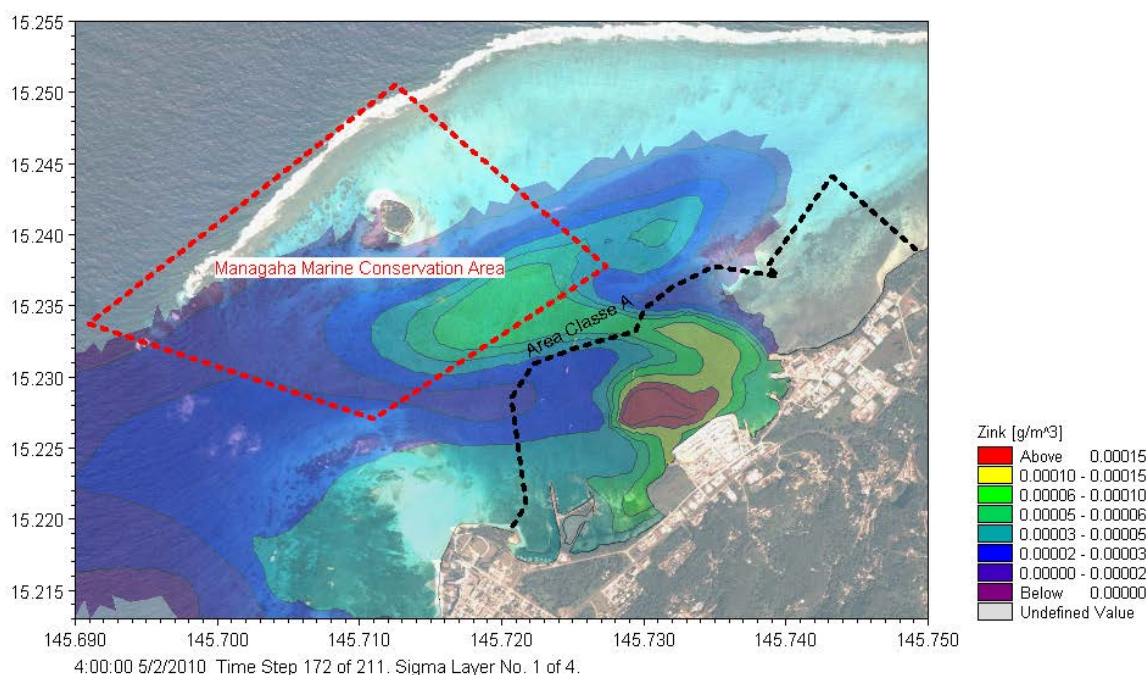


Figure 83. Snapshot of plume of Zink under Scenario 2. With a maximum daily discharge of 90 µg/l of copper, concentration in the Class AA is well below the saltwater acute criterion of 90mg/m³ and the saltwater chronic criterion of 81mg/m³ (EPA-822-H-04-001).

According to the model outputs presented above, the instantaneous concentration of pollutants in the plume discharged from Sadog Tasi outfall is well below the limits stipulated by CNMIWQS. However, the model only investigated the advection and

dispersion of the pollutants, treating them as inert neutrally buoyant particles. No settling velocity other bio-chemical reactions were attributed. The potential for metal to be fixed by sediment is high in Saipan Lagoon (Denton *et al.* 2006). Accumulation of metals in the sediment could be a threat to human health in Saipan. A sediment sample collection survey should be undertaken to further analyse and determine the rate of accumulation of harmful pollutants. The plume pathways presented in this report can act as a guide to concentrate sampling regimes within the common plume pathways such as east and south of Managaha Island as well as near Muchot point.

4.4 Residual Current Patterns

The residual circulation of Saipan Lagoon was investigated using the 3D hydrodynamic numerical model driven by wave, tide, and wind forces. This was done in order to better understand how the external forcing mechanisms interplay with the numerous reefs and inlets to influence the **dominant sediment transport directions along the shoreline of the lagoon system**. The residual circulation was computed by averaging the one-hour time step vectors over a period of one month for each of the two scenarios.

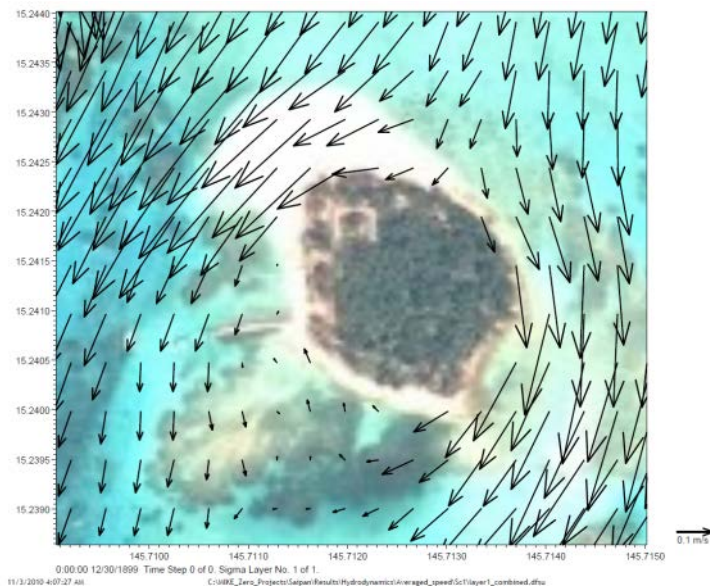


Figure 84. Residual current vectors for Scenario 1 at Managaha Island. Backdrop image is a 2005 Quickbird satellite image (source: CRMO).

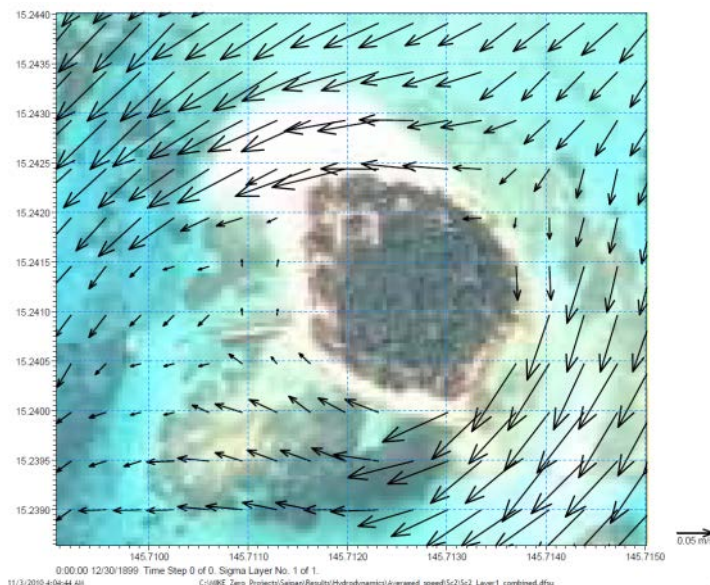


Figure 85. Residual current vectors for Scenario 2 at Managaha Island. Backdrop image is a 2005 Quickbird satellite image (source: CRMO).

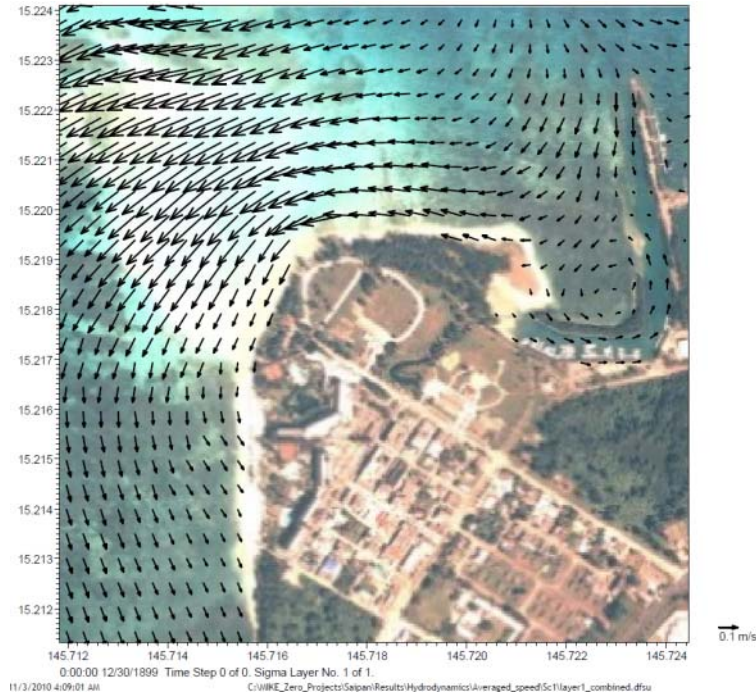


Figure 86. Residual current vectors for Scenario 1 at Muchot Point. Backdrop image is a 2005 Quickbird satellite image (source: CRMO).

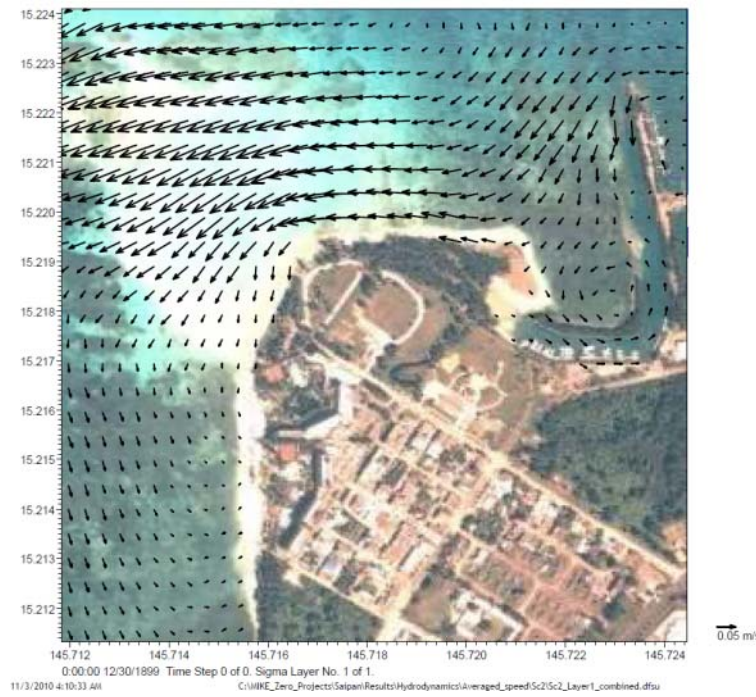


Figure 87. Residual current vectors for Scenario 2 at Muchot Point. Backdrop image is a 2005 Quickbird satellite image (source: CRMO).

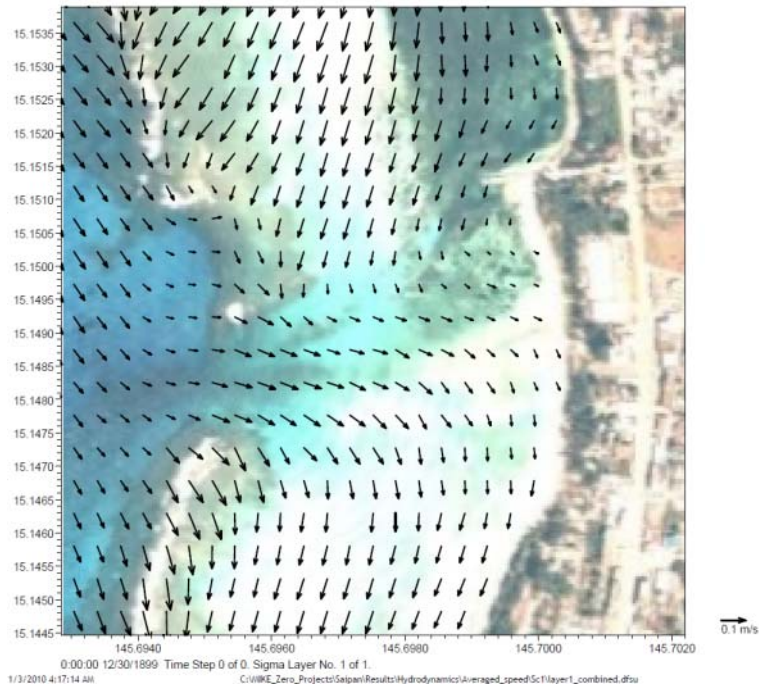


Figure 88. Residual current vectors for Scenario 1 at Sugar Dock. Backdrop image is a 2005 Quickbird satellite image (source: CRMO).

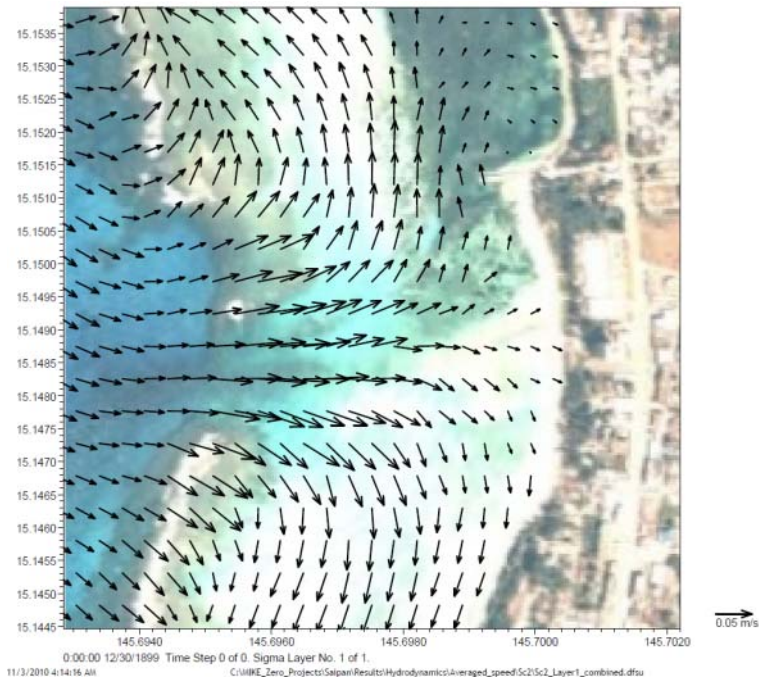


Figure 89. Residual current vectors for Scenario 2 at Sugar Dock. Backdrop image is a 2005 Quickbird satellite image (source: CRMO).

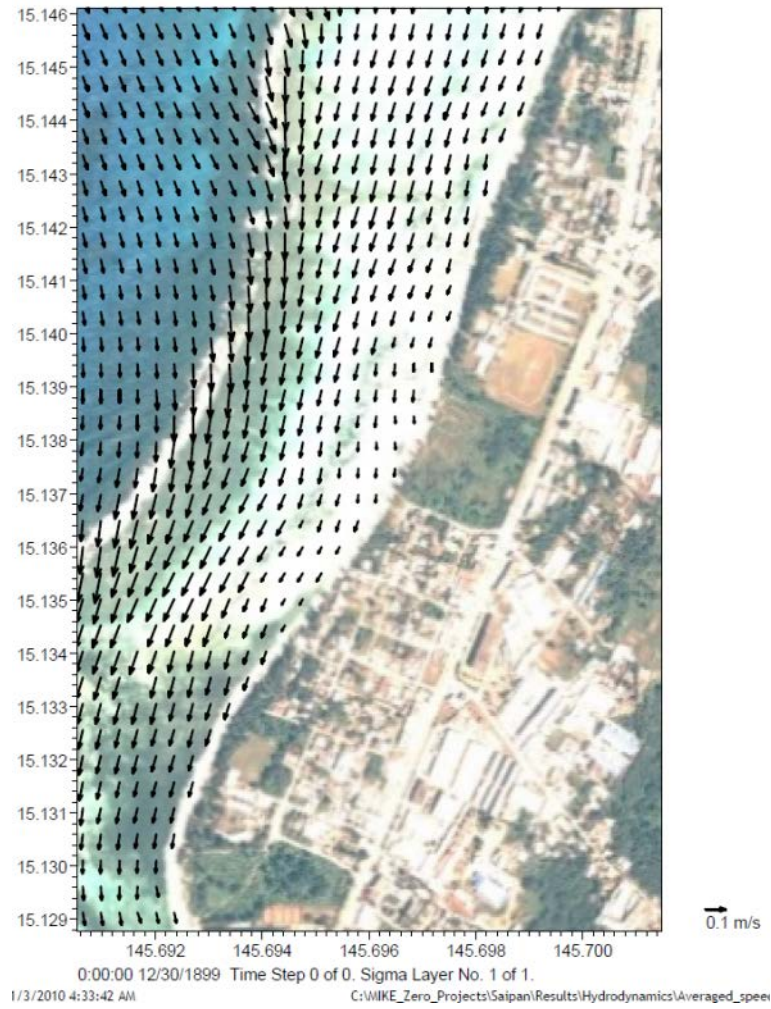


Figure 90. Residual current vectors for Scenario 1 at San Antonio. Backdrop image is a 2005 Quickbird satellite image (source: CRMO).

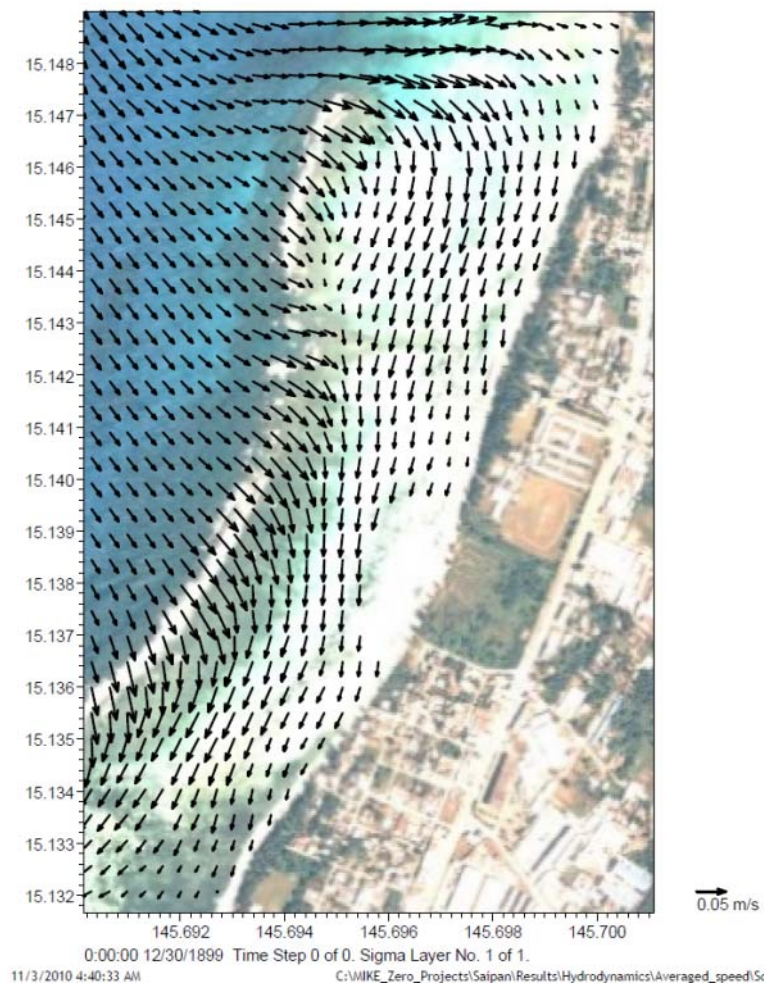


Figure 91. Residual current vectors for Scenario 2 at San Antonio. Backdrop image is a 2005 Quickbird satellite image (source: CRMO).

5 REFERENCES

- Denton, G.R.W., Bearden, B.G., Concepcion, L.P., Wood, H.R., and Morrison, R.J., 2006. Contaminant assessment of surface sediments from Tanapag Lagoon, Saipan, Commonwealth of the Northern Mariana Islands. *Marine Pollution Bulletin* 52, 696-718.
- ECMWF. 2007. IFS Documentation – Cy31r1, Part VII: ECMWF Wave Model. ECMWF, 56 pp.
- Hench, J.L., 2006. Wave-driven circulation on Paopao Bay, Moorea, French Polynesia. Stanford University. Annual Report for Gump South Pacific Research Station, 17 pp.
- Kruger, J., Kumar, S., Damlamian, H., and Sharma, A., 2010. Oceanographic Survey, Shoreline Mapping and Preliminary Hydrodynamic Modelling Report, Saipan, Commonwealth of the Northern Mariana Islands. *SOPAC Data Release Report 26*. 63 pp.
- Lander, M.A., 2004. Rainfall Climatology for Saipan: Distribution, Return-periods, El Nino, Tropical Cyclones, and Long-term Variations. *WERI Technical Report No. 103*. 60 pp.

Lowe, R. J., Falter, J.L., Monismith, S.G., Atkinson, M.J., 2009. Wave-Driven Circulation of a Coastal Reef–Lagoon System. *Journal of Physical Oceanography*, 39, 873–893.

Schoer, G., 2005. Management Plan for the Managaha Marine Conservation Area. Department of Lands and Natural Resources, Division of Fish and Wildlife. Contract No. 426443-OC, 61 pp.

Smithers, S.G. and Woodroffe, C.D. 2000. Microatolls as sea-level indicators on a mid-ocean atoll. *Marine Geology* 168, 61-78.